IMPLEMENTATION OF ORTHOGONAL FREQUENCY DIVISION MULTIPLEXING (OFDM) AND ADVANCED SIGNAL PROCESSING FOR ELASTIC OPTICAL NETWORKING IN ACCORDANCE WITH NETWORKING AND TRANSMISSION CONSTRAINTS

by

Stanley Johnson

_____

A Dissertation Submitted to the Faculty of the

COLLEGE OF OPTICAL SCIENCES

In Partial Fulfillment of the Requirements

For the Degree of

DOCTOR OF PHILOSOPHY

In the Graduate College

THE UNIVERSITY OF ARIZONA

2 0 1 6

THE UNIVERSITY OF ARIZONA
GRADUATE COLLEGE

As members of the Dissertation Committee, we certify that we have read the dissertation prepared by Stanley Johnson, titled Implementation of Orthogonal Frequency Division Multiplexing (OFDM) and Advanced Signal Processing for Elastic Optical Networking in Accordance with Networking and Transmission Constraints and recommend that it be accepted as fulfilling the dissertation requirement for the Degree of Doctor of Philosophy.

_____ Date: April 14th, 2016
Milorad Cvijetic

_____ Date: April 14th, 2016
Ivan Djordjevic

_____ Date: April 14th, 2016
Yuzuru Takashima

Final approval and acceptance of this dissertation is contingent upon the candidate's submission of the final copies of the dissertation to the Graduate College.

I hereby certify that I have read this dissertation prepared under my direction and recommend that it be accepted as fulfilling the dissertation requirement.

_____ Date: April 14th, 2016
Dissertation Director: Milorad Cvijetic

STATEMENT BY AUTHOR

This dissertation has been submitted in partial fulfillment of the requirements for an advanced degree at the University of Arizona and is deposited in the University Library to be made available to borrowers under rules of the Library.

SIGNED: Stanley Johnson

ACKNOWLEDGEMENTS

I have been fortunate to work with several wonderful individuals, both prior to and during my graduate studies. In many ways, this dissertation is a result of their help and support. I wish to thank:

Dr. Milorad Cvijetic, my academic advisor, for his guidance and support. His patience and insights have been very important in enabling my research.

Dr. Ivan Djordjevic and Dr. Yuzuru Takashima for their guidance during the preparation of this dissertation.

Dr. Franko Kueppers, my former advisor, for giving me my very first research opportunity and for his motivation and encouragement.

The National Science Foundation Center for Integrated Access Networks (NSF-CIAN) for funding a major portion of the research in this dissertation.

Dr. Carl Maes for his support, encouragement and for sharing his perspective on the nature of light.

Dr. Stanley Pau for giving me the opportunity to work in his research group.

Dr. John Wissinger, Dr. Jun He and Dr. Daniel Kilper, research collaborators, for a wonderful research experience.

Weiyang Mo, CIAN colleague, for his collaboration on: (a) the experiment described in Chapter 2 of this dissertation, specifically for his work on setting up the software defined networking control plane and (b) the experiment described in Chapter 4 of this dissertation, specifically for his work on setting up the optical network for the experiment and for the measurement of the control latencies.

Mingwei Yang, CIAN colleague, for his collaboration on the experiment described in Chapter 4 of this dissertation, specifically for his work on building the field programmable gate array based distributed control hardware.

Wenbo Gao, Dr. Yequn Zhang, Dr. Houman Rastegarfar, Likun Lin, Dr. Atiyah Ahsan, Aytekin Ozdemir, Dr. Earl Parsons and Dr. Hacene Chaouch, my current and former research colleagues, for enriching my research experience.

Dr. Masud Mansuripur and Dr. Brian Anderson, for their creative and intuitive methods of teaching.

Dr. Vaibhav Bora, Dr. Anoop George and Dr. A. K. Jha, my friends, for their ever-present help and support.

ACKNOWLEDGEMENTS -- *Continued*

Hector Garcia and Ashley Bidegain, for their excellent support that enabled my experimental work.

Shri. M. J. Khurjekar, my teacher during my undergraduate studies, for his advice, motivation and for recommending me for graduate studies.

Abraham T. Joy, Prasad Prabhughate and Krunal Patil, former supervisors and mentors, for their recommendations and their support.

I have also been fortunate to have a wonderfully supportive family, and I wish to thank:

P. V. Abraham, Arun Thomas, Annie Thomas, Sibi Abraham, Binu Mathew and Vincy Mathew, my relatives, for going out of their way to make my stay in an initially unfamiliar country a pleasant experience.

Roy Mammen, my uncle, and Dr. Reny Roy, my aunt, for their motivation, help and support in enabling my graduate studies.

Joy Mathew and Saly Joy, my parents-in-law, and Ashna Joy, my sister-in-law, for their support. *Thank you Pappa! Thank you Mummy! Thank you Unni!*

P. K. Samuel, my grandfather, for his affection and for helping to expand my view of the world through countless discussions on various subjects. *Thank you Appacha!*

M. J. Joseph and Marykutty Joseph, my grandparents, for their affection, support and encouragement. *Thank you Pappa! Thank you Ammachi!*

James Johnson, my brother, for his support over all these years. *Thank you Princy!*

Johnson Samuel, my father, for always being a patient teacher and guide and for his ever-present support. *Thank you Daddy!*

Saji Johnson, my mother, for her guidance, patience and effort towards enabling my studies and for being with me every step of this journey. *Thank you Mummy!*

Diana Joy, my wife, for her patience, understanding and encouragement. *Thank you Di!*

DEDICATION

Dedicated to my parents and grandparents

TABLE OF CONTENTS

TABLE OF CONTENTS – *Continued*

TABLE OF CONTENTS – *Continued*

LIST OF FIGURES

LIST OF FIGURES -- *Continued*

LIST OF FIGURES -- *Continued*

LIST OF FIGURES -- *Continued*

LIST OF TABLES

Abstract

An increasing adoption of digital signal processing (DSP) in optical fiber telecommunication has brought to the fore several interesting DSP enabled modulation formats. One such format is orthogonal frequency division multiplexing (OFDM), which has seen great success in wireless and wired RF applications, and is being actively investigated by several research groups for use in optical fiber telecom.

In this dissertation, I present three implementations of OFDM for elastic optical networking and distributed network control. The first is a field programmable gate array (FPGA) based real-time implementation of a version of OFDM conventionally known as intensity modulation and direct detection (IMDD) OFDM. I experimentally demonstrate the ability of this transmission system to dynamically adjust bandwidth and modulation format to meet networking constraints in an automated manner. To the best of my knowledge, this is the first real-time software defined networking (SDN) based control of an OFDM system.

In the second OFDM implementation, I experimentally demonstrate a novel OFDM transmission scheme that supports both direct detection and coherent detection receivers simultaneously using the same OFDM transmitter. This interchangeable receiver solution enables a trade-off between bit rate and equipment cost in network deployment and upgrades. I show that the proposed transmission scheme can provide a receiver sensitivity improvement of up to 1.73 dB as compared to IMDD OFDM. I also present two novel polarization analyzer based detection schemes, and study their performance using experiment and simulation.

In the third implementation, I present an OFDM pilot-tone based scheme for distributed network control. The first instance of an SDN-based OFDM elastic optical network with pilot-tone assisted distributed control is demonstrated. An improvement in spectral efficiency and a fast reconfiguration time of 30 ms have been achieved in this experiment.

Finally, I experimentally demonstrate optical re-timing of a 10.7 Gb/s data stream utilizing the property of bound soliton pairs (or "soliton molecules") to relax to an equilibrium temporal separation after propagation through a nonlinear dispersion alternating fiber span. Pulses offset up to 16 ps from bit center are successfully re-timed. The optical re-timing scheme studied here is a good example of signal processing in the optical domain and such a technique can overcome the bandwidth bottleneck present in DSP. An enhanced version of this re-timing scheme is analyzed using numerical simulations.

Chapter 1

Introduction

1.1 Telecommunication: A brief history and current trends

Since antiquity, we humans have always sought to better understand the world around us. The information we gather, and its transmission over long distances has shaped our history and culture. History has witnessed several methods of long distance communication – drums, smoke signals, flag semaphores, couriers carrying clay tablets or scrolls on horseback or foot and messenger pigeons to name a few. Many of these methods were set up in chain repeating or relaying fashion so as to increase the total distance over which messages could be transmitted. The study of current electricity in the 18^{th} century paved the way for new methods of communication using wired and wireless telegraphy and telephony in the century that followed. In this period, an example of the use of light as a means of communication is found in the 'Photophone', patented by Bell [1] in 1880. However, interest in optical telecommunication was muted, due to the difficulty in transmitting light over the air over long distances, the unavailability of suitable light waveguides and the ability of wired and wireless radio frequency telecommunication to meet the requirements of capacity at the time.

The growth of voice and data traffic and the advent of the internet in the second half of the last century renewed interest in using light as a carrier of information. The internet and the amount of information coursing through it was projected to grow exponentially and light was the carrier of choice due to its high capacity to carry information as compared to radio frequency carriers. However, light waveguides i.e. optical fibers suffered from very high losses, making even short distance (few tens of meters) optical communication impractical. In 1965, Kao and Hockham proposed that if the optical fiber losses could be reduced from 1000 dB/km at the time

to less than 20 dB/km by reducing impurities in the silica glass used to manufacture optical fiber, practical optical telecommunication was possible [2]. Within just over a decade and with a lot of engineering effort by various research groups, optical fibers with losses in the range of 0.47 dB/km became available. These developments in optical fibers were complemented by advances in semiconductor diode lasers, making optical fiber telecommunication reliable and cost effective. Telephone operators began carrying live voice traffic over city-wide optical fiber links. In the decades that followed, the speed and range of optical fiber telecommunication continued to grow and optic fiber links spanning continents were built.

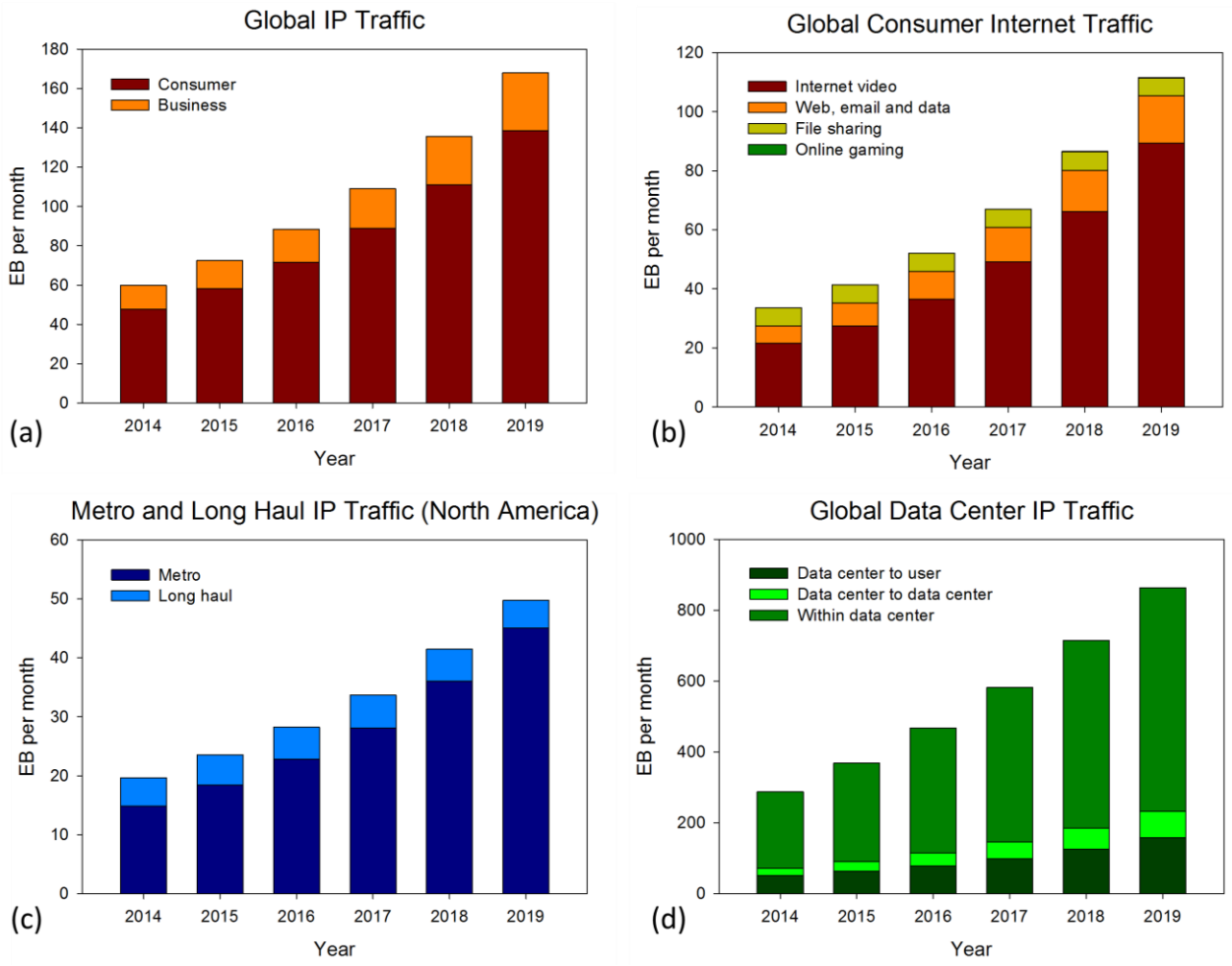

Fig. 1.1 2014 - 2019 trends in data traffic: (a) Global IP traffic (b) Global consumer internet traffic (c) Metro and long haul IP traffic (d) Global data center IP traffic. From [3] and [4]. 1 Exabyte (EB) = 10^9 Gigabytes (GB).

It would be fair to state that the explosive growth of the internet during the last two decades has been enabled by the capacity of optical fiber communication links to meet growing demand

for information. Fig. 1.1 shows data traffic trends for the period 2014 – 2019. Fig. 1.1 (a) shows that the bulk of global internet protocol (IP) traffic will continue to serve consumer needs. Internet video is and will continue to dominate global consumer internet traffic as shown in Fig. 1.1 (b). The bulk of IP traffic will continue to be within metro networks i.e. short haul while the long haul IP traffic is projected to stay fairly constant until 2019 for North America as shown in Fig. 1.1 (c). The rapid adoption of cloud based services will continue to add to the global data center IP traffic, with the bulk of the IP traffic staying within the data center as shown in Fig. 1.1 (d). These projections indicate that there is a continued need for higher bandwidth, short haul telecommunication links serving both metro and intra-data center applications.

1.2 Trends in DSP for optical fiber telecommunication

The last decade has witnessed the development and commercial adoption of digital signal processing (DSP) solutions for optical transport networks [5-8]. The ability to send more data over the same installed fiber capacity by providing for compensation of fiber chromatic dispersion (CD) and polarization mode dispersion (PMD) in addition to the use of higher order modulation formats and forward error correction (FEC) are some of the compelling reasons for DSP in fiber telecom. DSP is also expected to play an important role in next-generation access networks with the need for dynamic bandwidth allocation and adaptive modulation formats [9].

The increasing adoption of DSP has been driven in part by the introduction of application specific integrated circuits (ASICs) for coherent optical transport by several manufacturers, lowering the cost of coherent transceiver/line-card modules and hence the cost per bit for the telecom operators. With inter-operability between such ‘coherent ASICs’ from different manufacturers being established [10], the cost per bit for DSP solutions is further reduced. Another aspect of interest for DSP in optical telecom is the energy consumption per bit. Fig. 1.2 shows that the reduction of power dissipation in complementary metal–oxide–semiconductor (CMOS) technology, which is the dominant technology used to construct integrated circuits (ICs), has not kept up with the reduction of CMOS feature size over time (Moore’s law) and has essentially plateaued. With DSP expected to service future 400 Gbps signals and beyond, optimization of DSP architectures for lower power consumption will be an important engineering challenge.

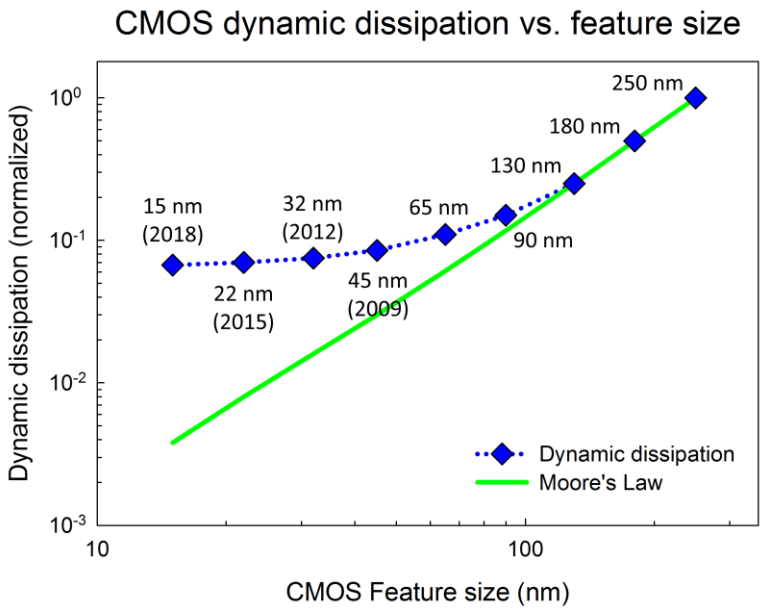

Fig. 1.2 Historical and predicted dynamic power dissipation vs. CMOS feature size. From [11].

DSP-enabled modulation formats such as polarization multiplexed binary phase shift keying (PM-BPSK) and polarization multiplexed quaternary phase shift keying (PM-QPSK) are in use in 100 Gbps coherent optical transport [12, 13] while 4 level pulse amplitude modulation (4-PAM) is in use in data-center and short range optical links [14, 15]. Other DSP-enabled formats such as carrierless amplitude phase (CAP) and orthogonal frequency division multiplexing (OFDM) are being actively investigated for use in optical telecom [16-18].

OFDM is a modulation technique that has been successfully deployed in wireless applications such as the IEEE 802.11 standard for wireless local area networks (also known as WiFi) [19] and wired RF applications such as asymmetric digital subscriber line (ADSL) and very-high-bit-rate digital subscriber line (VDSL) [20]. OFDM has been proposed for optical fiber telecommunication due to its many advantages [21, 22]. The flexibility offered by OFDM and its tolerance to certain transmission impairments, the details of which will be explained in the next section, comes with the requirement for DSP at the transmitter and receiver. Real-time, multi-Gb/s implementations of OFDM for optical telecom, such as those presented in this dissertation and by other groups [23-25], have been demonstrated using field programmable gate arrays (FPGAs) and to the best of my knowledge, there does not exist an ASIC implementation of OFDM for multi-Gb/s optical telecom at present. Similar to the trend seen in the adoption of

coherent optical transport, where 'coherent ASICs' played a key role, it would be reasonable to state that there is a need for multi-Gb/s OFDM ASICs in order to enable adoption of OFDM in optical telecom.

1.3 Introduction to OFDM

OFDM is a multi-carrier modulation technique that uses a large number of low bandwidth carriers (also called subcarriers) as opposed to using a single, large bandwidth carrier used in conventional modulation techniques such as on-off keying (OOK), phase shift keying (PSK) or quadrature amplitude modulation (QAM). The k^{th} OFDM subcarrier (SC) s_k can be represented in the time (t) domain as follows [26]

$$s_k(\mathrm{t}) = \mathrm{rect}(\mathrm{t}/T_S)e^{j2\pi f_k t}\,,\ \mathrm{rect}(\mathrm{t}) = \begin{cases} 1, -1/2 < t \le 1/2 \\ 0, \quad \text{otherwise} \end{cases} \tag{1.1}$$

where T_S is the duration of all OFDM subcarriers in the time domain, this is also called the symbol time; f_k is the frequency of s_k. The orthogonality condition (which distinguishes OFDM from regular frequency/wavelength division multiplexing) is as follows [26]

$$f_k - f_l = n/T_S \tag{1.2}$$

where f_k and f_l are the frequencies of the k^{th} and l^{th} subcarriers respectively and n is an integer. The orthogonality condition enables subcarriers to be closely spaced in the frequency domain, resulting in higher spectral efficiency, while being fully separable at the receiver. This can be understood by considering the correlation between the k^{th} and l^{th} subcarriers s_k and s_l respectively as shown below [26]

$$\langle s_l, s_k \rangle = \frac{1}{T_s}\int_{\frac{-T_S}{2}}^{\frac{T_S}{2}} s_k(t)s_l^*(t)dt = \frac{\sin(\pi(f_k - f_l)T_S)}{\pi(f_k - f_l)T_S} = sinc\big((f_k - f_l)T_S\big)\Big|_{f_k - f_l = n/T_S} = 0 \tag{1.3}$$

where the * indicates complex conjugation. Here we can see that the orthogonality condition in Eqn. 1.2 results in zero correlation between the k^{th} and l^{th} subcarriers, hence each subcarrier can be recovered at the receiver with no crosstalk between subcarriers. The orthogonality condition

requires the frequency of the k^{th} subcarrier to be k/T_S. Thus the time domain expression for the OFDM signal with N_{SC} number of subcarriers is given by

$$s(t) = \begin{cases} \sum_{k=-N_{SC}/2}^{k=N_{SC}/2-1} X_k e^{j2\pi \frac{k}{T_S} t}, & -T_S/2 < t \leq T_S/2 \\ 0, & otherwise \end{cases} \tag{1.4}$$

where X_k denotes the complex symbol used to modulate the k^{th} subcarrier.

Fig. 1.3 depicts the time domain representation of 4 OFDM subcarriers. For simplicity, only positive subcarrier frequencies are considered and the waveforms are for the real component of the subcarriers. In Fig. 1.3, each SC is modulated by a real symbol of unit amplitude as shown in the complex plane representation. The real component of the resulting OFDM waveform is also shown. The frequency spectrum plot on the right in Fig. 1.3, shows each of the SCs in the

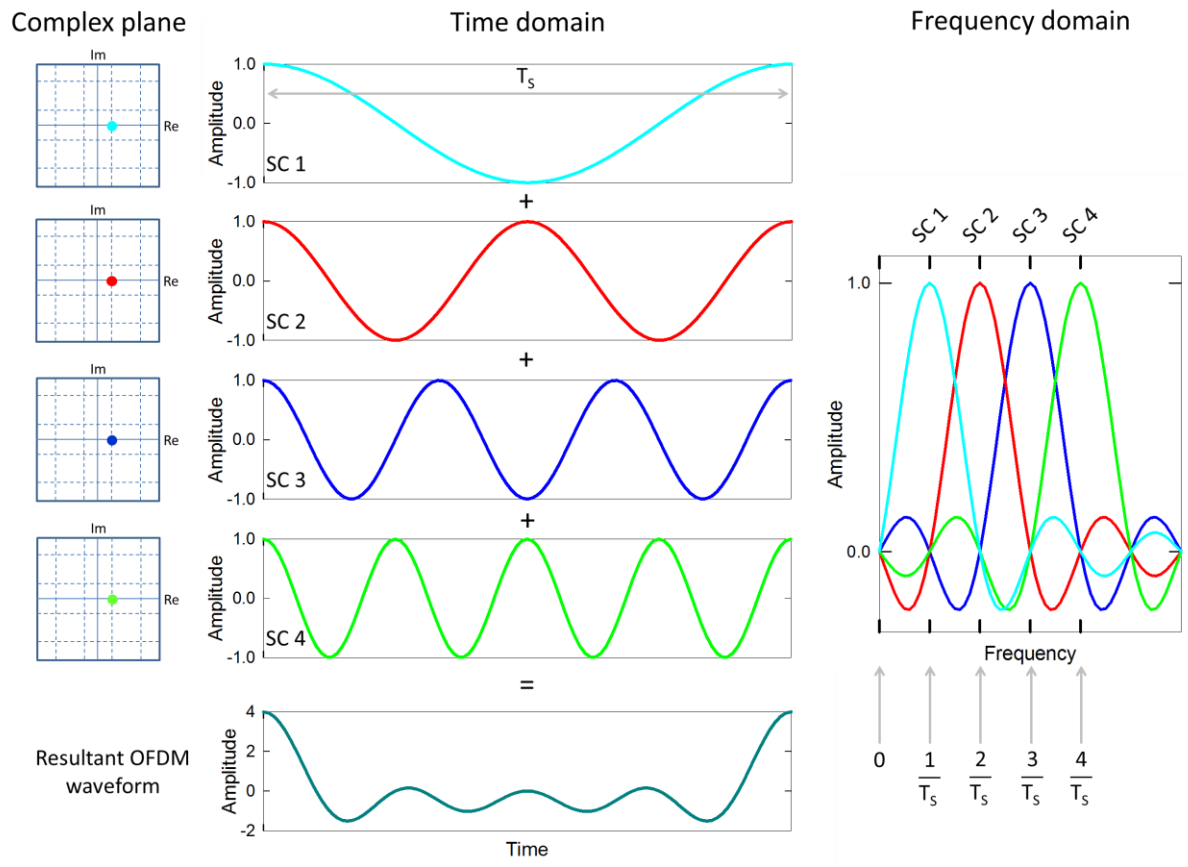

Fig. 1.3 The complex plane, time domain and frequency domain representations of a 4 subcarrier (SC) OFDM signal. All SCs are modulated with a unit amplitude real symbol.

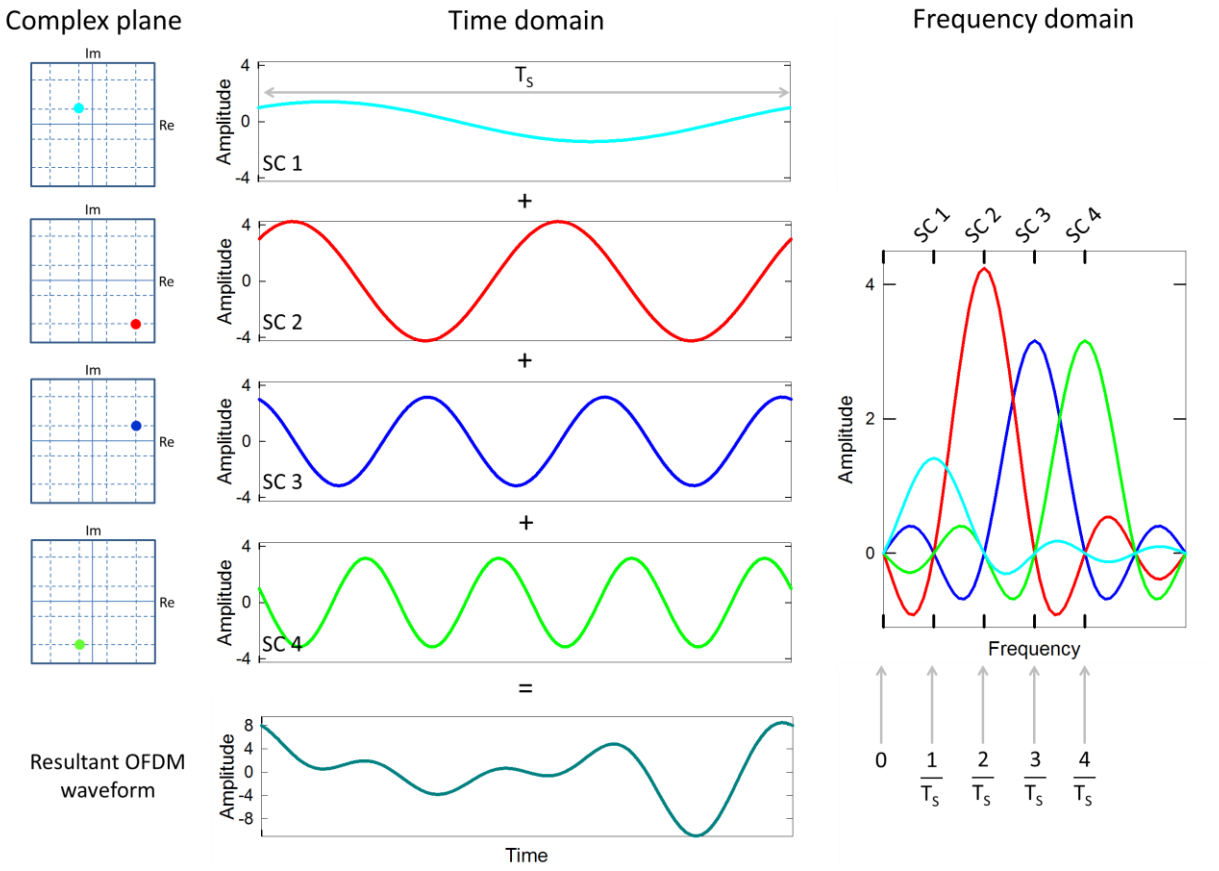

Fig. 1.4 The complex plane, time domain and frequency domain representations of a 4 subcarrier (SC) OFDM signal. Here, each SC is modulated with a complex 16-QAM symbol.

resultant OFDM spectrum. The frequency domain amplitude is normalized relative to a complex modulating symbol of unit amplitude.

Fig. 1.4 depicts the time domain representation of 4 OFDM subcarriers, with each SC being modulated by a complex 16-QAM symbol as shown in the complex plane representation. Again, for simplicity, only positive subcarrier frequencies are considered and the waveforms are for the real component of the subcarriers. The effect of modulation on the amplitude and phase of each of the 4 SCs can be seen in the time domain representation. The real component of the resulting OFDM waveform is also shown. The frequency spectrum plot on the right in Fig. 1.4, shows each of the SCs in the resultant OFDM spectrum, the variation in SC spectral amplitude based on the complex symbol modulating the SC is visible. The frequency domain amplitude is normalized relative to a complex modulating symbol of unit amplitude. It is important to note

that the orthogonality condition is not violated when the amplitude and phase of the SCs are modulated as such modulation does not change the frequency of the SCs.

OFDM modulation and demodulation can be performed by using the inverse discrete Fourier transform (IDFT) and discrete Fourier transform (DFT) respectively [27]. Since the inverse fast Fourier transform (IFFT) and fast Fourier transform (FFT) are efficient implementations of the IDFT and DFT respectively, the IFFT and FFT are the implementations of choice for generating and receiving OFDM signals.

OFDM systems can be classified according to the method of SC generation into the following two types:

1. Optically generated OFDM SCs: Here the OFDM SCs are generated optically and individually modulated with data. The orthogonality condition is maintained by using a source with frequency locked SCs, usually from an optical frequency comb generator.
2. Electrically generated OFDM SCs: Here the SCs are generated electrically, usually using the IFFT operation on electronic hardware, followed by digital to analog converters (DACs). The resulting complex electrical signal is used to modulate an optical carrier, causing the OFDM signal to now be up-converted to the optical carrier frequency. In this dissertation, I have used the electrically generated OFDM SCs – in Chapters 2 and 3, an FPGA followed by DACs are used to generate the electrical OFDM signal; in Chapter 4, an arbitrary waveform generator (AWG) is used as the electrical OFDM signal source.

Another method of classification of OFDM systems is by considering the type of receiver used for OFDM detection:

1. Coherent detection: This method is simply the regular OFDM discussed earlier in the introduction. Both amplitude and phase of the optical carrier are modulated by the complex OFDM signal and hence a coherent receiver is necessary. In Chapter 3, I present an experiment that includes coherent OFDM detection.
2. Direct detection: This method is also called intensity modulation and direct detection (IMDD) or discrete multi-tone (DMT) modulation and is a subset of regular OFDM. IMDD OFDM has half the information capacity compared to an equivalent coherent/regular OFDM signal. This is due to the fact that in IMDD OFDM, out of N_{SC}

subcarriers, only $N_{SC}/2$ subcarriers are modulated with data symbols, the other $N_{SC}/2$ subcarriers are modulated with the complex conjugate of the data symbols in order to meet the Hermitian symmetry requirement

$$X_{N_{SC}/2-k} = X^*_{-N_{SC}/2+k}, k = 1, 2, \ldots . N_{SC}/2 - 1; Im\{X_{-N_{SC}/2}\} = Im\{X_0\} = 0 \quad (1.5)$$

Eqn. 1.5 also specifies the additional requirement that the data symbols modulating the $-N_{SC/2}{}^{th}$ and 0^{th} SCs must be real valued. With these requirements met, the time domain expression for the OFDM signal with N_{SC} number of subcarriers as specified in Eqn. 1.4 becomes real valued [26] and hence can be used to modulate the intensity of an optical carrier either using a directly modulated laser (DML) or an intensity modulator after a carrier source. At the receiver, direct detection using a photodiode is employed. This simplicity of the transmitter and receiver lowers the cost for an IMDD OFDM system. In Chapters 2, 3 and 4, I present experiments that employ IMDD OFDM.

OFDM has several advantages when used in optical telecom as noted below

1. The division of the available bandwidth into lower baud rate subcarriers increases the tolerance of the OFDM signal to fiber chromatic dispersion. The use of the cyclic prefix [26] can help to further reduce the effects of chromatic dispersion (primarily inter-symbol interference).
2. OFDM is well suited to elastic optical networking. Every OFDM SC can be modulated with a modulation format that is best suited to maximize that SC's data transmission capacity under given transmission constraints. Individual SCs can also be left unmodulated, this technique offers high bandwidth granularity and the OFDM signal can be continuously adapted to meet current data traffic requirements while conserving bandwidth and energy. Multiple users can be supported simultaneously by allocating one or more SCs to each user.
3. The use of the FFT operation at the OFDM receiver has the benefit that channel impairments such as chromatic dispersion and frequency selective fading can be compensated using a single complex multiplication per SC i.e. one-tap equalization.

OFDM has the following disadvantages

1. The OFDM waveform has a high peak to average power ratio (PAPR) compared to conventional modulation formats. This makes OFDM more susceptible to nonlinear impairments when launched at high optical power into fiber.
2. The process of generation and demodulation of OFDM signals is more complex compared to conventional modulation formats.
3. Synchronization of the OFDM waveform at the receiver is critical for proper OFDM reception.

The benefits offered by OFDM far outweigh their disadvantages. The falling cost per bit for DSP will enable inexpensive OFDM processors to be built making OFDM an attractive option for next generation optical networks.

1.4 Overview of the dissertation

In this chapter, I have provided an introduction to the trends in optical fiber telecommunication and also introduced OFDM. In Chapter 2, I present a real-time IMDD OFDM system that I developed. I also discuss results from an experimental demonstration of this IMDD OFDM system performed in collaboration with my colleagues. I also compare the power consumption and energy efficiency of this IMDD OFDM system with commercially available networking hardware.

In Chapter 3, I present a coherent OFDM system that has the capability to communicate simultaneously with direct detection and coherent detection receivers. As this is a self-coherent system with the carrier transmitted in a polarization orthogonal to the polarization of the signal (pol mux transmission), I discuss the method of polarization tracking I use in this experiment. I compare the pol mux scheme to the conventional IMDD OFDM scheme and show that the pol mux scheme is more resilient to nonlinear impairment in fiber. Finally I present an enhanced detection scheme for the pol mux transmission and show that it has superior performance compared to a detection scheme presented earlier in this chapter.

In Chapter 4, I present a distributed control scheme using a low frequency OFDM subcarrier (pilot-tone) to convey control commands to optical network elements. I discuss results from an experiment conducted in collaboration with my colleagues that demonstrates the feasibility of using an OFDM pilot-tone for distributed control of network elements.

In Chapter 5, I present a nonlinear optical scheme that utilizes the 'soliton molecule' effect to re-time an optical data stream. I present results from the experimental verification of this scheme and also discuss simulation results for an enhanced re-timing scheme. I also compare the power consumption and energy efficiency of this scheme with commercially available optical signal regeneration hardware.

The Appendix section details the OFDM frame synchronization method that I developed in the course of my design and development of the FPGA based IMDD and coherent OFDM systems. Here, I present all important flowcharts, circuit schematics and the timing diagrams for relevant signals.

Chapter 2

Real-time elastic transmission with direct detection OFDM

2.1 Introduction

Orthogonal frequency division multiplexing (OFDM)-based schemes allow optical network implementations featuring high spectral efficiency, flexibility, and impairment resilience. Bandwidth granularity offered by OFDM is quite important for next generation elastic optical networks [28], with applications ranging from high-speed core network connections, to optical access and mobile backhaul scenarios [29, 30]. In particular, in [30], software-defined OpenFlow-based control was introduced to enable dynamic optical circuit creation for OFDM-based mobile backhaul overlays over legacy optical access networks. However, the OFDM-based processing was static and performed off-line. In this chapter, I will present my work on an implementation of software-defined optical OFDM-based access networks by demonstrating *real-time* dynamic adjustment of OFDM signal bandwidth and modulation format. I experimentally verify dynamic OFDM resource allocation scheme for passive optical networks (PON), wherein the software defined networking (SDN) approach is exploited to support real-time dynamic control of OFDM signal parameters, including subcarrier (SC) assignment and modulation format selection. I experimentally confirm that service impairment due to optical signal to noise ratio (OSNR) variation can be detected and remedied by the SDN controller within seconds for 20 km standard single mode fiber (SSMF) transmission. The augmented SDN takes advantages of converged networks to support intelligent functionalities by adding situation-awareness, such as knowledge of protocols, link congestion, and/or quality of transmission (QoT) [31]. In addition, the SDN can take care of QoT to operate OFDM dynamically based-on certain quality requirements (i.e. BER).

2.2 FPGA architecture for direct detection OFDM

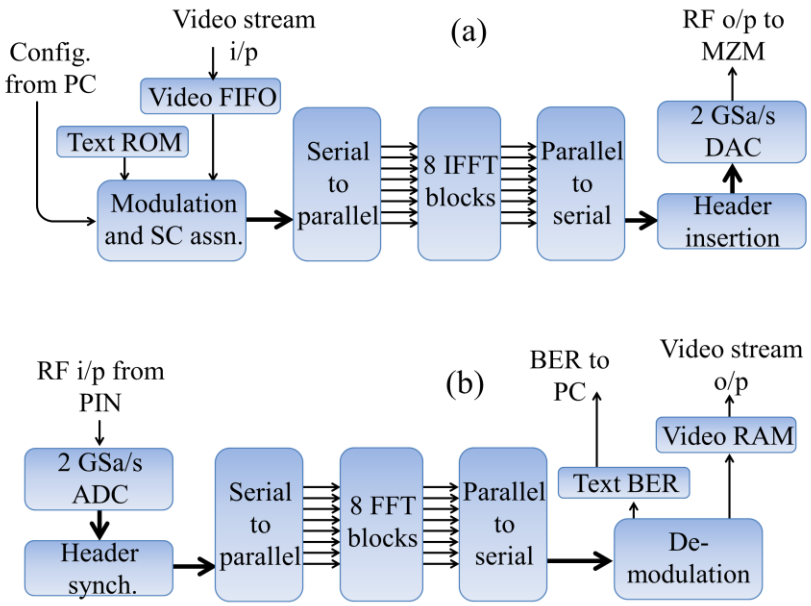

Fig. 2.1 FPGA architecture – (a) The OFDM transmitter (Tx) (b) The OFDM receiver (Rx)

The heart of the real-time system is the field programmable gate array (FPGA) OFDM implementation. The real-time OFDM transmitter (Tx) and receiver (Rx) as shown in Fig. 2.1 were implemented on a BEEcube BEE3 field programmable gate array (FPGA) system. The BEE3 system has four Xilinx Virtex-5 XC5VSX95T FPGAs, each connected to either a DAC or an ADC. The system has two DACs and two ADCs, each with a maximum sampling rate of 2 GSa/s. In this experiment, I used one FPGA-DAC pair as the Tx and one FPGA-ADC pair as the Rx. The Virtex-5 datasheet [32] specifies a maximum clock frequency of 500 MHz for the DSP48E logic block (this is the hardware element on which the IFFT/FFT computations are performed) for a speed grade of -2. I set timing constraints in the Xilinx ISE 13.4 tool to determine the maximum clock frequency I could use for a 1024 point IFFT computation with no setup and hold violations. I obtained a maximum clock frequency of 270 MHz. Since 2 GSa/s / 270 MHz = 7.4 samples per clock cycle, I decided to use 8 parallel IFFT/FFT blocks, each clocked at 250 MHz, in order to match the DAC/ADC throughput of 2 GSa/s while still meeting all timing constraints.

It is important to note that although 8 IFFT/FFT blocks operate in parallel, they do so on different time slots of the transmitted/received data i.e. data from each IFFT (to each FFT) computation and across the 8 IFFT (FFT) computations maintain their chronological order. This is achieved using the serial to parallel and parallel to serial blocks shown in Fig. 2.1. The IFFT/FFT computations are performed by 8 instantiations of the Xilinx Fast Fourier Transform v7.1 LogiCORE IP [33] in pipelined, streaming I/O mode with fixed point arithmetic.

At the Tx, the 1024-point IFFT with Hermitian symmetric inputs generates a 512 subcarrier (SC) real valued electrical OFDM signal suitable for intensity modulation. Each subcarrier has a bandwidth of 1 GHz / 512 = 1.95 MHz. Two data streams – text and video are used as data inputs to the OFDM Tx. The text data is a predefined ASCII encoded version of text from literature that is stored on a read-only memory (ROM) block on the Tx FPGA. Video data is obtained over an Ethernet line from a personal computer (PC) running VLC media player [34] as a streaming video source to the Tx FPGA. The 1370 byte user-defined protocol (UDP) video data packets entering the Tx FPGA are handled by a Virtex-5 embedded Tri-Mode Ethernet MAC (TEMAC) hardware block [35]. The video packets are then sent to a 16 KB first-in first-out (FIFO) memory block. The FIFO block acts as a 'leaky bucket' and ensures that no video frames are lost due to the burst nature of video traffic where the instantaneous bit rate of the video input (up to 1 Gb/s) to the Tx FPGA can exceed the bit rate assigned to the video data on the OFDM transmission (133.66 Mb/s).

After demodulation at the Rx FPGA, the video data are sent to a 4 KB RAM memory block. A Virtex-5 TEMAC hardware block [35] reads video data from the RAM and puts out UDP packets on an Ethernet line. Because the TEMAC has a read speed of 1 Gb/s from the video RAM, the RAM can be emptied of video data faster than the rate at which the RAM fills up i.e. 133.66 Mb/s. Hence only a 4 KB RAM block is sufficient at the Rx FPGA. The streaming video is received by a PC running VLC media player [34] connected to the Ethernet line.

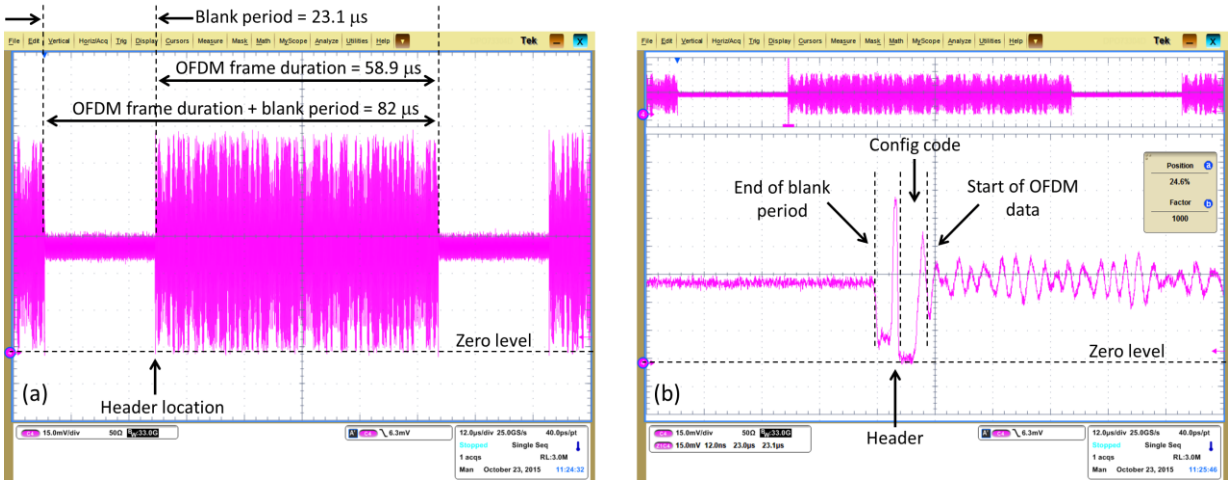

Fig. 2.2 (a) The OFDM frame time domain structure (b) The temporal structure of the frame header that is used for OFDM synchronization at the Rx.

Fig. 2.2 (a) shows the OFDM data which is transmitted in frames of 58.9 µs duration, each containing 115 IFFT frames. One IFFT frame is 512 ns in duration and contains 1024 IFFT time domain symbols. One symbol is transmitted per DAC sample. The OFDM data frame is preceded by a blank period of 23.1 µs duration. This blank period in conjunction with the header pulse shown in Fig. 2.2 (b) is used to synchronize the OFDM data frame at the receiver. The OFDM frame synchronization method is detailed in the Appendix section. The header pulse is followed by an 8 bit configuration code that uniquely identifies each bandwidth and modulation format combination used in every OFDM data frame. The receiver uses this configuration code to select the correct subcarriers and the de-modulators to be used for every OFDM data frame.

The Tx FPGA can transmit in any one of 18 unique configurations (as shown in Table 2.1), each configuration using a different number of subcarriers for text and video data or using a different modulation format for text data. Using the universal asynchronous receiver/transmitter (UART) serial communication protocol, the Tx FPGA can receive commands from a PC to transmit a given OFDM configuration. While the Tx FPGA is capable of generating an OFDM frame with a different configuration as compared to its predecessor frame i.e. a new configuration is possible every 82 µs, the UART communication baud rate of 115200 for the Tx FPGA allows for a new configuration only every 220 µs.

The Rx FPGA also uses the UART protocol at a baud rate of 460800 to send to a PC a periodic sample of either the received complex symbols, the demodulated text data or a stream

that can be used to estimate the bit error rate (BER) for the text data at the Rx. A copy of the ASCII encoded text data used at the Tx FPGA is stored at the Rx FPGA as a reference and the demodulated incoming text data is compared bit by bit with the reference data using an XOR operation. The data stream fed back over the serial port is the result of the XOR operation of the received and reference bits. Hence, in order to calculate the BER, a MATLAB script running on the PC connected to the Rx FPGA serial port counts the number of 1's in a given set of received bits. The ratio of the number of 1's to the total number of bits received in a given integration time is the BER of the system. With this method, a new BER value is computed about once every second.

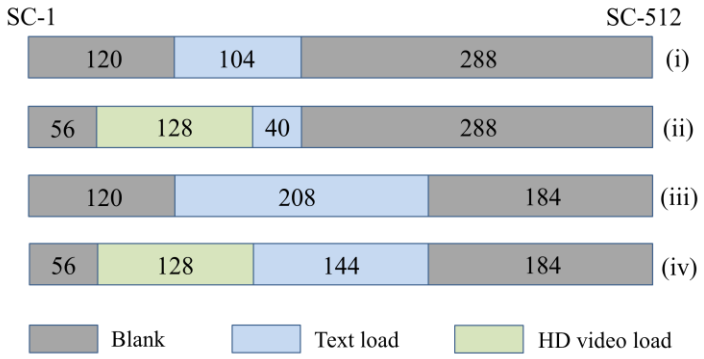

Fig. 2.3 Four OFDM configurations with different subcarrier allocations for text and video data, please refer to the Table 2.1 special notes for descriptions

Configuration Code (decimal)	**Configuration Code (binary)**	**Number of subcarriers for video, modulation format**	**Number of subcarriers for text, modulation format**	**Total bit rate (Mb/s), special notes**
128	1 000 000 0	0	104, BPSK	145.9, SC allocation depicted in Fig. 2.3 (i)
129	1 000 000 1	128, BPSK	40, BPSK	235.7, SC allocation depicted in Fig. 2.3 (ii)
130	1 000 001 0	0	160, BPSK	224.5
131	1 000 001 1	128, BPSK	96, BPSK	314.3
132	1 000 010 0	0	208, BPSK	291.8, SC allocation depicted in Fig. 2.3 (iii)
133	1 000 010 1	128, BPSK	144, BPSK	381.6, SC allocation depicted in Fig. 2.3 (iv)
144	1 001 000 0	0	104, QPSK	291.8, SC allocation depicted in Fig. 2.3 (i)
145	1 001 000 1	128, BPSK	40, QPSK	291.8, SC allocation depicted in Fig. 2.3 (ii)
146	1 001 001 0	0	160, QPSK	448.9
147	1 001 001 1	128, BPSK	96, QPSK	448.9
148	1 001 010 0	0	208, QPSK	583.6, SC allocation depicted in Fig. 2.3 (iii)
149	1 001 010 1	128, BPSK	144, QPSK	583.6, SC allocation depicted in Fig. 2.3 (iv)
160	1 010 000 0	0	104, 8-QAM	437.7, SC allocation depicted in Fig. 2.3 (i)
161	1 010 000 1	128, BPSK	40, 8-QAM	347.9, SC allocation depicted in Fig. 2.3 (ii)
162	1 010 001 0	0	160, 8-QAM	673.4
163	1 010 001 1	128, BPSK	96, 8-QAM	583.6
164	1 010 010 0	0	208, 8-QAM	875.4, SC allocation depicted in Fig. 2.3 (iii)
165	1 010 010 1	128, BPSK	144, 8-QAM	785.6, SC allocation depicted in Fig. 2.3 (iv)

Table 2.1 Configuration details and bit rates for the direct detection OFDM architecture

2.3 Proposed real-time elastic resource allocation scheme

The proposed elastic resource allocation scheme is shown in Fig. 2.4, and features dynamic OFDM subcarrier modulation format allocation based on optical signal-to-noise ratio (OSNR) requirements to keep the bit error ratio (BER) below a target threshold. It also features traffic-type specific dynamic bandwidth (BW) allocation based on real-time data load, where, in this case, high definition (HD) video and ASCII-encoded text are used as the two data traffic types.

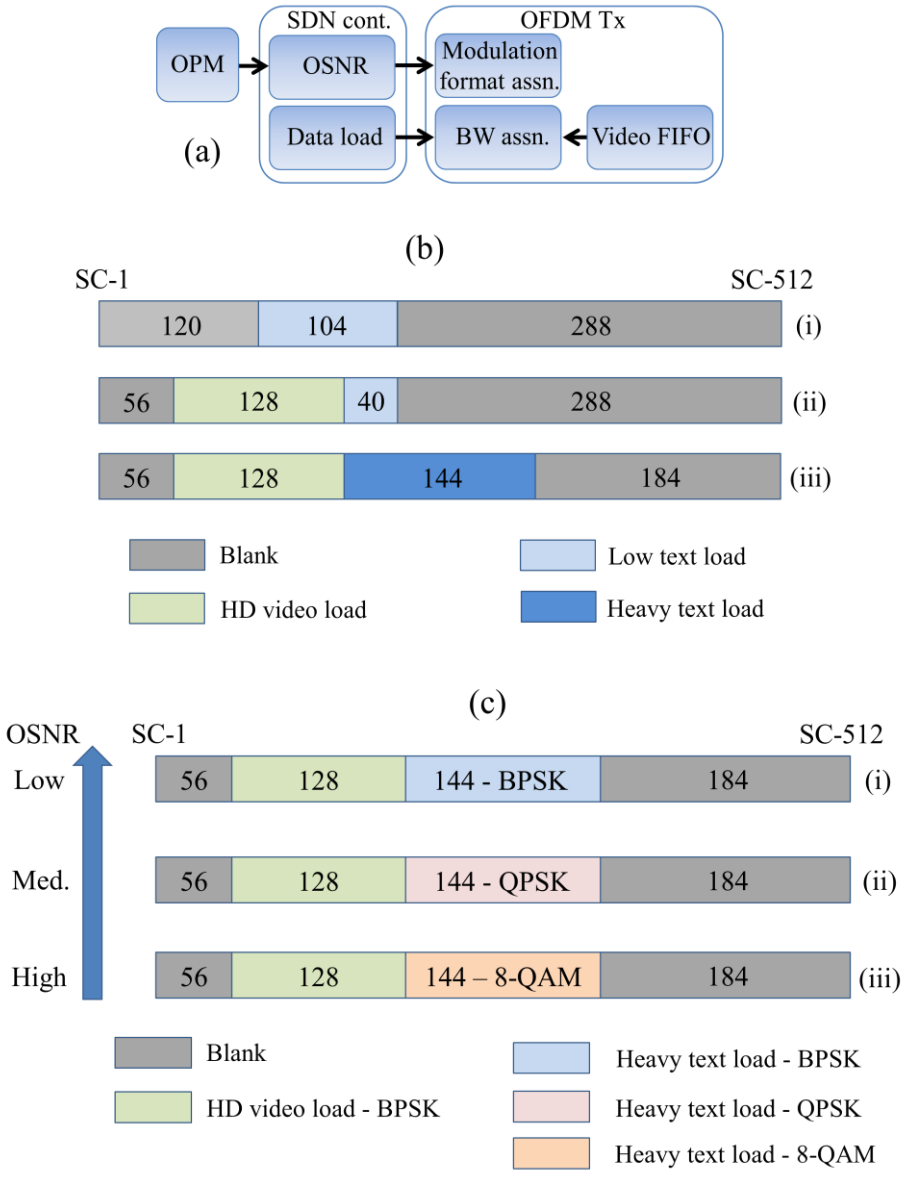

Fig. 2.4 (a) Top-level schematic; OFDM subcarrier assignment based on (b) data load and (c) OSNR.

As shown in Fig. 2.4 (a), a FIFO memory element is used at the Tx to regulate the burst nature of the incoming video stream; the FIFO and the data load from the SDN controller decide the subcarrier BW assignment and the OSNR input decides the modulation format for subcarriers carrying text data. Fig. 2.4 (b) shows some of the implemented real-time BW assignment configurations, such that: (i) when there is no HD video, only a low text load, only 104 out of 512 subcarriers are used; (ii) when there is a low text load and the FIFO is partially filled by a burst of incoming video data, 64 OFDM subcarriers are turned on and another 64 subcarriers are re-assigned to transmit video instead of text, and (iii) when there is HD video and a heavy text load, the SDN controller turns on an additional 104 blank subcarriers to support the heavy text load. In Fig. 2.4 (c), the modulation format of the text data stream is adjusted dynamically based on OSNR readings that the OFDM Tx receives from the SDN controller; the system moves to lower order modulation formats when OSNR degrades in order to keep BER below a defined threshold. The video stream is modulated using BPSK in all cases, while the modulation format for text ranges from BPSK to 8-QAM depending on OSNR. The SDN controller thus communicates with both top level applications (i.e. HD video and text) and the underlying real-time OFDM transmitter in real-time.

2.4 Experiment setup

Fig. 2.5 shows the experiment setup. An Integrable Tunable Laser Assembly (ITLA) tuned to λ = 1550.12 nm with 13 dBm output power served as the optical carrier for intensity modulation of the dynamically-controlled OFDM signal from the OFDM Tx (Fig. 2.1 (a)). An amplified spontaneous emission (ASE) source and an optical amplifier connected to a 50:50 coupler (Cp.) were used to add a variable amount of noise into the system. The attenuator α before the coupler in conjunction with the 50:50 coupler and 90:10 splitter emulate a 1:16 passive split (with 12 dB attenuation). The splitter diverts the bulk of the optical power to a 20 km SSMF spool via a 0.4 nm bandwidth optical bandpass filter (BPF) centered at 1550.12 nm, with the BPF also used to filter out out-of-band noise. Double side-band (DSB) optical OFDM transmission was used in this experiment since it allowed for a simpler transmitter architecture and the fiber length was sufficiently short [36]. Following SSMF transmission, the OFDM signal was optically amplified and photodetected by a 50 GHz PIN photodiode connected to the OFDM Rx (Fig. 2.1 (b)). The

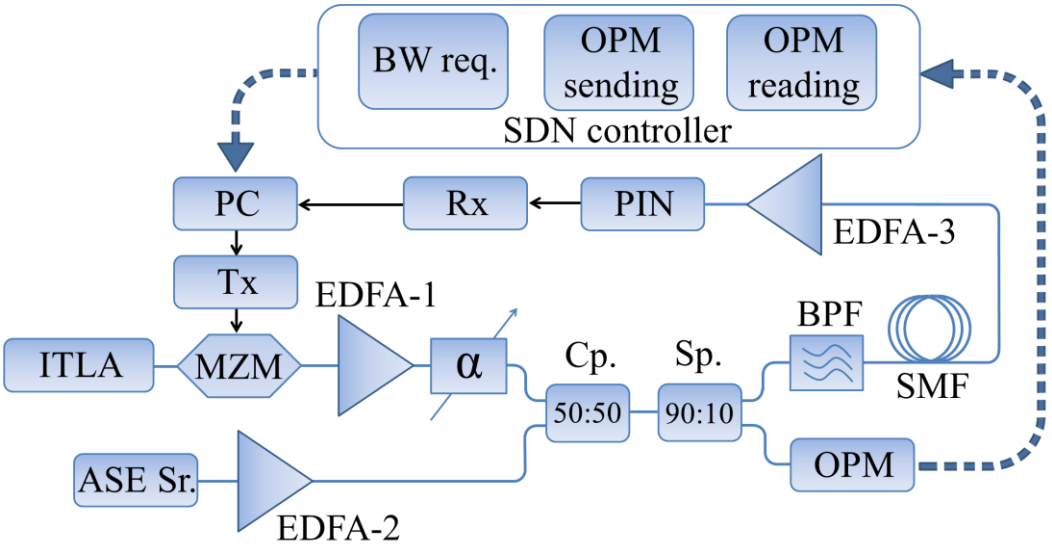

Fig. 2.5 Experiment setup: The thin light blue lines are optical links, the black lines are electrical links and the thick blue dashed lines are logical connections.

real-time BER computed in the OFDM Rx for the text data stream was sent to the PC for visual display. Part of the optical power after the 90:10 splitter in Fig. 2.5 was used for the Optical Performance Monitoring (OPM) circuit [37]. The OPM system thus continuously measured transmission OSNR and this reading was then translated into the OpenFlow protocol by the augmented SDN controller. Then the reading was sent along with the OSNR thresholds and bandwidth requirement to the OFDM Tx MATLAB interface running on a PC connected via serial communication to the Tx FPGA. The MATLAB interface uses this real-time OSNR data and thresholds to dynamically change the OFDM modulation format if required, by issuing commands via the serial port to the Tx FPGA. In the experimental scheme, 240 out of 512 total OFDM subcarriers were turned off throughout, while 128 subcarriers were used to carry HD video, and 40-208 subcarriers carried ASCII-encoded text based on various data load conditions (Fig. 2.4). The total bit rate of the system varied from 145.9 Mb/s with low text load (BPSK modulation) and no video, to 785.63 Mb/s with heavy text load (8-QAM modulation) and video, to 875.42 Mb/s with heavy text load (8-QAM modulation) and no video.

2.5 Results

Fig. 2.6 displays the BER performance for real-time OFDM transmission with BPSK, QPSK and 8-QAM modulation formats over a range of OSNR values for heavy text load with HD video. A BER threshold of 1.1×10^{-5} was used in the experiment, such that the OSNR threshold for switching from 8-QAM to QPSK was 8 dB (OSNR threshold 2) and the threshold for switching from QPSK to BPSK was 3.5 dB (OSNR threshold 1). These thresholds are used to automatically switch the modulation format of the text data stream based on real-time OSNR readings from the SDN controller, i.e. dynamic mode. One can see that the BER in the dynamic

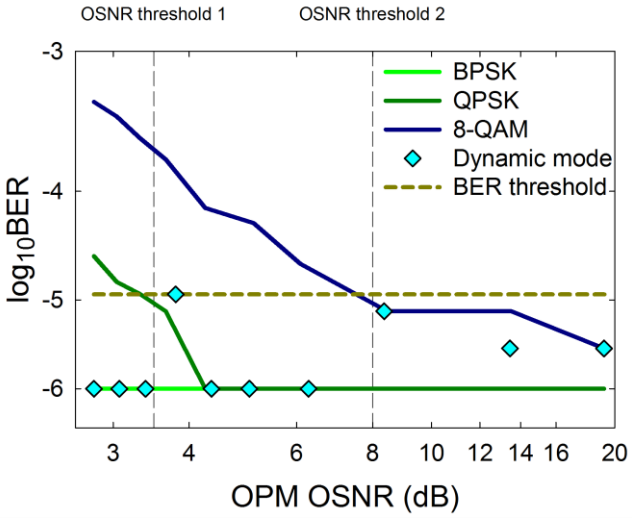

Fig. 2.6 BER versus OSNR for various modulation schemes.

mode never exceeded the BER threshold over the measured OSNR range. The quality of the HD video stream was also observed to be good in all cases. The BER threshold value of 1.1×10^{-5} was selected as a reference case.

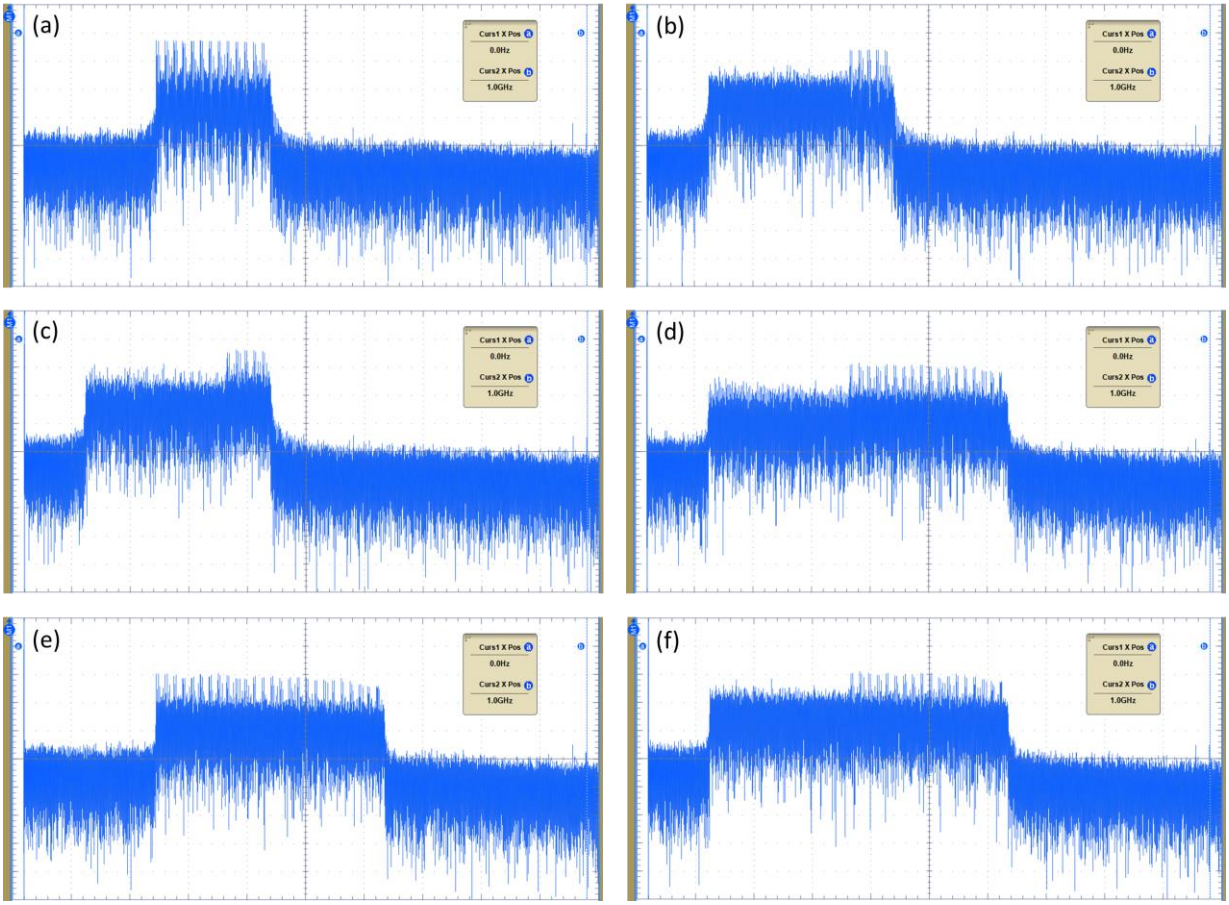

Fig. 2.7 OFDM electrical spectrum for (a) config. 128: low text load (BPSK) with no video (b) config. 129: low text load (BPSK) with video (BPSK) (c) config. 145: low text load (QPSK) with video (BPSK) (d) config. 149: heavy text load (QPSK) with video (BPSK) (e) config. 164: heavy text load (8-QAM) with no video (f) config. 165: heavy text load (8-QAM) with video (BPSK). The horizontal scale in all the plots is 104 MHz/div.

Fig. 2.7 displays the electrical spectrum of the OFDM signal for various configurations. Since the subcarrier BW assignment for video data is based on the presence of data in the video FIFO, the Tx FPGA is capable of switching from a configuration that does not carry video (Fig. 2.7 (a) and (e) for example) to a configuration that carries video (Fig. 2.7 (b) and (f) respectively) every OFDM frame i.e. every 82 μs. This real-time BW assignment demonstrates an important aspect of elastic optical networking.

2.6 FPGA utilization

OFDM_Tx_design Project Status (10/12/2013 - 14:12:52)			
Project File:	OFDM_Tx_design.xise	**Target Device:**	xc5vsx95t-2ff1136

Device Utilization Summary			
Slice Logic Utilization	**Used**	**Available**	**Utilization**
Number of Slice Registers	23,154	58,880	39%
Number of Slice LUTs	19,852	58,880	33%
Number of occupied Slices	8,665	14,720	58%
Number of bonded IOBs	274	640	42%
Number of BlockRAM/FIFO	108	244	44%
Total Memory used (KB)	3,276	8,784	37%
Number of BUFG/BUFGCTRLs	9	32	28%
Number of IDELAYCTRLs	3	22	13%
Number of DSP48Es	320	640	50%
Number of PLL_ADVs	1	6	16%
Number of TEMACs	1	2	50%

Table 2.2 The FPGA utilization for the OFDM Tx FPGA

OFDM_Rx_design Project Status (10/07/2013 - 13:23:40)			
Project File:	OFDM_Rx_design.xise	**Target Device:**	xc5vsx95t-2ff1136

Device Utilization Summary			
Slice Logic Utilization	**Used**	**Available**	**Utilization**
Number of Slice Registers	22,865	58,880	38%
Number of Slice LUTs	19,352	58,880	32%
Number of occupied Slices	8,559	14,720	58%
Number of bonded IOBs	203	640	31%
Number of BlockRAM/FIFO	105	244	43%
Total Memory used (KB)	3,078	8,784	35%
Number of BUFG/BUFGCTRLs	13	32	40%
Number of IDELAYCTRLs	4	22	18%
Number of DSP48Es	352	640	55%
Number of PLL_ADVs	2	6	33%
Number of TEMACs	1	2	50%

Table 2.3 The FPGA utilization for the OFDM Rx FPGA

Tables 2.2 and 2.3 depict the FPGA utilization for the Tx and Rx FPGAs respectively. The hardware block that performs the IFFT/FFT computations is the DSP48E block. Its utilization is between 50% and 55% for the Tx and Rx. This allows room for additional signal processing in the Tx and Rx designs for future use.

We can compare the FPGA utilization of my design with an implementation of the Radix2 Multi-Path Delay Commutator kernel (Radix2-MDC) [38] on a Virtex-5 FPGA. Here a parallel 1024 point FFT architecture is implemented, we shall consider the 8x architecture as it is similar to the IFFT/FFT implementation in my design. The Radix2-MDC design requires 260 DSP48E blocks (compared to 320 to 352 in my design) and can be clocked at up to 280 MHz (compared to 270 MHz in my design). My design has not been optimized for lower hardware use as it uses 8 instantiations of the Xilinx Fast Fourier Transform v7.1 LogiCORE IP [33] in pipelined, streaming I/O mode. Hence, the DSP48E hardware utilization in my design is at least 23% higher than the more optimized Radix2-MDC design. Thus, there is room for further optimization of my design, enabling it to be implemented on smaller FPGAs.

2.7 Energy efficiency calculations

Tables 2.4 – 2.7 show the power consumption estimates for sub-systems of the OFDM Tx and Rx. The FPGA power consumption estimates in Table 2.4 and Table 2.6 are derived from the Xilinx XPower Analyzer tool that is part of the Xilinx ISE 13.4 System Edition package. The power consumption estimates for components in Table 2.5 and Table 2.7 (excluding the FPGA) are derived from the respective manufacturer datasheets.

FPGA resource	**Power consumption (W)**
Clocks	0.895
Logic	0.105
Signals	0.132
BRAMs	1.202
DSPs	0.053
PLLs	0.133
TEMACs	0.019
IOs	3.15221
Leakage	1.711
FPGA Total	**7.40221**

Table 2.4 OFDM Tx FPGA power consumption

Tx component	**Power consumption (W)**
FPGA Total	7.40221
DAC	1.15
ITLA	3.5
Modulator driver	4.9
EDFA	5
Transmitter Total	**21.95221**

Table 2.5 OFDM Tx power consumption

Energy/bit = Transmitter total power / maximum bit-rate for IMDD OFDM

= 21.95221 W / 875.42 Mbps

= 25.076 nJ/bit

Bits/Joule = 39.878 Mb/J

FPGA resource	Power consumption (W)
Clocks	0.913
Logic	0.101
Signals	0.133
BRAMs	1.167
DSPs	0.053
PLLs	0.219
TEMACs	0.019
IOs	2.49781
Leakage	1.645
FPGA Total	**6.74781**

Table 2.6 OFDM Rx FPGA power consumption

Rx component	Power consumption (W)
FPGA Total	6.74781
ADC	1.8
PIN photodiode	0.1
Receiver Total	**8.64781**

Table 2.7 OFDM Rx power consumption

Energy/bit = Receiver total power / maximum bit-rate for IMDD OFDM

= 8.64781 W / 875.42 Mbps

= 9.878 nJ/bit

Bits/Joule = 101.23 Mb/J

It can be seen in Table 2.4 and 2.6 that the input-output (IO) section is the single largest contributor to the FPGA power consumption for the Tx and Rx respectively. The bulk of the IO section services the connection between the FPGA and DAC/ADC and hence a higher energy efficiency can be expected from an application specific integrated circuit (ASIC) implementation of the OFDM system with integrated DACs/ADCs that will help reduce the utilization of energy hungry IO resources.

In order to compare the power consumption and energy efficiency of my IMDD OFDM system with commercially available networking equipment consisting of both transmitters and receivers, I consider the OFDM Tx and Rx as a single transceiver with parameters as follows

Total OFDM Tx and Rx power consumption = 21.95221 + 8.64781 = 30.60 W

Total OFDM Tx and Rx energy efficiency = 25.076 + 9.878 = 34.954 nJ/bit

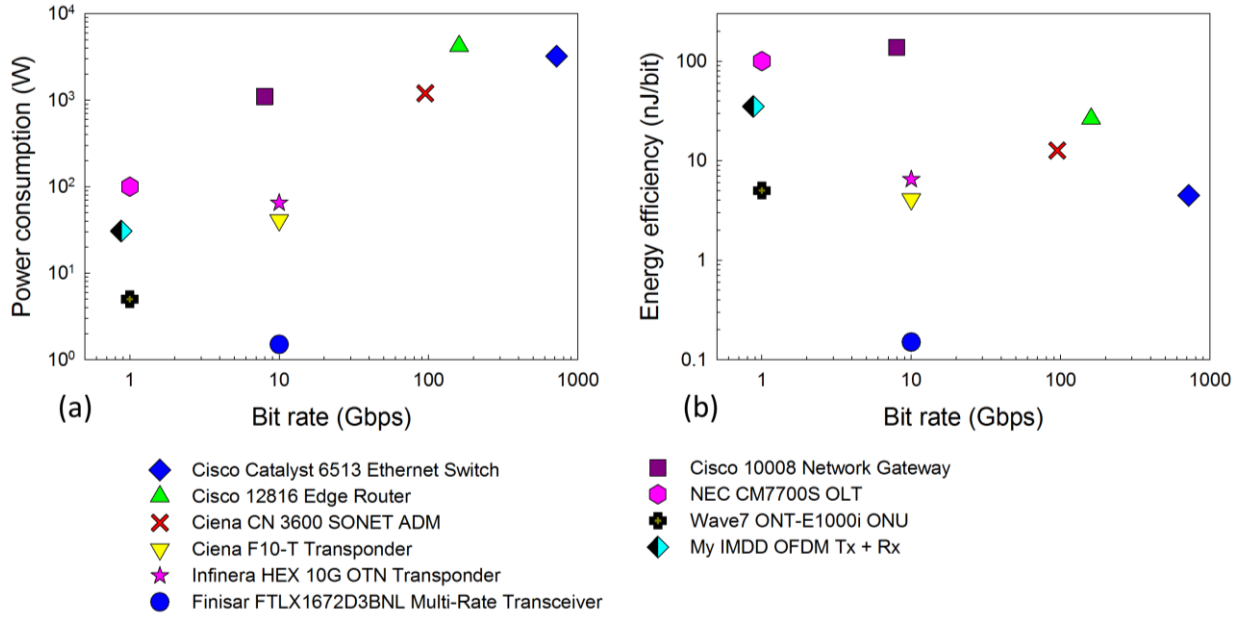

Fig. 2.8 The comparison between commercial networking equipment and my IMDD OFDM system for (a) power consumption and (b) energy efficiency, a lower energy efficiency number (in nJ/bit) is better. SONET – Synchronous optical network, ADM – Add-drop multiplexer, OTN – Optical transport network, OLT – Optical line terminal, ONU – Optical network unit. From [39-42].

Fig. 2.8 shows this comparison of the power consumption and energy efficiency. In Fig. 2.8 (a), we can see the general trend of higher power consumption with higher bit rate. Interestingly however, the energy efficiency at higher bit rates is at par or better as compared to lower bit rates as can be seen in Fig. 2.8 (b). The IMDD OFDM system supports a 1:16 passive split as explained in the experiment setup in Sec. 2.4. Hence the IMDD OFDM system is closer in operational capability to a passive optical network (PON) OLT such as the NEC CM7700S OLT. In Fig. 2.8, we can see that the IMDD OFDM system has about a third of the power consumption of the NEC CM7700S OLT and hence is about three times as efficient as the NEC CM7700S OLT. The IMDD OFDM system consumes six times as much power as the Wave7 ONT-E1000i ONU and hence has only about a seventh of the energy efficiency of the Wave7 ONT-E1000i ONU. An ASIC implementation of the OFDM signal generation and processing can help bring

the energy efficiency of an OFDM system closer to the energy efficiency of the commercially available ONU and transponders depicted in Fig. 2.8.

2.8 Conclusions

I have experimentally demonstrated real-time software-defined dynamic resource allocation for OFDM-based PON that is capable of dynamic alteration of subcarrier assignment and modulation format using OpenFlow to keep BER below designated threshold over a wide range of OSNR values for 20 km SSMF transmission. Based on real-time OSNR readings, the OpenFlow-based SDN controller issues dynamic resource allocation commands to the real-time OFDM Tx within seconds. A load based re-assignment of subcarriers for bursty video stream transmission was also demonstrated. This dynamic alteration of parameters results in better spectral utilization and higher error resilience in the presence of impairments. The proposed approach is thus highly-promising for supporting interoperable on-demand resource provisioning in next-generation OFDM-based optical access networks.

Chapter 3

Unified direct and coherent detection OFDM optical transmission scheme

3.1 Introduction

Self-coherent OFDM has been the subject of ongoing research primarily due to its potential for simplified receiver architecture [43]. Transmitting the carrier, that serves as the local oscillator (LO) at the receiver side, has been achieved by using spectral [43], temporal [44] or polarization [45] multiplexing or by using a virtual carrier [46]. Each method has its own drawbacks, such as: (i) the need for narrow bandwidth optical filtering for carrier extraction and a guard band placed between signal and carrier in both spectral multiplexing and the virtual carrier methods, (ii) reduction of the transmission capacity in temporal multiplexing, and (iii) the need for polarization tracking or polarization diversity reception in polarization multiplexing.

Experiments with spectrally overlapping polarization multiplexed OFDM streams rely on polarization diversity reception, complex digital signal processing (DSP) and periodic training symbols [47, 48], or on the use of narrow band optical filtering to separate the carrier, as well as the use of additional filtering to separate the undesirable OFDM stream originating from the orthogonal polarization [49]. It is important to note that field-programmable gate array (FPGA) based real-time coherent systems [50] have limited hardware resources and implementing complex DSP [47, 48] on FPGAs may present a significant challenge. Simultaneous operation of legacy direct detection receivers and newer coherent detection receivers using 8 quadrature amplitude modulation (QAM) derived amplitude shift keying (ASK) and regular 8-QAM modulation formats respectively has also been proposed [51].

In this chapter, I demonstrate a novel scheme of a unified direct and coherent OFDM transmitter (Tx) that is able to communicate simultaneously with a simple direct detection receiver and also with a

coherent receiver. Such an approach provides scalability, flexibility, and higher efficiency since the detection scheme can be readily interchanged. The use of self-coherent OFDM in conjunction with optical polarization tracking in this setup greatly simplifies the OFDM receiver design and FPGA implementation.

3.2 The unified Tx concept

The concept of the unified transmitter that communicates simultaneously with direct/coherent receivers is shown in Fig. 3.1. The two spectral sidebands around the optical carrier of a coherent OFDM signal can be independently turned on/off by configuring the lower and upper half of the OFDM subcarriers. Turning on just the lower (or upper) subcarriers produces a single sideband (SSB) OFDM signal as shown in Fig. 3.1 (a), (ii). This signal does not require a coherent receiver. This can be understood by considering the fact that in the spectral domain, the SSB-OFDM signal resides only on one side of the optical carrier, thus down-conversion is essentially heterodyne detection for SSB-OFDM and a single photodiode is sufficient to generate the down-converted RF channel containing all the information encoded in the SSB signal. The presence of a carrier in the orthogonal polarization enables us to use a direct detection receiver based on a single polarization analyzer followed by a single photodiode. When a double sideband (DSB) OFDM signal is required, both the lower and the upper half of the subcarriers are turned on as in Fig. 3. 1 (b). A DSB OFDM signal requires a coherent receiver shown in Fig. 3.1 (b); the DSB-OFDM signal and the carrier in the orthogonal polarization are used for self-coherent detection.

A conventional intensity modulation and direct detection (IMDD) OFDM scheme has a double sided signal spectrum around the optical carrier, the signal and carrier reside in the same polarization plane [Fig. 3.1 (a), (i)]. In the time domain, this translates to a carrier offset/bias that results in higher peak power in the OFDM waveform. Since the double-sided IMDD-OFDM signal spectrum carries identical information in each sideband, a single sideband transmission is sufficient for information integrity. By transmitting the carrier and signal in two orthogonal polarizations, as in Fig. 3.1 (a), (ii), we can eliminate the carrier bias, thus reducing the peak optical power and the impact of fiber nonlinearities [26].

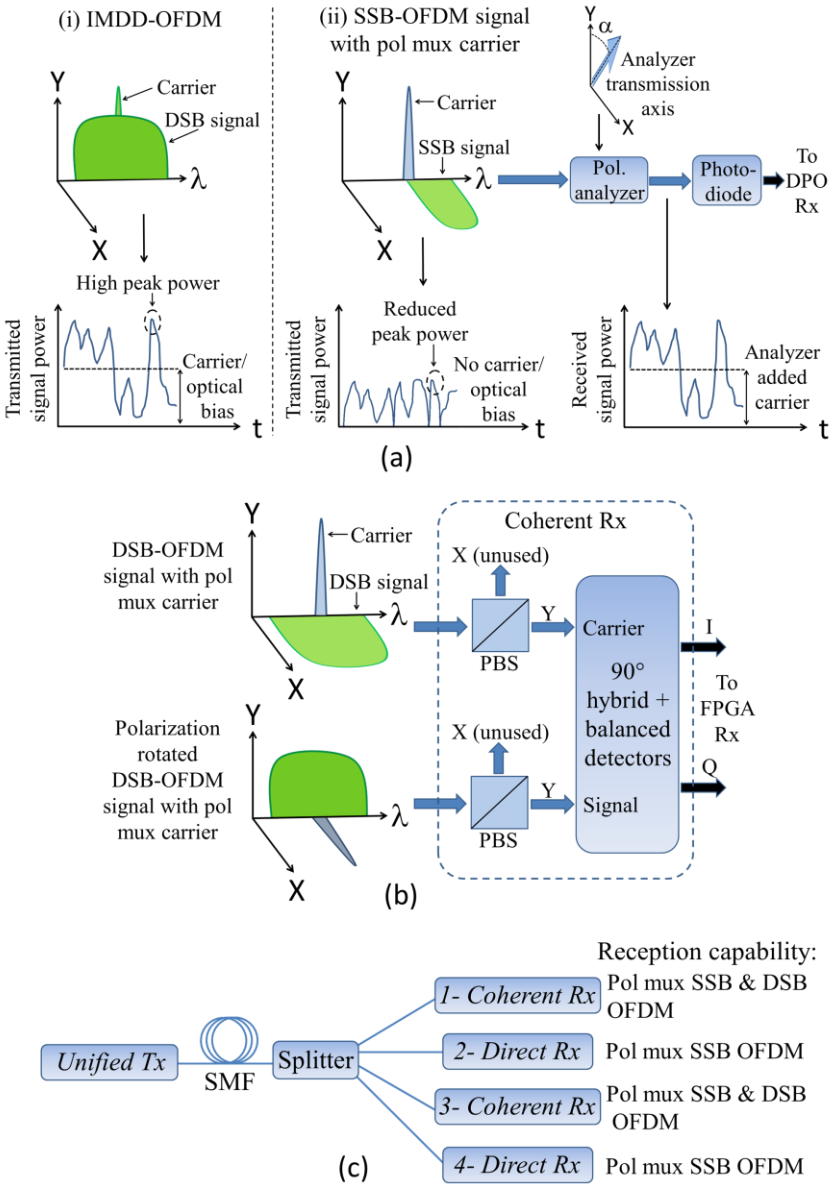

Fig. 3.1 The unified Tx concept: (a) the polarization multiplexed (pol-mux) SSB-OFDM waveform with direct detection using a polarization analyzer and a photodiode; signal is compared with the IMDD-OFDM waveform, (b) DSB-OFDM reception using an integrated coherent receiver with polarization beam splitters (PBS) to select the signal and carrier along the Y polarization, (c) a transmission setup with the unified transmitter (Tx) and both direct and coherent receivers (Rx). SMF – standard single-mode fiber.

Fig. 3.1 (c) shows a transmission setup with the unified transmitter communicating simultaneously with both direct and coherent receivers. The direct receivers are able to receive only SSB OFDM signals while the coherent receivers are able to receive both SSB and DSB OFDM signals. As the direct receivers

require a relatively simple optical front end that consists of a polarization analyzer and a photodiode, and just one analog-to-digital converter, direct receivers would be less expensive, although they would receive only at about half the bit-rate of coherent receivers. Thus, one could set up a network with lower cost direct receivers (transceivers with direct receivers, to be more precise) for lower bit rates and coherent receivers (transceivers with coherent receivers) for higher bit rates. One could then incrementally replace direct receivers with coherent receivers when higher bit rates are needed. Such an interchangeable receiver solution would enable a trade-off between bit-rate and equipment cost and allow for higher flexibility and bit-rate scalability in network deployment and upgrade.

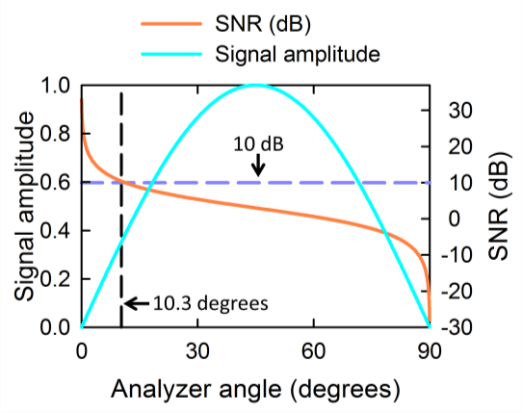

Fig. 3.2 The determination of the optimum analyzer angle.

The optimum value α_{opt} of the angle α between the analyzer transmission axis and the carrier polarization axis can be determined by considering the sum of the signal and carrier electric fields projected on the analyzer transmission axis and then squaring the sum, as we are using a square law detector (i.e. a photodiode), so we have that

$$\begin{aligned}&\left[E_{carr}\cdot e^{j\cdot\omega_{carr}\cdot t}\cdot\cos\alpha + E_{sig}\cdot e^{j\cdot\omega_{sig}\cdot t}\cdot\sin\alpha\right]^2\\&\quad= E_{carr}^2\cdot\cos^2\alpha + E_{sig}^2\cdot\sin^2\alpha\\&\quad+ 2\cdot E_{sig}\cdot E_{carr}\cdot\cos\left[\left(\omega_{carr}-\omega_{sig}\right)\cdot t\right]\cdot\cos\alpha\cdot\sin\alpha\end{aligned}\qquad(3.1)$$

where E_{sig} and E_{carr} are the peak electric field amplitudes of the signal and carrier, respectively; ω_{carr} and ω_{sig} are the angular frequencies of the carrier and signal, respectively; and t is the time variable. The product $S_{sig\text{-}carr} = 2\,E_{sig}\,E_{carr}\cos[(\omega_{carr} - \omega_{sig})\,t]\cos\alpha\sin\alpha$ contains the desired signal, while $N_{sig\text{-}sig} = E_{sig}^2\sin^2\alpha$ represents the noise term. In order to ensure adequate reception quality, we specify that the signal to noise ratio (SNR) $S_{sig\text{-}carr}/N_{sig\text{-}sig} > 10$, while simultaneously maximizing the signal amplitude

$S_{sig\text{-}carr}$. This is represented graphically in Fig. 3.2. With this condition, and assuming that $E_{sig} = E_{carr}$, I applied numerical analysis and found that $\alpha_{opt} = 10.3$ °.

3.3 FPGA architecture for coherent detection OFDM

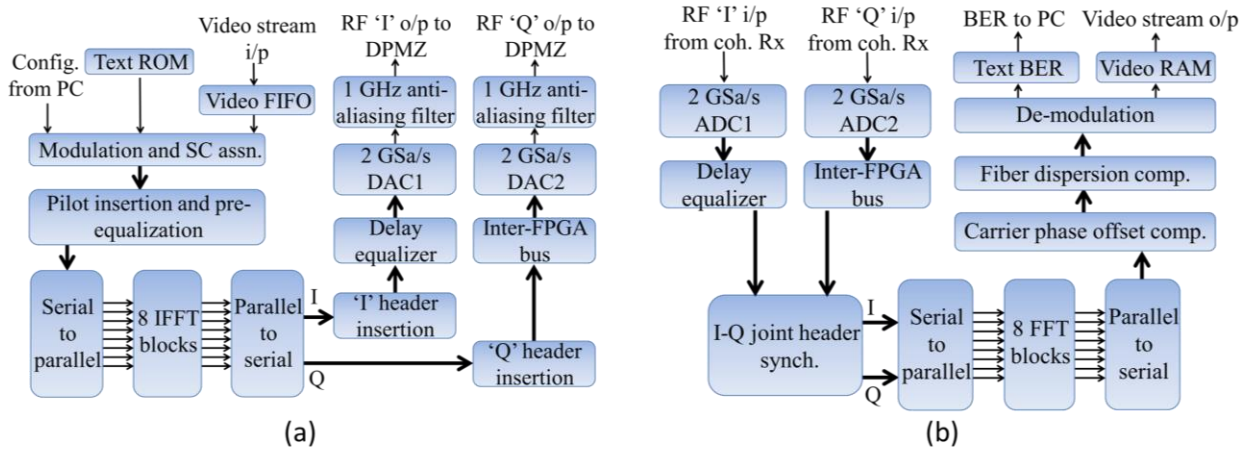

Fig. 3.3 (a) The unified OFDM Tx FPGA implementation; (b) The OFDM receiver (Rx) FPGA implementation, only carrier phase offset and fiber dispersion compensation are necessary and are implemented, thus simplifying the FPGA Rx design. (PC – personal computer).

I implemented a real-time coherent OFDM transmitter on an FPGA system with two digital-to-analog converters (DACs) clocked at 2 GSa/s producing in-phase (I) and quadrature (Q) OFDM outputs. Eight parallel 512-point inverse fast Fourier transform (IFFT) hardware blocks, each clocked at 250 MHz, produce a complex-valued OFDM signal with a maximum of 512 subcarriers (Fig. 3.3 (a)). Each subcarrier has a bandwidth of 3.91 MHz. The subcarriers are turned on/off to produce either an SSB or a DSB OFDM signal and also to meet text and video traffic load in real time, as shown in Fig. 3(a). Similar to the direct detection design, the text from commonly available literature encoded in ASCII form is used as the text load, while the video load is generated by a high definition (HD) streaming video source (VLC media player) over an Ethernet line from the PC running VLC to the Tx FPGA.

Fig. 3.4 shows the FPGA system used to implement the coherent OFDM Tx and Rx. The FPGA system has 4 FPGAs, 2 DACs and 2 analog to digital converters (ADCs). Each FPGA is connected to either a DAC or an ADC. At the OFDM Tx, the entire OFDM signal processing takes place on the FPGA 'A' as denoted in Fig. 3.4. The DAC (DAC1) connected to this FPGA is used to output the 'I' component of the complex OFDM signal. The 'Q' component that is generated at FPGA 'A' travels via the inter-

FPGA bus (Fig. 3.3 (a) and Fig. 3.4) to FPGA 'D' and then to DAC2. No signal processing occurs on the FPGA 'D'. For the OFDM Rx, the bulk of the OFDM signal processing takes place on the FPGA 'B' as denoted in Fig. 3.4. The ADC (ADC1) connected to this FPGA is used to receive the 'I' component of the complex OFDM signal. The 'Q' component is received at ADC2 connected to FPGA 'C' and travels via the inter-FPGA bus (Fig. 3.3 (b) and Fig. 3.4) to FPGA 'B'. OFDM frame synchronization for the 'Q' component is the only signal processing that takes place on the FPGA 'C'.

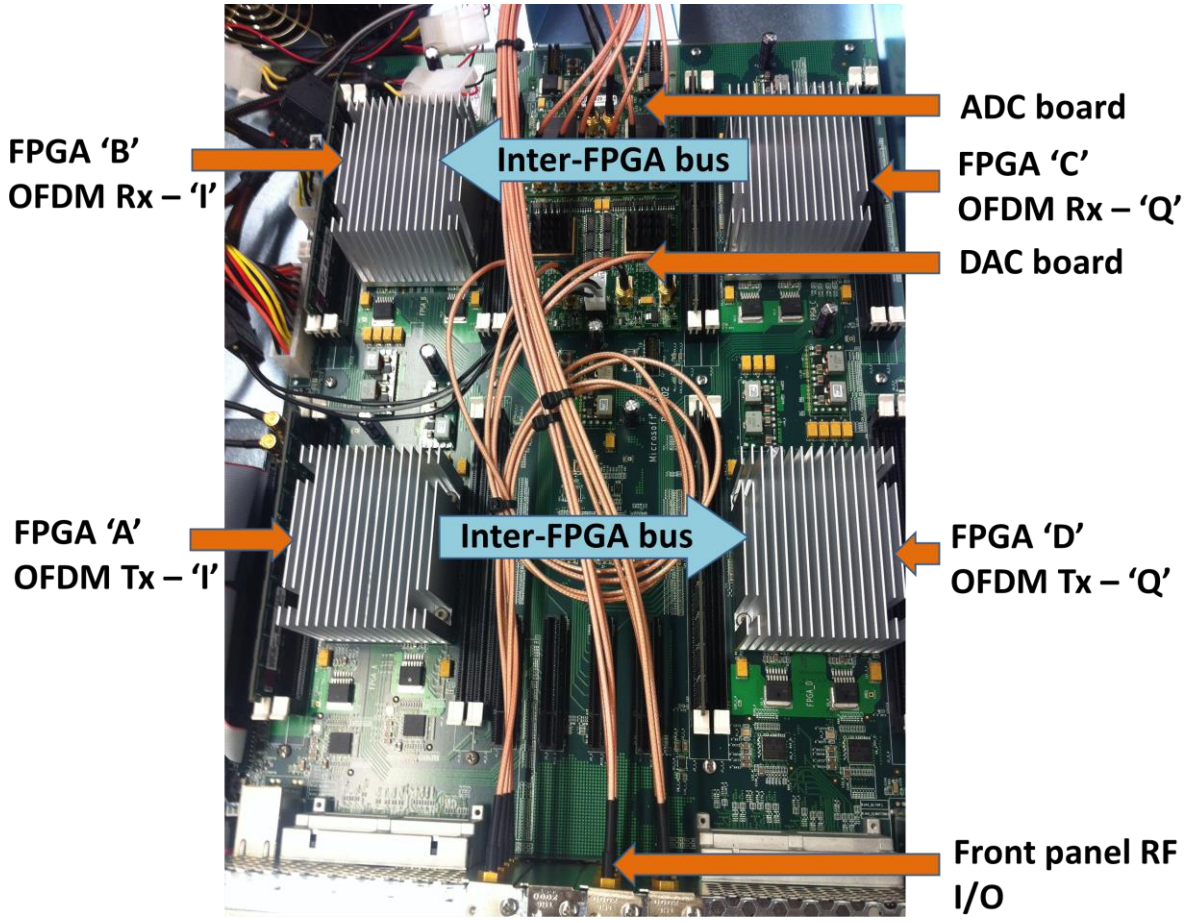

Fig. 3.4 The photograph of the FPGA system on which the OFDM Tx and Rx are implemented.

The Tx can transmit in any one of 12 unique configurations (as shown in Table 3.1), each configuration using a different number of subcarriers for text and video data or using a different modulation format for text data.

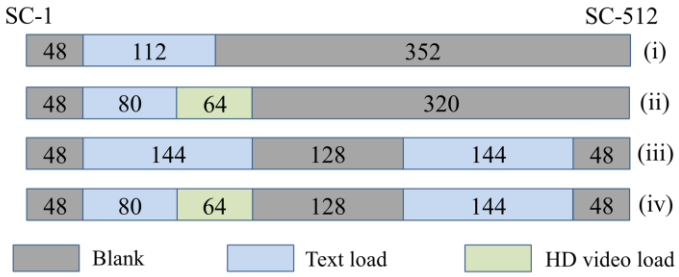

Fig. 3.5 The subcarrier (SC) loading: (i) SSB-OFDM configuration with the lower half of the SCs carrying text data, (ii) SSB-OFDM configuration with the lower half of SCs carrying both text and video data, (iii) DSB-OFDM configuration with both lower and upper half of the SCs carrying text data, (iv) DSB-OFDM configuration with both text and video data.

Configuration Code (decimal)	**Configuration Code (binary)**	**Number of subcarriers for video, modulation format**	**Number of subcarriers for text, modulation format**	**Total bit rate (Mb/s), special notes**
128	1 000 000 0	0	112, BPSK	414.9, SSB, SC allocation depicted in Fig. 3.5 (i)
129	1 000 000 1	64, BPSK	80, BPSK	533.5, SSB, SC allocation depicted in Fig. 3.5 (ii)
130	1 000 001 0	0	176, BPSK	652.1, DSB (partial)
131	1 000 001 1	64, BPSK	128, BPSK	711.4, DSB (partial)
132	1 000 010 0	0	288, BPSK	1067.1, DSB (full), SC allocation depicted in Fig. 3.5 (iii)
133	1 000 010 1	64, BPSK	224, BPSK	1067.1, DSB (full), SC allocation depicted in Fig. 3.5 (iv)
144	1 001 000 0	0	112, QPSK	829.9, SSB, SC allocation depicted in Fig. 3.5 (i)
145	1 001 000 1	64, BPSK	80, QPSK	829.9, SSB, SC allocation depicted in Fig. 3.5 (ii)
146	1 001 001 0	0	176, QPSK	1304.2, DSB (partial)
147	1 001 001 1	64, BPSK	128, QPSK	1185.6, DSB (partial)
148	1 001 010 0	0	288, QPSK	2134.1, DSB (full), SC allocation depicted in Fig. 3.5 (iii)
149	1 001 010 1	64, BPSK	224, QPSK	1897, DSB (full), SC allocation depicted in Fig. 3.5 (iv)

Table 3.1 Configuration details and bit rates for the coherent detection OFDM architecture

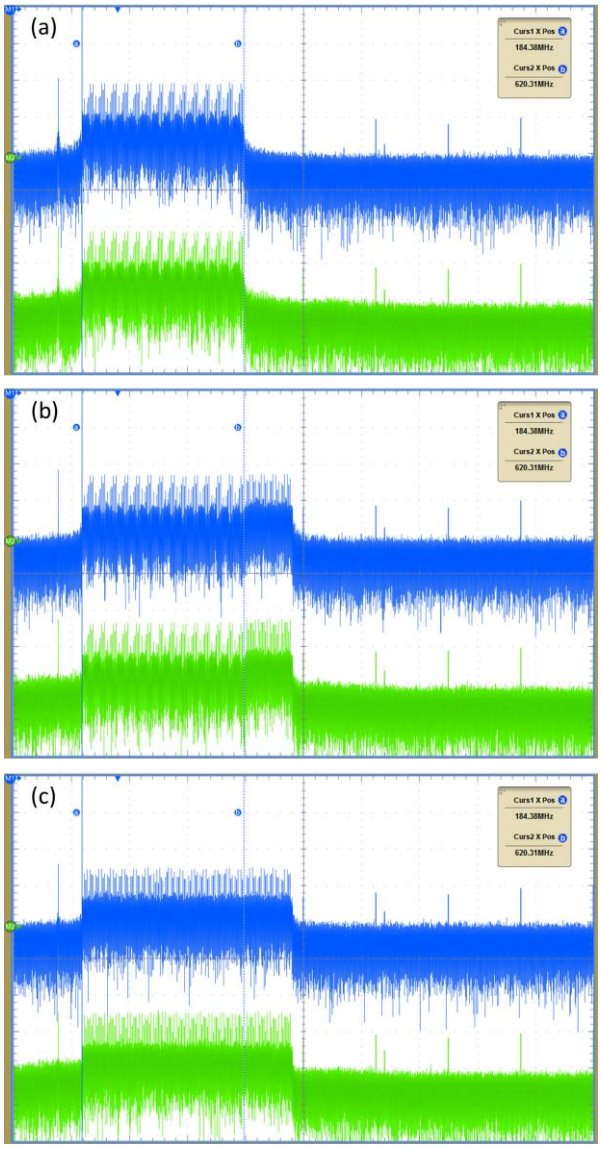

Fig. 3.6 I and Q OFDM electrical spectra for (a) configuration 144: SSB with text load (QPSK) and no video. (b) configuration 146: DSB (partial) with text load (QPSK) and no video. (c) configuration 148: DSB (full) with text load (QPSK) and no video. The horizontal scale for all three plots is 156 MHz/div.

OFDM frame synchronization is an important part of OFDM reception and I have defined specific hardware on the OFDM Rx FPGAs (i.e. FPGA 'B' and FPGA 'C') to perform frame synchronization. The details of this method of frame synchronization are explained in the Appendix chapter.

3.4 Experimental demonstration of the unified transmission scheme

3.4.1 Experiment setup

The unified transmitter is implemented by using a dual-parallel Mach-Zehnder (DPMZ) modulator with both I and Q arms biased at null. The unmodulated carrier (1550.12 nm wavelength) is combined with the

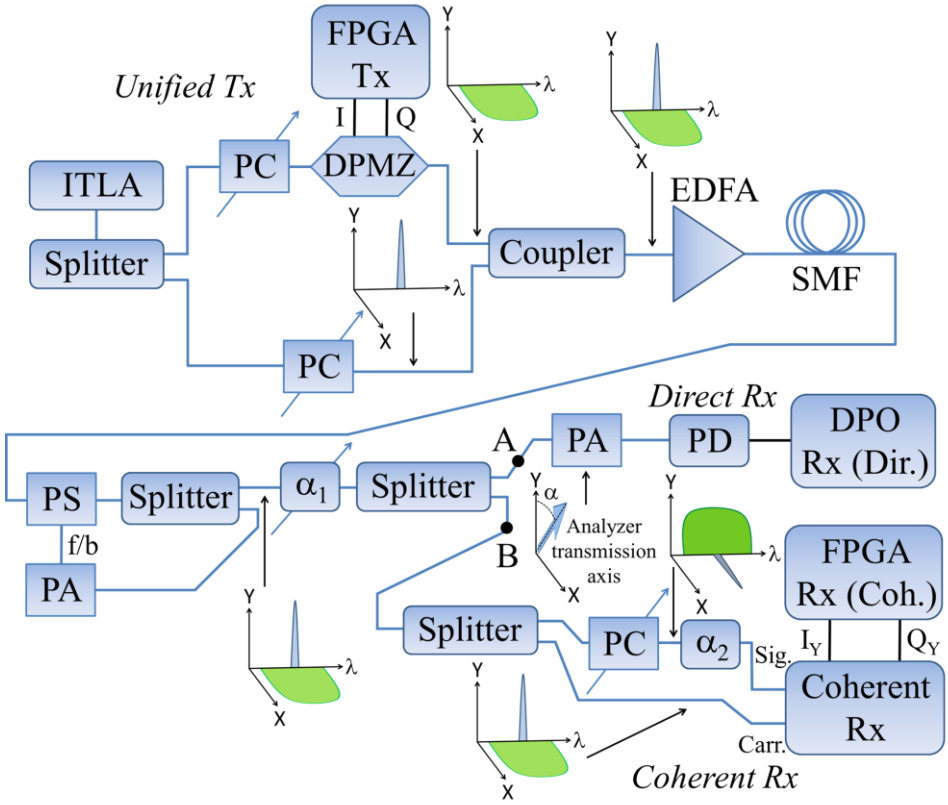

Fig. 3.7 The experiment setup for unified transmission – ITLA-Integrable tunable laser assembly; PC-polarization controller; PS-polarization stabilizer i.e. polarization tracking system; PA-polarization analyzer; PD-photodiode.

modulated signal in orthogonal polarization to produce the polarization multiplexed composite signal. I minimized the path length difference between the signal/DPMZ arm and the carrier arm to minimize the frequency offset between carrier and signal center frequencies before pol-mux. An erbium doped fiber amplifier (EDFA) is used to launch the composite signal into the fiber at a specified power (between 10 dBm and 17 dBm). A commercially available polarization tracking system is used in the transmission path containing 20 km of standard single-mode fiber (SMF). Using the feedback that is routed through a polarization analyzer, the polarization tracker continuously compensates for the random polarization drift

in the fiber span and maintains a constant polarization state at the polarization tracker output. The polarization tracker has a state of polarization response time of less than 4 ms and has a state of polarization rotation tracking speed of 32π radians/s.

A variable optical attenuator α_1 is used to vary the optical power of the composite signal that is split into two paths, one to a direct detection system and the other to a coherent detection system. While I envision a polarization tracker positioned before the optical front end of every direct or coherent receiver in the network, in this experiment I have used a single polarization tracker placed before both receivers. The direct detection path consists of a polarization analyzer with its transmission axis set to angle α_{opt} = 10 °, as explained in Sec. 3.2. The analyzer is followed by a PIN photodiode and then connected to a digital phosphor oscilloscope (DPO) with a sampling rate of 25 GSa/s. An OFDM receiver is implemented in MATLAB running on the DPO; the 25 GSa/s DPO waveform is decimated to 2 GSa/s before OFDM processing begins. The DPO based OFDM receiver does not process video data as it samples only 80 μs segments of the received OFDM waveform, about once every second and hence lacks the necessary throughput. The coherent detection path consists of a coherent optical receiver capable of handling polarization multiplexed inputs. A fixed optical attenuator α_2 is used to set the optical signal power to be 13 dB lower than the optical carrier power for proper coherent detection. The I and Q RF outputs of the coherent receiver are connected to the 2 GSa/s analog-to-digital converter (ADC) inputs of the receiver FPGA system. As a functional inverse of the OFDM transmitter, the receiver consists of eight parallel 512-point fast Fourier transform (FFT) blocks (Fig. 3.3 (b)). The OFDM signal is transmitted in 54.7 μs blocks each containing 213 IFFT frames. One IFFT frame consists of 512 OFDM time-domain symbols. A pilot symbol is transmitted every IFFT frame to enable carrier phase offset compensation, while the first IFFT frame in every 54.7 μs block contains pilot symbols for fiber dispersion compensation. Each compensation method is implemented using a single complex multiplication for every subcarrier/FFT output symbol (i.e. one-tap equalization). The FPGA based real-time coherent receiver is able to process video data as it continuously samples the received OFDM waveform and has the necessary throughput. It is important to note that since we are using self-coherent detection, which ensures a negligible frequency offset between the carrier and the signal center frequencies, we are not required to implement carrier frequency offset compensation in the FPGA Rx. In addition, since polarization tracking is handled by a dedicated polarization stabilization system, no additional FPGA resources need to be committed to digital compensation of polarization drift and only 2 ADCs are needed

as compared to 4 ADCs that would be needed for polarization diversity reception. These factors enable a simplified receiver architecture.

I setup the experiment as shown in Fig. 3.7 and varied the OFDM signal bandwidth at the unified Tx to produce SSB or DSB OFDM signals. The optical launch power into the fiber was 10 dBm. The direct receiver was able to successfully demodulate all SSB-OFDM signals, while the coherent receiver was able to demodulate both SSB and DSB OFDM signals. The quality of the video received by the FPGA Rx was excellent in both SSB and DSB OFDM configurations.

3.4.2 The polarization tracking setup used in the experiment

Fig. 3.8 shows the typical setup for a polarization tracking system. The light input with unstable polarization passes through a polarization controller (PC) and then part of the light is directed to the downstream optical setup (while a portion is diverted into a feedback loop). A polarization sensitive

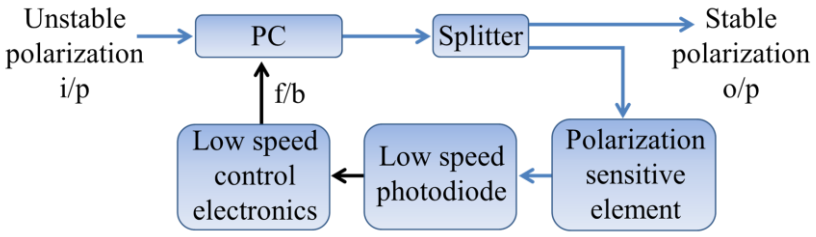

Fig. 3.8 The setup for a polarization tracking system.

element, such as a polarization analyzer or a polarization beam splitter, is used in the feedback loop so that a polarization dependent optical power is incident on the photodiode connected after the polarization sensitive element. The electrical output of the photodiode is used to generate a control signal for the polarization controller. The feedback loop operates to either minimize or maximize the optical power incident on the photodiode, depending on the tracking method chosen. This continuous feedback and control ensures a stable polarization at the output.

It is important to note that since the polarization of light at the output of a fiber (which is also the input to the polarization tracking system) changes over time in the microsecond to millisecond range, the photodiode and control electronics needed in the feedback path are required to have only an electrical bandwidth in the MHz range and a sampling rate in the MSa/s range. This can be compared with a receiver that employs polarization diversity reception and subsequent digital compensation of polarization

drift. Such a system would require twice the number of ADCs to receive both X and Y polarization signals as compared to the setup for receiving the X (or Y) polarization signal with polarization tracking. These ADCs would all have to be operating at the full sampling rate of the system which is typically in the GSa/s range. Given that high speed ADCs are expensive, one would want to minimize their count (especially at higher sampling rates), which we are able to achieve in our scheme. Polarization tracking modules that are suitable for integration in receivers are now commercially available. The control electronics in these modules are low speed and thus relatively inexpensive. A polarization tracking system has been shown to track polarization for up to 1 THz of optical bandwidth [52], a task that digital polarization compensation will be hard pressed to achieve at similar cost. We can say that polarization tracking will be a viable alternative to digital compensation of polarization drift if the cost of polarization tracking modules falls below the cost of using additional ADCs and additional digital processing for polarization diversity reception. Since the usage of polarization tracking modules is on the rise, it would be reasonable to expect that their prices would fall further with wider adoption in next generation networks.

Fig. 3.9 depicts the polarization tracking loop employed in my unified transmission experiment. The light with time-varying polarization is input to the POS-203 polarization stabilizer. The POS-203 output is divided into 2 paths – one path is to the Rx and the other path is to the polarization stabilizer feedback loop. A polarization analyzer (PA) followed by a photodiode (PD) provides a polarization dependent electrical signal. It is important to note that the carrier that is present in the polarization orthogonal to the OFDM signal in my pol-muxed composite signal produces a DC offset at the PD output. It is necessary to eliminate this DC offset so that only the time-varying components of the electrical feedback signal (which represent the OFDM signal) are used to determine the feedback signal to the POS-203. A DC block is used for this purpose. An ADL-5903 detector circuit is employed in the feedback loop to produce a DC voltage that is proportional to the RF input power to the ADL-5903 (The ADL-5903 does have an internal DC block, hence a discrete DC block as explained above and as shown in Fig. 3.9 is unnecessary in this case. Nevertheless, in case another method is used to generate the feedback signal, the DC block is critical to allow the POS-203 tracking algorithm to work correctly with this pol-muxed composite signal). This DC voltage is then fed to the electrical feedback input of the POS-203. The POS-203 is configured to tune the polarization of light passing through it so as to *minimize* the electrical feedback signal to the POS-203. Initially, when the light output from the POS-203 is not 'locked' to the desired polarization, as shown in Fig. 3.9 (a), light from both the carrier and the OFDM signal polarizations passes through the

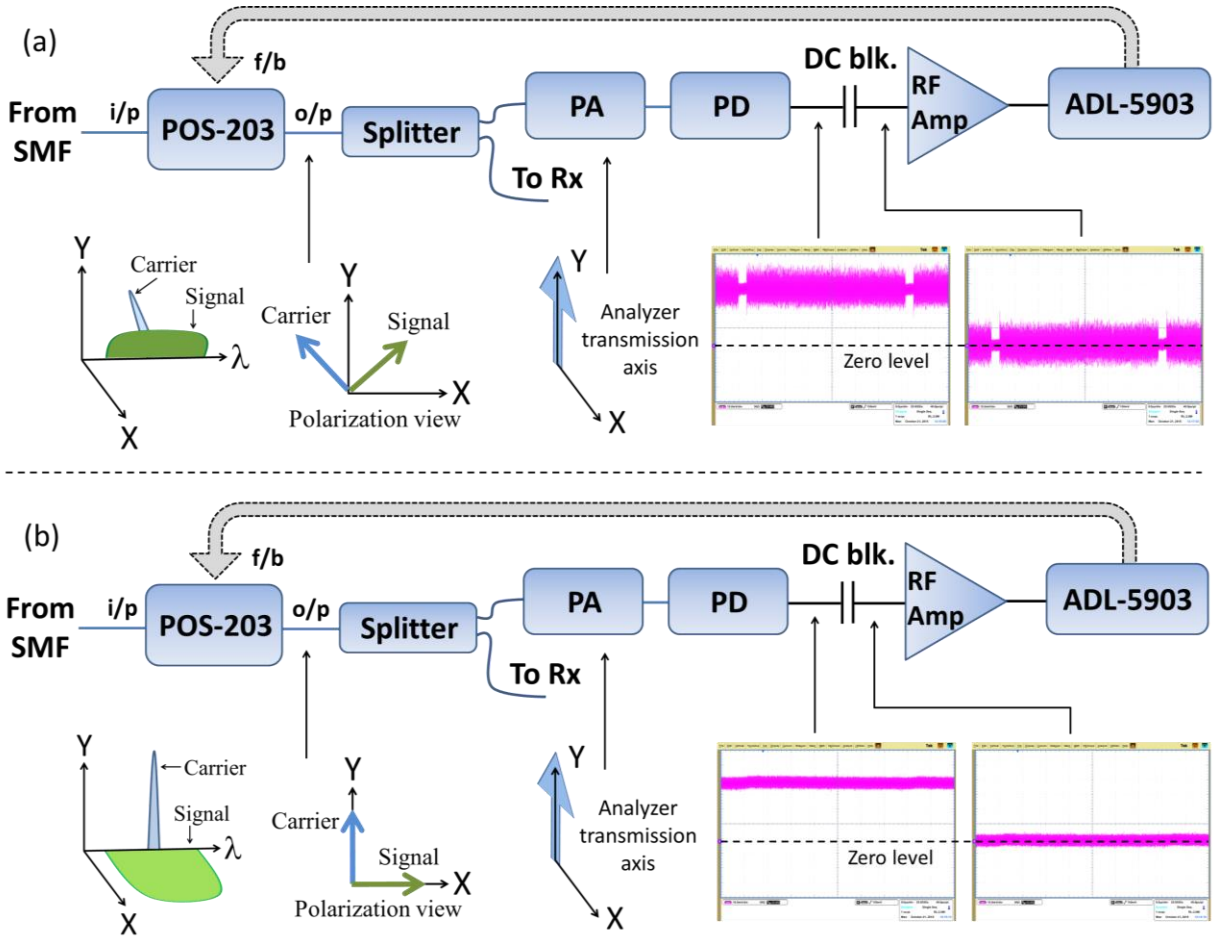

Fig. 3.9 The polarization tracking system with (a) the polarization not locked; (b) the polarization locked to the desired polarization. The waveforms before and after the DC block are also shown in insets for each case.

PA. Hence, a non-zero electrical RF signal is seen after the DC block. This causes the ADL-5903 to produce a larger DC feedback voltage to the POS-203 and the POS-203 iteratively adjusts the polarization of the light passing through it to minimize the DC feedback voltage. Once the light is 'locked' to the desired polarization as shown in Fig. 3.9 (b), the light from the OFDM signal polarization no longer passes through the PA and hence a zero valued electrical RF signal is seen after the DC block. This causes the ADL-5903 to produce its minimum DC feedback voltage to the POS-203. The POS-203 continuously adjusts the polarization of the incoming light so as to stay at this 'minima' point.

3.4.3 The results for the unified transmission experiment

Fig. 3.10 shows the bit error rate (BER) performance of the DPO based direct receiver and the FPGA based coherent receiver and serves as the proof of concept that the unified Tx can communicate simultaneously with both direct and coherent receiver types with good reception performance. BER readings were taken at least until the FEC BER limit of $8x10^{-3}$. The X axis in Fig. 3.10 (a)-(b) represents the optical power of the signal (power of all loaded OFDM subcarriers) at each of the points A and B indicated in Fig. 3.7. It is important to note that this power cannot be directly compared with the power indicated on the X axis in Fig. 3.12 as the power in Fig. 3.12 represents the signal power after interference with the carrier (for pol-mux SSB-OFDM) while the power in Fig. 3.10 represents the signal power

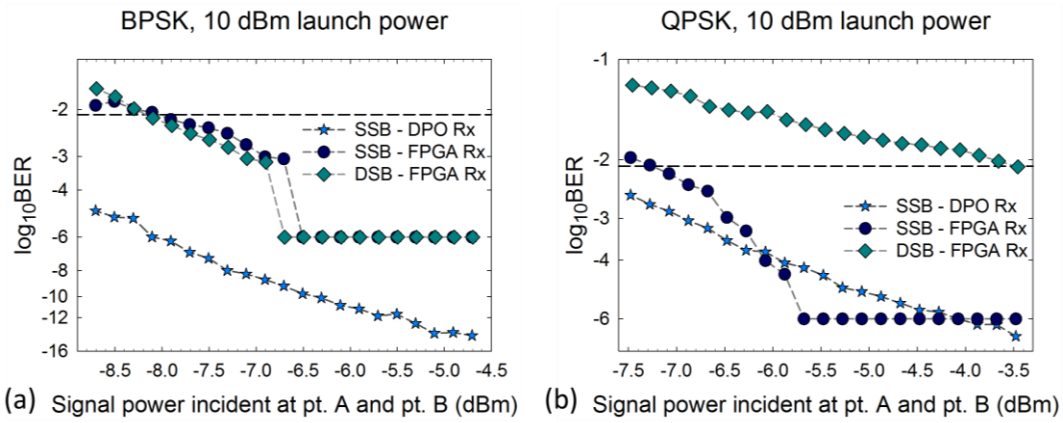

Fig. 3.10 The BER performance of the DPO based direct receiver (SSB-OFDM configuration only) and the FPGA based coherent receiver (both SSB and DSB OFDM configurations) at 10 dBm launch power for (a) BPSK and (b) QPSK subcarrier modulation formats. The dashed horizontal line in both figures represents the forward error correction (FEC) BER limit of $8x10^{-3}$. Please note that the signal power refers to points A and B in order to perform a meaningful comparison. Signal power at the receiver inputs is ~8 dB lower (please see Fig. 3.12).

before interference with the carrier. Each power definition in Fig. 3.10 and Fig. 3.12 was chosen to best represent and compare the OFDM formats studied in each of these experiments. As the FPGA system has limited hardware resources, I implemented a simple bit counting method to calculate the BER of the text data for the FPGA system. This method enables a BER as low as $1x10^{-6}$ to be measured and is an optimum trade-off between the lowest BER that can be measured and the time it takes to compute a new BER value. On the DPO based direct receiver, I implemented an error vector magnitude (EVM) based BER calculation method [53] for the text data; this method is capable of measuring BER levels even

lower than those measured by the FPGA based receiver. The EVM based BER method also enables quicker estimation of BER compared to the bit counting method given the fact that the DPO based direct receiver samples the received OFDM waveform about once every second. Accordingly, it takes about a ten times longer period to estimate BER using bit counting on the DPO as compared to the FPGA measurements.

The differences between the direct and coherent receiver implementation – both in optical domain (photodiode responsivity and bandwidth) and electrical domain (effective ADC resolution, fixed/floating point arithmetic), account for the difference in the BER measured by the direct and coherent receivers for the same pol-mux SSB-OFDM configuration (Fig. 3.10 (a) and (b)). The pol-mux DSB-OFDM configuration can be received by the FPGA based coherent receiver alone. The optical launch power into the fiber is kept constant at 10 dBm for both pol-mux SSB-OFDM and pol-mux DSB-OFDM configurations. In Fig. 3.10 (a), I attribute the step change in the BER for the FPGA Rx in both SSB and DSB OFDM configurations to the OFDM frame synchronization method I have implemented in the FPGA that begins to lose accuracy below a certain waveform amplitude threshold. In Fig. 3.10 (b), the pol-mux DSB-OFDM configuration has a higher BER as compared to the pol-mux SSB-OFDM configuration since the constant optical power has to be shared among a larger number of loaded subcarriers in the DSB-OFDM configuration, thus lowering the optical signal to noise ratio for each subcarrier. This effect is evidently higher for QPSK modulation.

3.4.4 FPGA utilization

OFDM_Tx_design Project Status (12/16/2014 - 00:58:57)			
Project File:	OFDM_Tx_design.xise	**Target Device:**	xc5vsx95t-2ff1136

Device Utilization Summary			
Slice Logic Utilization	**Used**	**Available**	**Utilization**
Number of Slice Registers	21,691	58,880	36%
Number of Slice LUTs	18,461	58,880	31%
Number of occupied Slices	8,014	14,720	54%
Number of bonded IOBs	274	640	42%
Number of BlockRAM/FIFO	127	244	52%
Total Memory used (KB)	3,960	8,784	45%
Number of BUFG/BUFGCTRLs	9	32	28%
Number of IDELAYCTRLs	3	22	13%
Number of DSP48Es	336	640	52%
Number of PLL_ADVs	1	6	16%
Number of TEMACs	1	2	50%

Table 3.2 The FPGA utilization for the coherent detection OFDM Tx (FPGA 'A'). This is the main data processing FPGA at the transmitter, the 'I' data output is sent to DAC1 and the 'Q' data output is sent to DAC2 via the Tx2 FPGA (FPGA 'D') as DAC2 has no direct connection to the Tx FPGA.

OFDM_Tx_design Project Status (07/10/2014 - 18:45:19)			
Project File:	OFDM_Tx_design.xise	**Target Device:**	xc5vsx95t-2ff1136

Device Utilization Summary			
Slice Logic Utilization	**Used**	**Available**	**Utilization**
Number of Slice Registers	701	58,880	1%
Number of Slice LUTs	559	58,880	1%
Number of occupied Slices	320	14,720	2%
Number of bonded IOBs	264	640	41%
Number of BlockRAM/FIFO	4	244	1%
Total Memory used (KB)	72	8,784	1%
Number of BUFG/BUFGCTRLs	9	32	28%
Number of IDELAYCTRLs	3	22	13%
Number of PLL_ADVs	1	6	16%

Table 3.3 The FPGA utilization for the coherent detection OFDM Tx2 (FPGA 'D'). Since this FPGA performs no signal processing and merely forwards the 'Q' data received from the Tx FPGA (where the signal processing occurs) to the DAC2, the FPGA utilization is low.

OFDM_Rx_design Project Status (12/22/2014 - 15:36:33)			
Project File:	OFDM_Rx_design.xise	**Target Device:**	xc5vsx95t-2ff1136

Slice Logic Utilization	Used	Available	Utilization
Number of Slice Registers	20,705	58,880	35%
Number of Slice LUTs	17,798	58,880	30%
Number of occupied Slices	7,767	14,720	52%
Number of bonded IOBs	267	640	41%
Number of BlockRAM/FIFO	104	244	42%
Total Memory used (KB)	3,240	8,784	36%
Number of BUFG/BUFGCTRLs	14	32	43%
Number of IDELAYCTRLs	5	22	22%
Number of DSP48Es	368	640	57%
Number of PLL_ADVs	2	6	33%
Number of TEMACs	1	2	50%

Table 3.4 The FPGA utilization for the coherent detection OFDM Rx (FPGA 'B'). This is the main data processing FPGA at the receiver, the 'I' data input is received from ADC1 and the 'Q' data input is received from ADC2 via the Rx2 FPGA (FPGA 'C') as ADC2 has no direct connection to the Rx FPGA.

OFDM_Rx_design Project Status (12/05/2014 - 18:15:36)			
Project File:	OFDM_Rx_design.xise	**Target Device:**	xc5vsx95t-2ff1136

Device Utilization Summary			
Slice Logic Utilization	**Used**	**Available**	**Utilization**
Number of Slice Registers	968	58,880	1%
Number of Slice LUTs	1,117	58,880	1%
Number of occupied Slices	647	14,720	4%
Number of bonded IOBs	268	640	41%
Number of BlockRAM/FIFO	10	244	4%
Total Memory used (KB)	342	8,784	3%
Number of BUFG/BUFGCTRLs	13	32	40%
Number of IDELAYCTRLs	3	22	13%
Number of DSP48Es	32	640	5%
Number of PLL_ADVs	2	6	33%

Table 3.5 The FPGA utilization for the coherent detection OFDM Rx2 (FPGA 'C'). Since this FPGA performs no significant signal processing other than OFDM frame synchronization for the 'Q' data input and forwards the 'Q' data received from the ADC2 to the Rx FPGA (where the signal processing occurs), the FPGA utilization is low.

3.4.5 Energy efficiency calculations

Tables 3.6 – 3.11 show the power consumption estimates for sub-systems of the OFDM Tx and Rx. The FPGA power consumption estimates in Tables 3.6, 3.7, 3.9 and 3.10 are derived from the Xilinx XPower Analyzer tool that is part of the Xilinx ISE 13.4 System Edition package. The power consumption estimates for components in Table 3.8 and Table 3.11 (excluding the FPGA) are derived from the respective manufacturer datasheets.

FPGA resource	**Power consumption (W)**
Clocks	0.850
Logic	0.115
Signals	0.143
BRAMs	1.493
DSPs	0.061
PLLs	0.132
TEMACs	0.019
IOs	4.913
Leakage	1.721
FPGA Total	**9.449**

Table 3.6 OFDM Tx FPGA (FPGA 'A') power consumption

FPGA resource	**Power consumption (W)**
Clocks	0.100
Logic	0.001
Signals	0.009
BRAMs	0.006
DSPs	0
PLLs	0.133
TEMACs	0
IOs	2.935
Leakage	1.635
FPGA Total	**4.819**

Table 3.7 OFDM Tx2 FPGA (FPGA 'D') power consumption

Tx component	Power consumption (W)
Tx FPGA Total	9.449
Tx2 FPGA Total	4.819
2 DACs	1.15x2 = 2.3
ITLA	3.5
2 Modulator drivers	4.9x2 = 9.8
EDFA	5
Transmitter Total	**34.868**

Table 3.8 OFDM Tx power consumption

Energy/bit = Transmitter total power / maximum bit-rate for coherent OFDM

= 34.868W / 2134.1Mbps

= 16.338 nJ/bit

Bits/Joule = 61.205 Mb/J

FPGA resource	Power consumption (W)
Clocks	0.868
Logic	0.108
Signals	0.144
BRAMs	1.220
DSPs	0.048
PLLs	0.219
TEMACs	0.019
IOs	4.283
Leakage	1.695
FPGA Total	**8.605**

Table 3.9 OFDM Rx FPGA (FPGA ‘B’) power consumption

FPGA resource	Power consumption (W)
Clocks	0.171
Logic	0.002
Signals	0.011
BRAMs	0.068
DSPs	0.001
PLLs	0.219
TEMACs	0
IOs	2.486
Leakage	1.628
FPGA Total	**4.586**

Table 3.10 OFDM Rx2 FPGA (FPGA 'C') power consumption

Rx component	Power consumption (W)
Rx FPGA Total	8.605
Rx2 FPGA Total	4.586
2 ADCs	1.8x2 = 3.6
Integrated coherent receiver	0.7
Polarization stabilizer	7.8
Receiver Total	**25.291**

Table 3.11 OFDM Rx power consumption

Energy/bit = Receiver total power / maximum bit-rate for coherent OFDM

= 25.291W / 2134.1Mbps

= 11.8509 nJ/bit

Bits/Joule = 84.38 Mb/J

Total coherent OFDM Tx and Rx power consumption = 34.868 + 25.291 = 60.159 W

Total coherent OFDM Tx and Rx energy efficiency = 16.338 + 11.8509 = 28.1889 nJ/bit

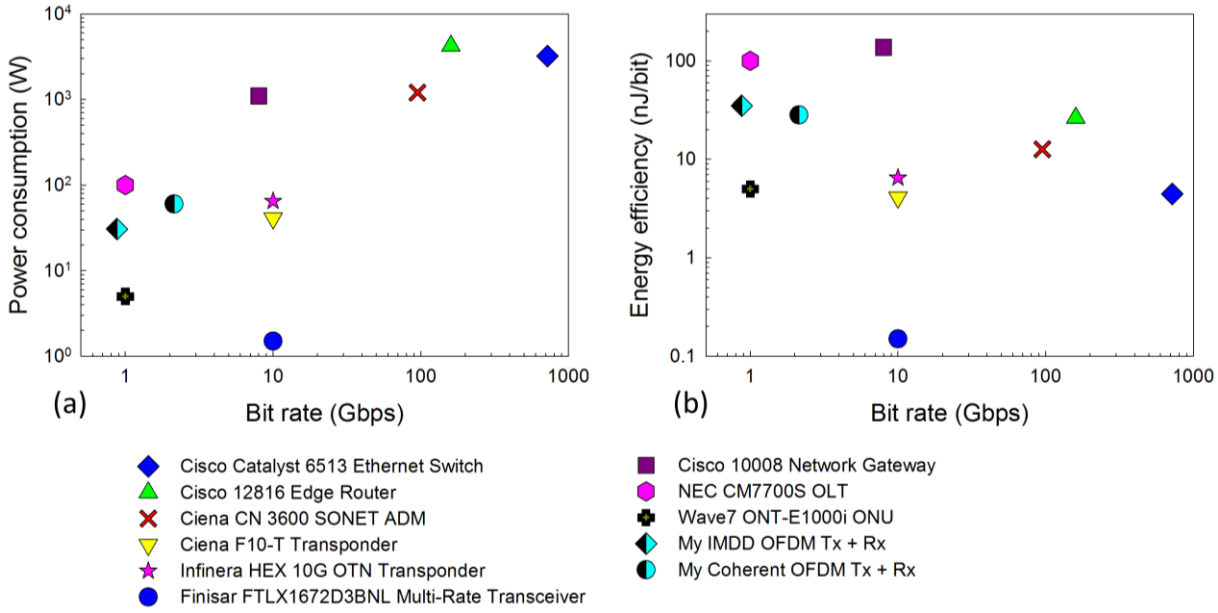

Fig. 3.11 (a) The power consumption of commercially available networking equipment and my OFDM systems (IMDD and coherent); (b) The energy efficiency of commercially available networking equipment and my OFDM systems (IMDD and coherent), a lower energy efficiency number (in nJ/bit) is better.

The combination of the OFDM Tx and Rx can be considered as a single transceiver. This makes it easier to compare the power consumption and energy efficiency of my coherent OFDM system with commercially available networking equipment. Fig. 3.11 shows this comparison. Here, we can see that while my coherent OFDM system has about twice the power consumption as compared to my IMDD OFDM system, the coherent OFDM system is 19% more energy efficient compared to the IMDD OFDM system.

3.5 Comparison of pol-mux OFDM with IMDD-OFDM

3.5.1 Experiment setup and results

In Sec. 3.2, I mentioned that the pol-mux scheme eliminates the carrier bias and reduces the impact of fiber nonlinearities compared to conventional IMDD-OFDM transmission. In this section, I quantify the benefit of the pol-mux scheme over the IMDD-OFDM scheme. I compare pol-mux SSB-OFDM with IMDD-OFDM as pol-mux DSB-OFDM cannot be directly detected and does not provide identical bit-rates to IMDD-OFDM. Using the same photodiode and DPO for direct detection, we can compare pol-mux SSB-OFDM with IMDD-OFDM on an equal footing. I set the OFDM Tx to produce either a pol-mux SSB signal or an IMDD signal with identical bit rate that was launched into the fiber at identical total optical power (carrier power + power of all loaded OFDM subcarriers). The pol-mux SSB signal-to-total power ratio [power of all loaded OFDM subcarriers/(carrier power + power of all loaded OFDM subcarriers)] was kept identical to its IMDD equivalent. The modulation format on all OFDM subcarriers carrying text data was either BPSK or QPSK, while video data was not transmitted.

The BER was evaluated using the EVM based method [53]. The X axis in Fig. 3.12 (a)-(f) indicates the optical power of the signal alone without considering the carrier offset/bias in the time domain waveform. This enables a meaningful comparison between IMDD and SSB OFDM waveforms which have different carrier offsets/biases at the receiver photodiode. This difference is a consequence of setting the analyzer angle to the optimum value for the SSB-OFDM waveform (as explained in Sec. 3.2) which gives the SSB-OFDM waveform a larger carrier offset/bias. At launch power of 10 dBm, IMDD-OFDM has equivalent BER values as compared to pol-mux SSB-OFDM [Fig. 3.12 (a) and 3.12 (b)]. At launch power of 13 dBm, IMDD-OFDM has equivalent or slightly higher BER values as compared to pol-mux SSB-OFDM [Fig. 3.12 (c) and 3.12 (d)]. At higher launch power (17 dBm), pol-mux SSB-OFDM has lower BER and higher receiver sensitivity [Fig. 3.12 (e) and 3.12 (f)], which demonstrates the resilience of the pol-mux transmission scheme to impairments due to nonlinear effects in fiber. The simulation curves match well with the experiment data.

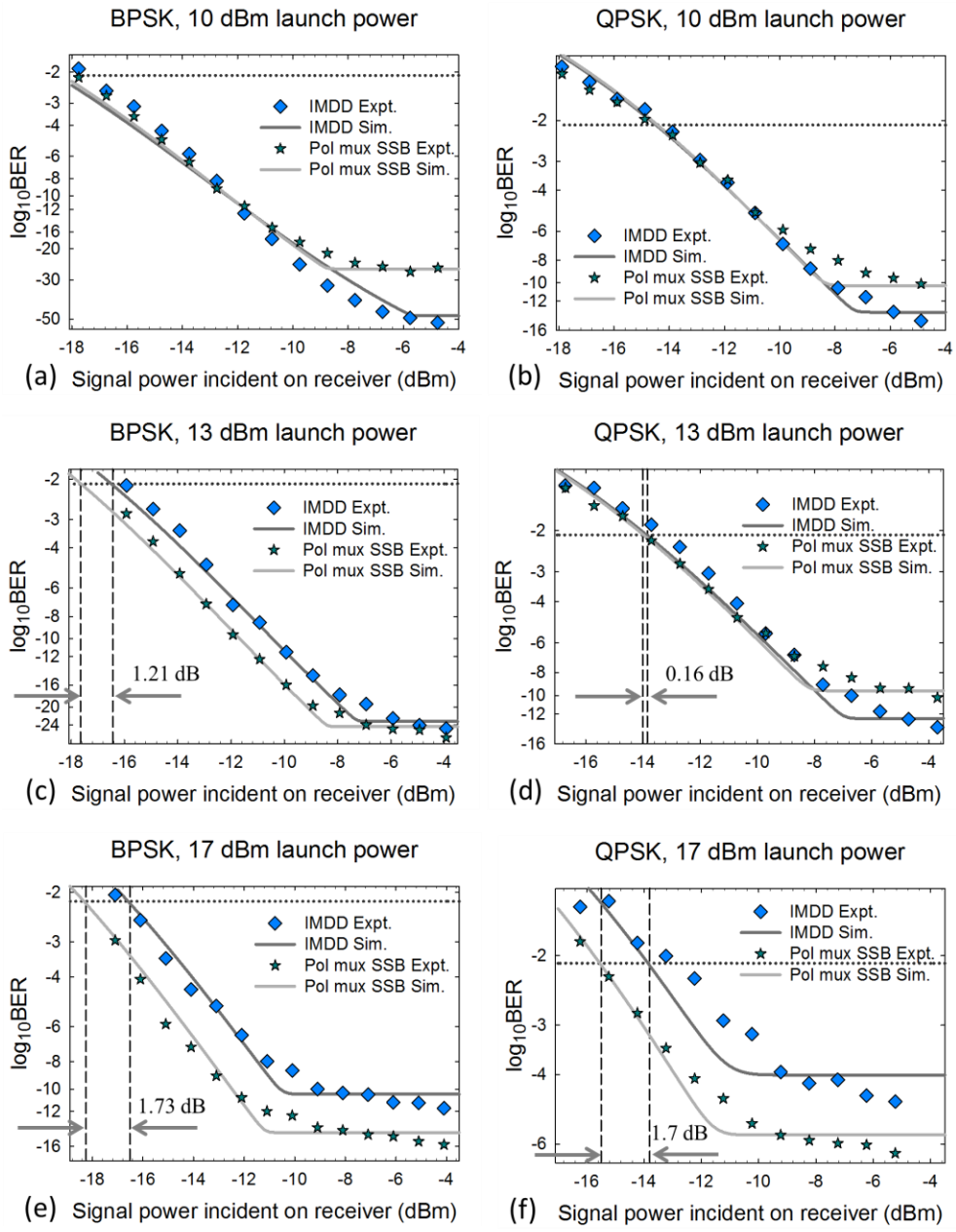

Fig. 3.12 BER performance of the pol-mux SSB-OFDM scheme vs. the IMDD-OFDM scheme for BPSK and QPSK modulation formats at 10 dBm [(a), (b)], 13 dBm [(c), (d)] and 17 dBm [(e), (f)] launch powers into the fiber. Dashed vertical lines indicate the receiver sensitivity at $8x10^{-3}$ BER (FEC limit). For the legends: Expt. – experiment data, Sim. – simulation data.

3.5.2 Discussion on the simulation method and the noise sources considered

For the simulation, I devised a split approach. The impact of self-phase modulation (SPM) (the primary non-linear impairment in this setup) and inter-modulation distortion (IMD) noise was determined by simulating the transmission of the OFDM signal over fiber using the PHOTOSS 4.50 simulation tool. The constellation diagram obtained from this simulation was evaluated and the BER was determined using the EVM method [53] as described below.

$$\sigma_{err}^2 = \frac{1}{N}\sum_{i=1}^{N}\left[\left(S_{rcvd,\ i}^{real} - S_{ideal,\ i}^{real}\right)^2 + \left(S_{rcvd,\ i}^{imag} - S_{ideal,\ i}^{imag}\right)^2\right] \tag{3.2}$$

$$EVM_a = k\,\frac{\sigma_{err}}{\left|S_{ideal,\ max}\right|}, \qquad k = 1\ for\ B/Q/8-PSK \tag{3.3}$$

$$BER_{SPM+IMD} = \frac{1-\frac{1}{\sqrt{M}}}{\frac{1}{2}log_2 M}\ erfc\left(\sqrt{\frac{3/2}{(M-1)EVM_a^2}}\right) \tag{3.4}$$

As shown in Eqn. 3.2, the EVM method relies on first calculating the error term σ_{err}^2 by comparing the received complex constellation symbols ($S_{rcvd,\ i}$, superscripted with '*real*' and '*imag*' to denote the real and imaginary components respectively) with the ideal complex constellation symbols ($S_{ideal,\ i}$, superscripted with '*real*' and '*imag*' to denote the real and imaginary components respectively), N denotes the total number of constellation symbols considered. Using Eqn. 3.3, the EVM_a can be calculated using σ_{err} determined from Eqn. 3.2 and the maximum magnitude of the ideal constellation symbol $S_{ideal,\ max}$. Eqn. 3.4 enables the $BER_{SPM+IMD}$ (denoting the impact of SPM and IMD noise) to be computed from the EVM_a term, with M denoting the total number of constellation points for a given modulation format and *erfc()* denoting the complementary error function.

The DAC and ADC quantization noise, thermal noise and shot noise were determined using analytical expressions as explained below. The root mean squared (RMS) ADC quantization noise $N_{ADC\ quant,\ rms}$ can be determined from the quantization step size q_{ADC} as shown in Eqn. 3.5 [54]. The signal to noise ratio for the ADC quantization noise term $SNR_{ADC\ quant}$ can then be determined with the knowledge of the RMS value of the signal being sampled by the ADC $S_{ADC\ quant,\ rms}$ as shown in Eqn. 3.6. In a similar manner, the impact of the DAC quantization noise can be determined from Eqn. 3.7 and Eqn. 3.8.

$$N_{ADC\ quant,\ rms} = \frac{q_{ADC}}{\sqrt{12}} \tag{3.5}$$

$$SNR_{ADC\ quant} = \frac{S_{ADC\ quant,\ rms}}{N_{ADC\ quant,\ rms}} \tag{3.6}$$

$$N_{DAC\ quant,\ rms} = \frac{q_{DAC}}{\sqrt{12}} \tag{3.7}$$

$$SNR_{DAC\ quant} = \frac{S_{DAC\ quant,\ rms}}{N_{DAC\ quant,\ rms}} \tag{3.8}$$

The RMS shot noise term $N_{shot,\ rms}$ is determined using Eqn. 3.9 [26], where q is the charge on an electron, P_{inc} is the optical power incident on the photodiode, R is the responsivity of the photodiode (0.65 A/W as per the datasheet) and Δf is the bandwidth over which the noise is considered, which is 10 GHz in this case. The RMS thermal noise term $N_{therm,\ rms}$ is determined using Eqn. 3.10 [26], where k_B is the Boltzmann's constant, T is the temperature of the photodiode in K and R_L is the load resistance, which is 50 Ω in this case. The cumulative SNR due to shot and thermal noise $SNR_{shot+therm}$ is evaluated using Eqn. 3.11.

$$N_{shot,\ rms} = \sqrt{2\ q\ P_{inc}\ R\ \Delta f} \tag{3.9}$$

$$N_{therm,\ rms} = \sqrt{\frac{4\ k_B\ T\ \Delta f}{R_L}} \tag{3.10}$$

$$SNR_{shot+therm} = \frac{P_{inc}\ R}{\sqrt{N_{shot,\ rms}^2 + N_{therm,\ rms}^2}} \tag{3.11}$$

The cumulative SNR due to DAC and ADC quantization noise, thermal noise and shot noise is determined using Eqn. 3.12.

$$SNR_{DAC\ \&\ ADC\ quant+shot+therm} = \frac{1}{\frac{1}{SNR_{DAC\ quant}} + \frac{1}{SNR_{ADC\ quant}} + \frac{1}{SNR_{shot+therm}}} \tag{3.12}$$

The BER is then determined using either Eqn. 3.13 or Eqn. 3.14 depending on the modulation format used [55].

$$For\ BPSK,\quad BER_{DAC\ \&\ ADC\ quant+shot+therm} = Q\left(\sqrt{2\ SNR_{DAC\ \&\ ADC\ quant+shot+therm}}\right) \tag{3.13}$$

$$For\ QPSK,\quad BER_{DAC\ \&\ ADC\ quant+shot+therm} = Q\left(\sqrt{2\ SNR_{DAC\ \&\ ADC\ quant+shot+therm}}\right)\cdot \left(1-\frac{1}{2}Q\left(\sqrt{2\ SNR_{DAC\ \&\ ADC\ quant+shot+therm}}\right)\right) \tag{3.14}$$

$$where\ Q(x) = \frac{1}{2}\ erfc\left(\frac{x}{\sqrt{2}}\right) \tag{3.15}$$

The BER resulting from the simulation ($BER_{SPM+IMD}$) is added to the BER obtained from the analytical expressions ($BER_{DAC\ \&\ ADC\ quant+shot+therm}$) to give the BER from all noise terms as shown in Eqn. 3.16.

$$BER_{All\ noise\ terms} = BER_{DAC\ \&\ ADC\ quant+shot+therm} + BER_{SPM+IMD} \tag{3.16}$$

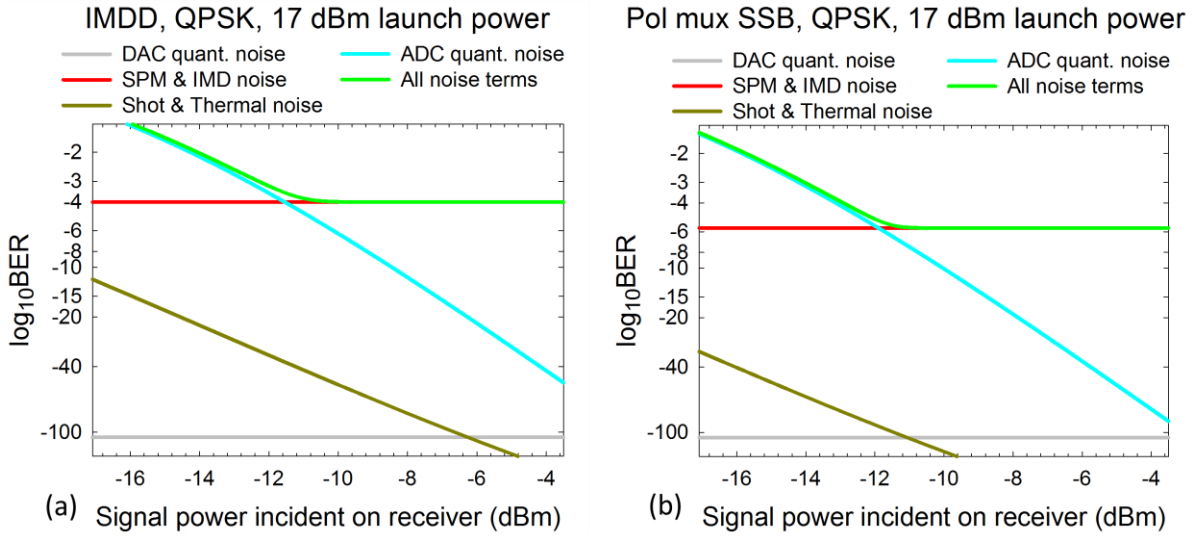

Fig. 3.13 The BER performance of the (a) IMDD and (b) pol mux schemes with individual noise terms.

Fig. 3.13 shows the impact of the individual noise terms on the BER for IMDD OFDM (Fig. 3.13 (a)) and pol mux SSB OFDM (Fig. 3.13 (b)). In both cases, it can be seen that SPM and

IMD noise are the dominant contributors to the total noise at higher values of incident signal power on the receiver while ADC quantization noise is the dominant noise source at lower values of incident signal power on the receiver.

3.5.3 Discussion on the role of the symbol rate on the strength of the nonlinear impairment in fiber

In the experiment, I used a 2 GSa/s OFDM symbol transmission rate as this was the maximum achievable DAC sampling rate (1 sample = 1 OFDM symbol at the FPGA Tx) for the real-time FPGA Tx. This relatively low symbol rate results in the benefit of the pol-mux scheme over the IMDD-OFDM scheme to be visible at relatively higher launch powers (13 dBm and 17 dBm). Let us consider the frequency shift introduced due to self-phase modulation (SPM), which is given as [26],

$$\delta\nu = \frac{-1}{\lambda}\frac{L_{eff}}{A_{eff}} n_2 \frac{dP}{dt} \tag{3.17}$$

where $\delta\nu$ is the frequency shift of the optical carrier, λ is the wavelength of the carrier, L_{eff} and A_{eff} are the effective length and effective cross-sectional area of the fiber respectively that characterize the strength of the nonlinear effects, n_2 is the Kerr coefficient, P is the instantaneous optical power and dP/dt is the

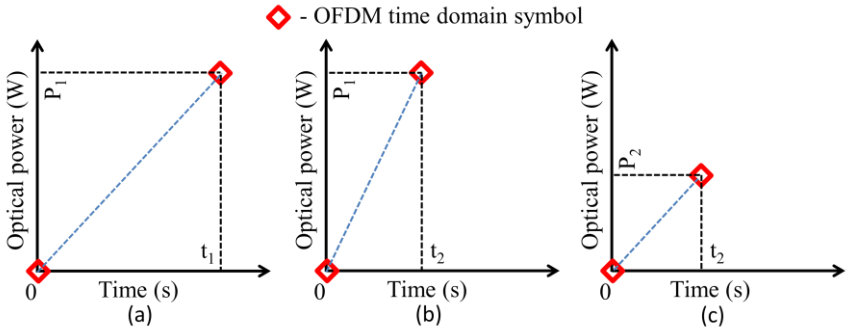

Fig. 3.14 Three time domain scenarios with a time rate of change of optical power of (a) P_1/t_1, (b) P_1/t_2, and (c) P_2/t_2. This figure illustrates the role of the OFDM symbol rate in determining the strength of the nonlinear effects in fiber.

instantaneous time rate of change of optical power. All parameters in this equation are constant for a defined system except dP/dt which varies according to the OFDM time domain waveform. Fig. 3.14 (a) depicts a transition from one OFDM time domain symbol to the next with $dP/dt = P_1/t_1$. Now if the OFDM symbol rate is doubled as shown in Fig. 3.14 (b), such that $t_2 = t_1/2$, while keeping the same

change in power i.e. P_1, $dP/dt = P_1/t_2 = P_1/(t_1/2) = 2P_1/t_1$. The time rate of the power change, and hence the frequency shift in Fig. 3.14 (b) is twice that of Fig. 3.14 (a). Thus, keeping the change in power constant while increasing the symbol rate results in higher frequency shift due to SPM. In order to maintain the same amount of frequency shift while increasing the symbol rate, the change in power must be decreased by a proportional amount. Per Fig. 3.14 (c), if we have that $P_2 = P_1/2$, $dP/dt = P_2/t_2 = (P_1/2)/(t_1/2) = P_1/t_1$, which means that nonlinear effects will be observed for OFDM signals at higher symbol rate at lower launch powers. The above analysis can be summarized by the equation:

$$P_A = P_B - 10 \cdot log_{10}\left(\frac{S_A}{S_B}\right) \tag{3.18}$$

where P_A and P_B are the launch powers in dBm for OFDM signals with symbol rates of S_A and S_B respectively. Based on Eqn. 3.18, we can conclude that the impact of nonlinear effects, and therefore the benefit of the pol-mux scheme over the IMDD-OFDM scheme observed for the 2 GSa/s (i.e. 2 GSymbols/s) OFDM waveform launched at 17 dBm power in our experiment, will be equivalent to the impact/benefit with respect to OFDM symbol rates of 12 GSymbols/s and 24 GSymbols/s launched at 9.2 dBm and 6.2 dBm, respectively. These power levels are lower than the maximum launch power limits defined in various passive optical network (PON) standards. Therefore, we can conclude that the benefit of the pol-mux scheme as compared to the IMDD-OFDM scheme can be observed even at standard launch power levels.

3.6 An enhanced detection scheme for pol-mux SSB-OFDM: Dual analyzer balanced detection

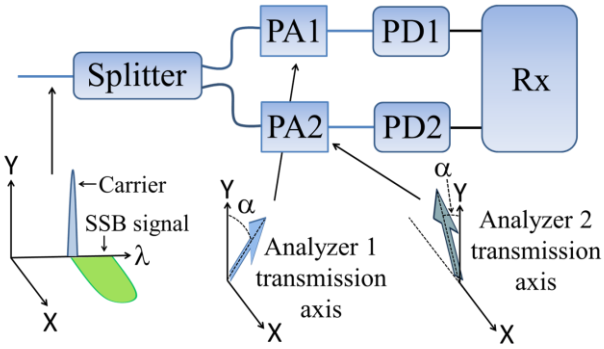

Fig. 3.15 The dual analyzer balanced detection setup.

The reception performance of the pol-mux SSB-OFDM scheme can be further enhanced with a dual analyzer balanced detection (DABD) scheme as compared to the single analyzer direct detection scheme that I introduced in Sec. 3.2. Namely, in the direct detection scheme with pol-mux SSB-OFDM signals discussed above, a single photodiode is used and the analyzer transmission axis is set at an optimal angle α_{opt} to minimize the signal-signal interference term. However, by using a second pair of analyzer and photodiode with its analyzer transmission axis set to an identical angle, but with an opposite rotation as shown in Fig. 3.15, the two receivers operate like a regular balanced photodiode pair. Based on Eqn. 3.1 and by considering a negative analyzer angle, the output from the second arm now takes the form

$$\begin{aligned}
&\left[E_{carr} \cdot e^{j\cdot(\omega_{carr}\cdot t+\delta)} \cdot cos\,(-\alpha) + E_{sig} \cdot e^{j\cdot(\omega_{sig}\cdot t+\delta)} \cdot sin\,(-\alpha)\right]^2 \\
&\quad = \left[E_{carr} \cdot e^{j\cdot(\omega_{carr}\cdot t+\delta)} \cdot cos\,\alpha - E_{sig} \cdot e^{j\cdot(\omega_{sig}\cdot t+\delta)} \cdot sin\,\alpha\right]^2 \\
&\quad = E_{carr}^2 \cdot cos^2\alpha + E_{sig}^2 \cdot sin^2\alpha \\
&\qquad - 2 \cdot E_{sig} \cdot E_{carr} \cdot cos\left[\left(\omega_{carr} - \omega_{sig}\right) \cdot t + (\delta - \delta)\right] \cdot cos\,\alpha \cdot sin\,\alpha \\
&\quad = E_{carr}^2 \cdot cos^2\alpha + E_{sig}^2 \cdot sin^2\alpha \\
&\qquad - 2 \cdot E_{sig} \cdot E_{carr} \cdot cos\left[\left(\omega_{carr} - \omega_{sig}\right) \cdot t\right] \cdot cos\,\alpha \cdot sin\,\alpha
\end{aligned} \tag{3.19}$$

Any residual phase δ in the second arm is identical for both signal and carrier as they co-propagate in the same optical path and hence δ cancels out in the signal-carrier interference term. The negative analyzer angle in the second arm has the effect of giving the signal-carrier interference term a negative sign. Thus, the electrical outputs of the two arms given by Eqns. 3.1 and 3.19 when subtracted leave behind only the signal-carrier interference term. Using simulation, Fig. 3.16 (a) and Fig. 3.16 (b) show the

performance improvement of the dual analyzer balanced detection scheme over single analyzer detection. For 13 dBm launch power in Fig. 3.16 (a), a 2.95 dB sensitivity improvement is observed at $8x10^{-3}$ BER (the FEC limit), which can be attributed to the fact that the peak-to-peak voltage of the combined electrical output of the two arms is twice that of the voltage output of the single analyzer detection case. The sensitivity improvement drops to 2.14 dB for 17 dBm launch power in Fig. 3.16 (b) as the peak-to-peak voltage of the combined electrical output of the two arms reaches the maximum allowable peak-to-peak voltage of the receiver ADC.

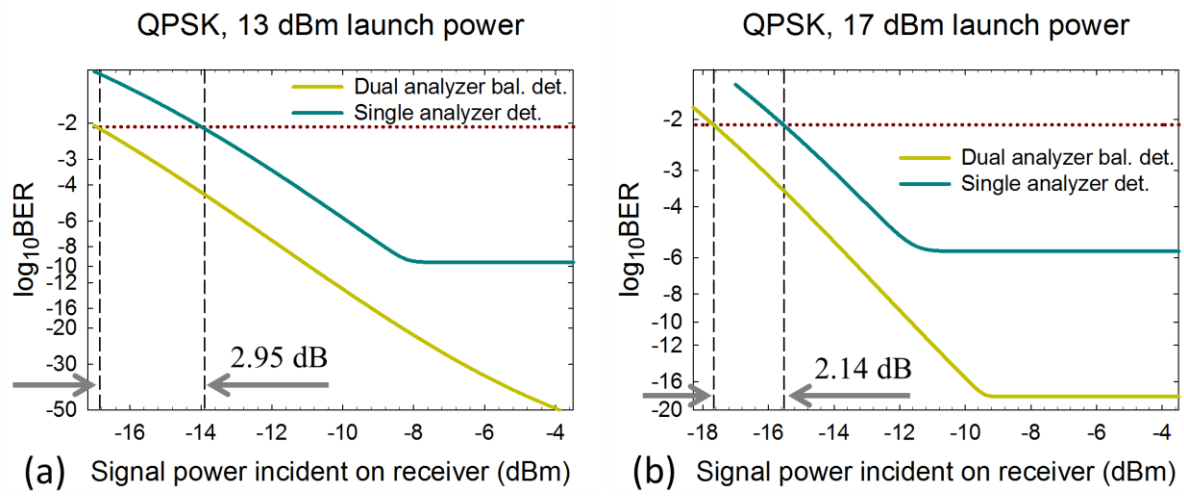

Fig. 3.16 The BER performance comparison between single analyzer detection and dual analyzer balanced detection for (a) 13 dBm and (b) 17 dBm launch powers, for pol-mux SSB-OFDM, QPSK subcarrier modulation, 2 GSa/s OFDM signal. The BER is evaluated using the EVM method [53].

In addition to being able to eliminate the signal-signal interference term, the DABD scheme is also resilient to the polarization drift occurring in the transmission fiber. In simulation, I varied the polarization state at the transmission fiber output by varying θ (the orientation angle of the polarization ellipse) and ϕ (the phase difference between the orthogonal decompositions of polarization) (see Fig. 3.17). The BER performance with the DABD scheme [Fig. 3.17 (b) and (d)] is superior when compared to single analyzer detection [Fig. 3.17 (a) and (c)]. Specifically, a larger area in Figs. 3.17 (b) and (d) has lower BER as compared to Figs. 3.17 (a) and (c), which allows the polarization stabilizer to have a wider range of target polarization states. Please note that there are extremely low values of BER (BER<$1x10^{-15}$) in Figs. 3.17 (b) and (d) obtained by applying the EVM based BER calculation method [53]. Obviously, these values have just a theoretical meaning and reflect error free transmission, but they are shown in Figs. 3.17 (b)

and (d) to illustrate the advantage of the DABD scheme and its flexibility with respect to θ and ϕ parameters. This translates to the ability of using a polarization stabilizer that is both slower and less

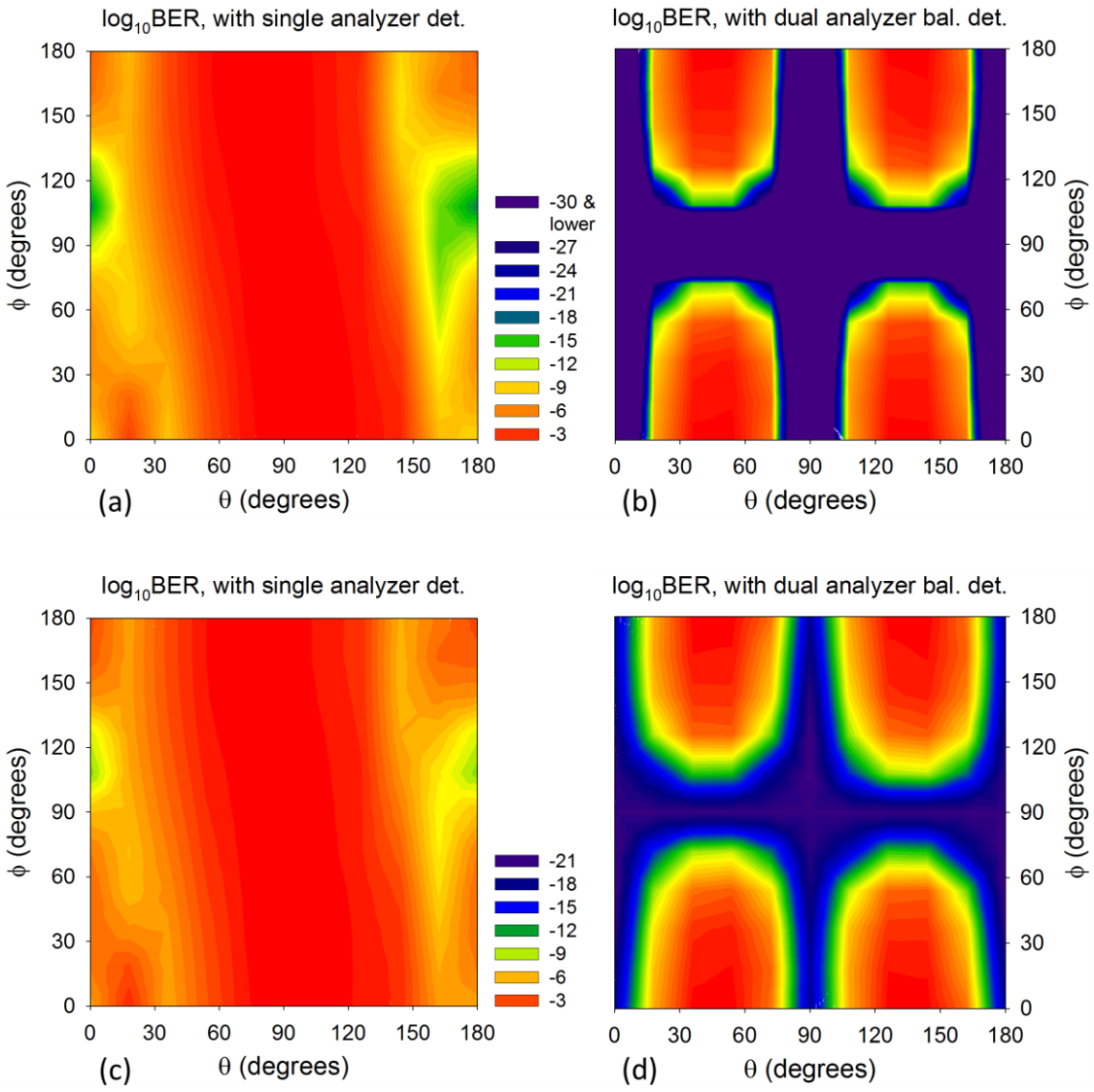

Fig. 3.17 The BER performance across various polarization states of the received light for pol-mux SSB-OFDM, QPSK subcarrier modulation, 2 GSa/s OFDM signal, -4 dBm signal power incident on receiver at θ = 0° and ϕ = 0°, α = 10 ° in (a) single analyzer detection, 13 dBm launch power; (b) dual analyzer balanced detection, 13 dBm launch power; (c) single analyzer detection, 17 dBm launch power; and (d) dual analyzer balanced detection, 17 dBm launch power. The BER is evaluated using the EVM method [53].

accurate than the one needed for the single analyzer detection case. I have thus demonstrated a direct detection scheme using two polarization analyzers and two photodiodes that provides sensitivity

improvement and allows for less accurate and lower cost polarization stabilizers to be used as compared to the single analyzer detection scheme I introduced and studied in the previous sections.

3.7 Conclusions

I have experimentally demonstrated a novel unified OFDM transmission scheme that can communicate simultaneously with both direct and coherent receiver types. By using self-coherent OFDM transmission and optical polarization tracking, a simplified FPGA coherent receiver architecture is enabled. I have experimentally verified the resilience of the pol-mux scheme to fiber nonlinearities and achieved receiver sensitivity improvement of up to 1.73 dB compared to the IMDD-OFDM scheme. I have also verified the effectiveness of the dual analyzer balanced detection scheme in providing better BER performance even with a minor drift in the polarization state of the received light. Due to the need for polarization tracking at the receiver, this transmission scheme can be an attractive alternative to digital compensation of polarization drift once polarization tracking modules suitable for integration in receivers become more affordable. I believe that a unified transmitter approach has the potential to provide better scalability and flexibility in optical network deployment by providing ready interchangeability between receiver types.

Chapter 4

OFDM pilot-tone assisted distributed control of optical network elements

4.1 Introduction

The configuration of optical filters on demand in a real-time environment [56] offers potential performance improvement for elastic optical networks since the passbands of these network elements can be configured in accordance with the changes in traffic spectrum [57]. The placement of the control plane in an elastic optical network is an important design consideration, broadly classified into two competing approaches – centralized and distributed. An SDN based centralized controller, which collects the traffic load from electrical networks and uses it to optimize the optical network performance has been demonstrated [31]. While a careful study of the network must be performed before deciding on controller placement [58], the distributed control approach has been shown to reduce latency in optical networks [59]. Pilot-tones have been used to convey optical performance monitoring information [60] and they can also be used to convey distributed control information. Since OFDM offers fine bandwidth granularity with multiple orthogonal subcarriers, the low frequency subcarriers can readily be used as pilot-tones with no requirement for additional modulators to modulate the optical data signal with the pilot-tones. In addition, the use of low speed and hence low cost photodiodes to receive the pilot-tones enables cost-effective distributed controllers to be built. In this chapter, I propose and experimentally demonstrate the use of a low frequency OFDM subcarrier as a pilot-tone for distributed control of an optical network element.

4.2 OFDM pilot-tone assisted distributed control

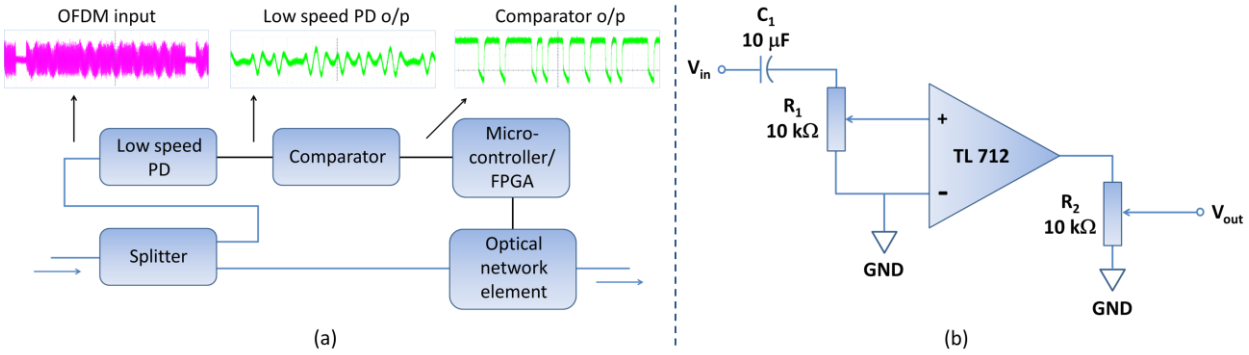

Fig. 4.1 (a) The main idea of using an OFDM pilot-tone for distributed control; (b) Circuit diagram of the comparator.

Fig. 4.1 (a) shows the main components of an OFDM pilot-tone based distributed control scheme. The incoming OFDM signal is split and a portion of the light is input to a low speed photodiode (PD). The PD output is connected to a comparator circuit that converts the multi-level PD output to a 2 level i.e. binary signal. The binary signal, which indicates the parameters of the OFDM signal, is input to a micro-controller or a field programmable gate array (FPGA) for processing. The remainder of the light from the splitter is input to the network element that is controlled by the micro-controller or FPGA. In this way, the network element can be configured in a distributed manner by the very signal that the network element handles.

In our OFDM pilot-tone assisted distributed control scheme, the lowest frequency OFDM subcarrier at 5.86 MHz is used as the pilot-tone and the main traffic is carried on other subcarriers. The amplitude of the pilot-tone subcarrier is set to be 16 dB higher than the subcarriers carrying traffic, in order to have sufficient power for proper pilot-tone detection. The pilot-tone carries a 16 bit binary code that conveys information about the OFDM signal composition (i.e. channel bandwidth and subcarrier modulation formats). The first eight bits are preamble bits (10101100), and these bits are needed to correctly synchronize the next 8 bits that carry the actual composition code. Each bit has a duration equal to the IFFT period (i.e. 171 ns for a 4096 point IFFT at 24 GSa/s). A part of the OFDM signal power is introduced into a low speed photodiode with a 10 MHz bandwidth and is therefore able to receive the pilot-tone, while filtering high frequency subcarriers. I used a Thorlabs PDA20CS photodiode with a 3 dB bandwidth of 10 MHz in the 0 dB gain setting. An analog comparator based on the TL712

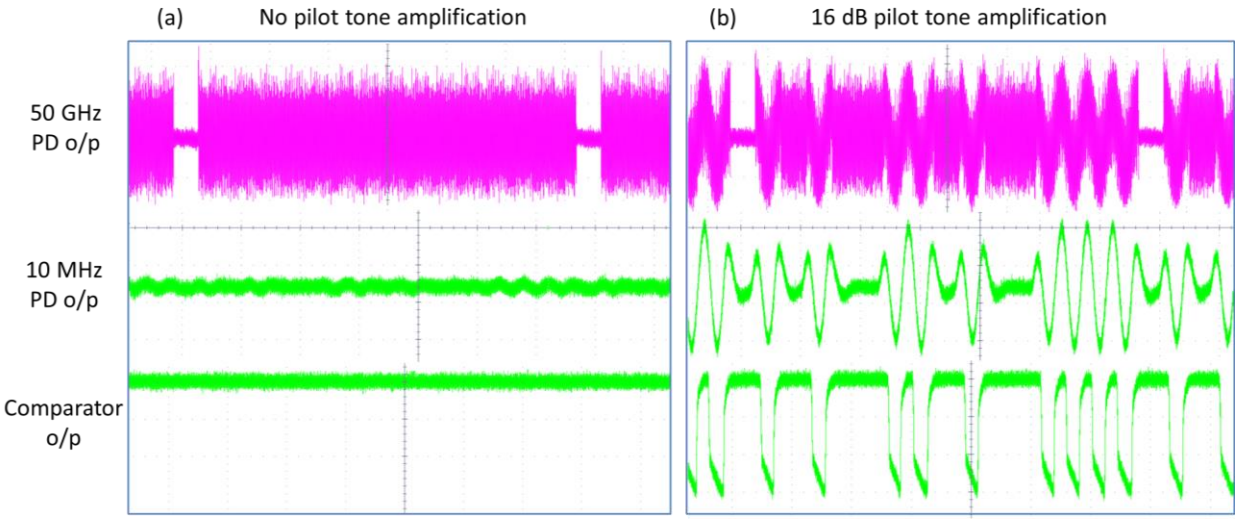

Fig. 4.2 (a) No pilot-tone amplification; (b) 16 dB pilot-tone amplification. The horizontal scale for both plots is 400 ns/div.

differential comparator integrated circuit (see Fig. 4.1 (b)) is used to reshape the received composition code into a binary stream and sent to a Virtex-6 FPGA module. The FPGA module has a pre-defined mapping table for translating the binary stream into a specific configuration command to configure optical network elements.

Fig. 4.2 depicts the waveforms in the system without (a) and with (b) pilot-tone amplification.

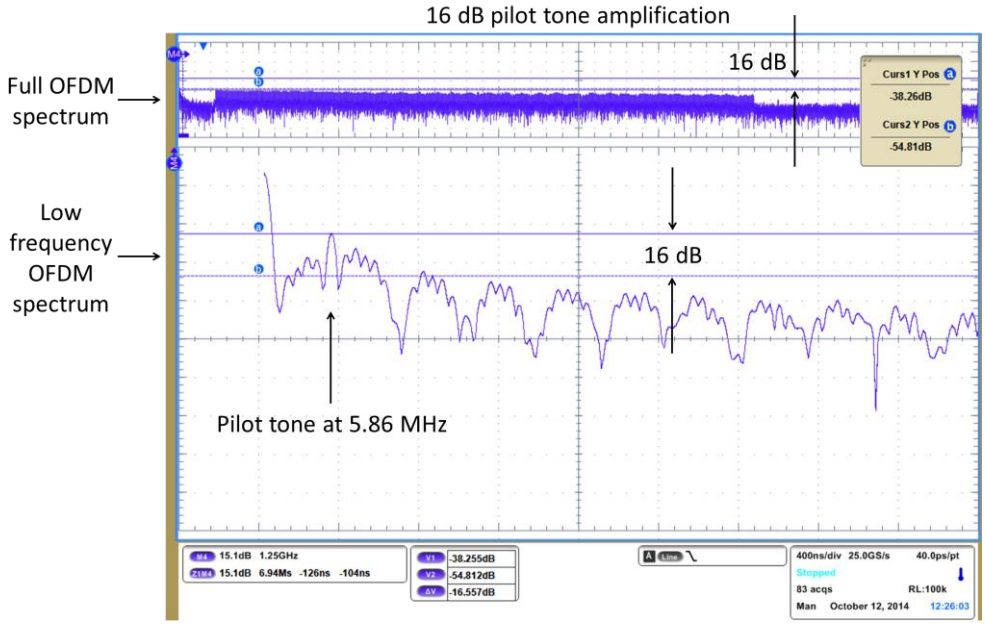

Fig. 4.3 Full OFDM spectrum (upper) and low frequency OFDM spectrum (lower); the horizontal scale for the upper spectrum is 1.25 GHz/div and is 6.94 MHz/div for the lower spectrum.

As can be seen in Fig. 4.2 (a), due to the lack of pilot-tone amplification, the 10 MHz photodiode is barely able to register the pilot-tone. As a consequence, the comparator output stays high throughout. With a pilot-tone amplification of 16 dB (Fig. 4.2 (b)), the pilot-tone is well received by the photodiode and the desired binary signal is output by the comparator. Fig. 4.3 shows this pilot-tone amplification in the frequency domain where the pilot-tone amplitude is 16 dB higher than the highest data subcarrier amplitude.

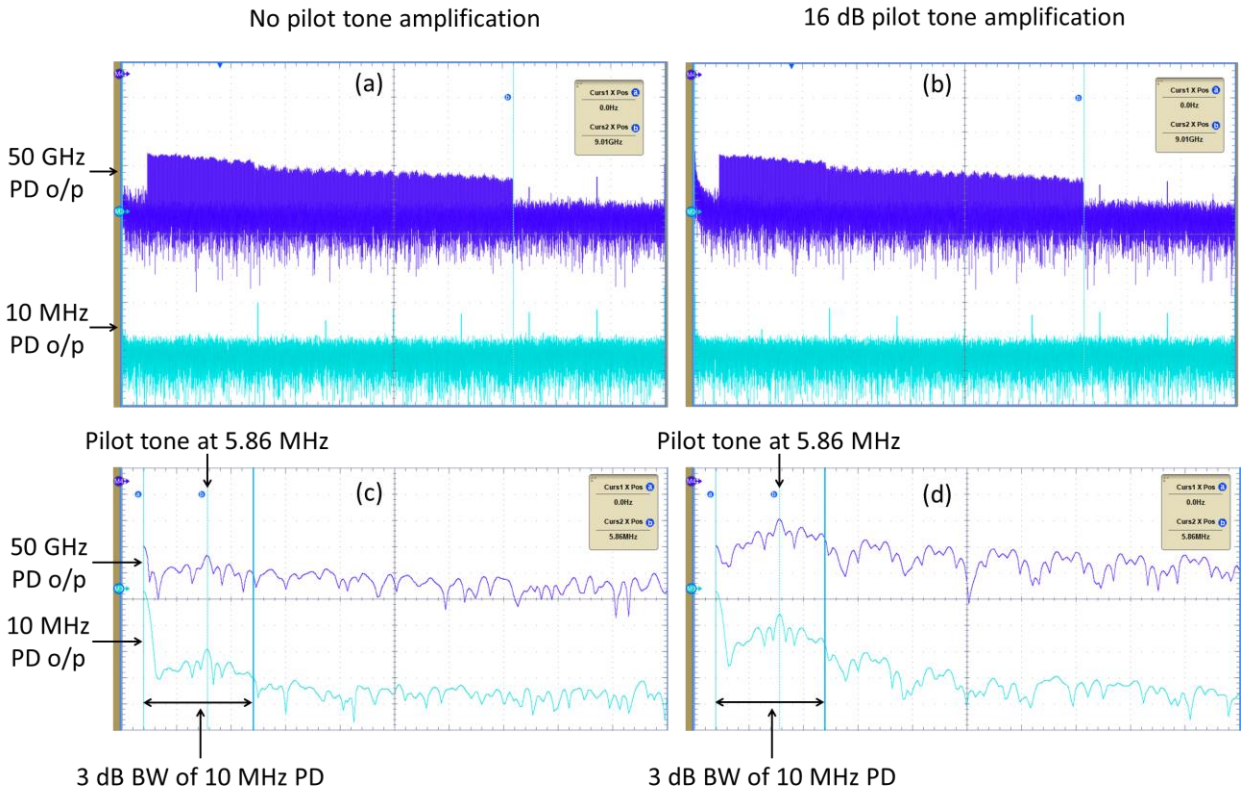

Fig. 4.4 Full OFDM spectra for the 50 GHz and 10 MHz photodiodes with (a) no pilot-tone amplification; (b) 16 dB pilot-tone amplification; the horizontal scale for both (a) and (b) is 1.25 GHz/div; Low frequency OFDM spectra for the 50 GHz and 10 MHz photodiodes with (c) no pilot-tone amplification; (d) 16 dB pilot-tone amplification; the horizontal scale for both (c) and (d) is 5 MHz/div.

In Figs. 4.4 (a) and (b), one can see that the 10 MHz PD is unable to reproduce the full OFDM spectrum (up to 9 GHz) as the frequency range of subcarriers carrying data is higher than the bandwidth of this PD. The 10 MHz PD is able to fully reproduce the lowest subcarrier at 5.86 MHz i.e. the pilot-tone, as can be seen in Figs. 4.4 (c) and (d).

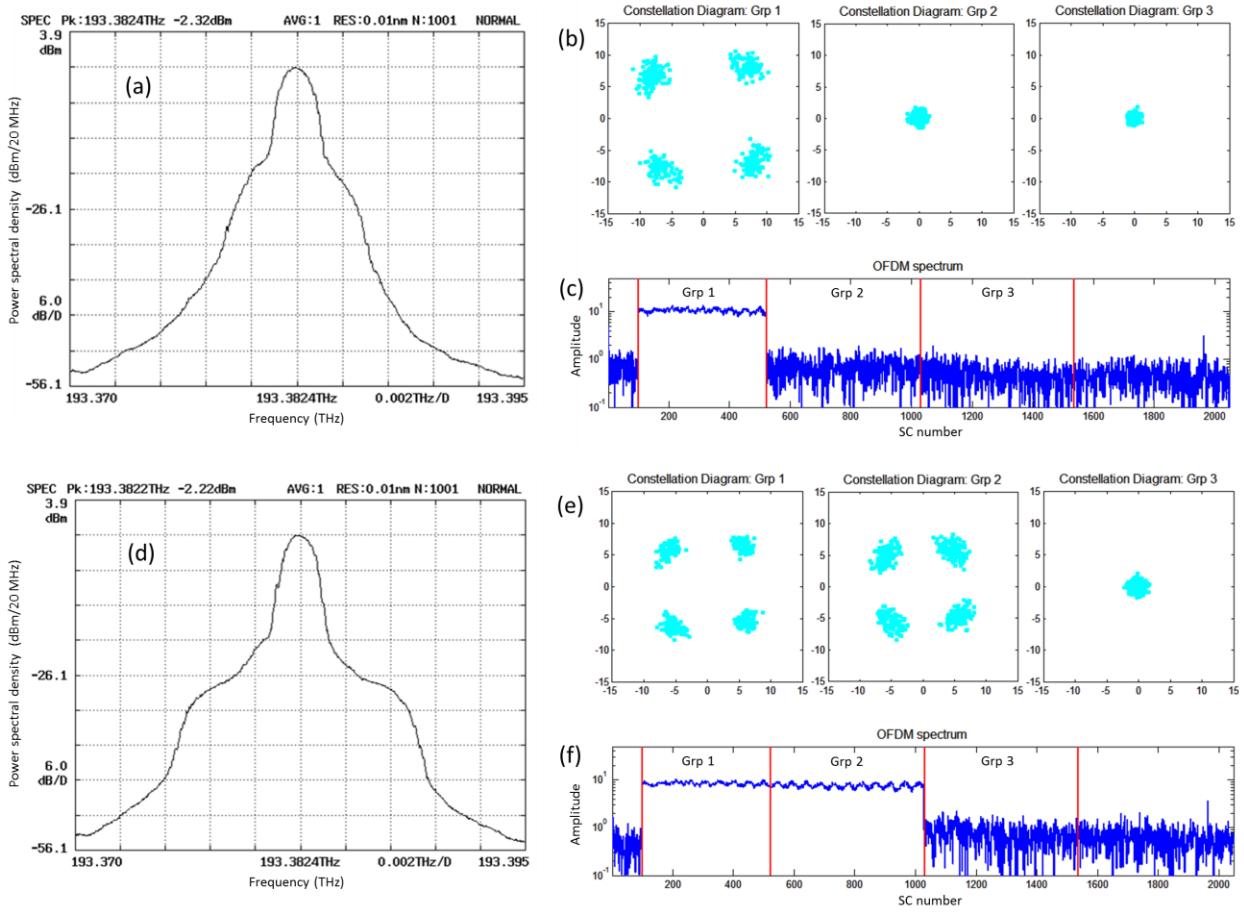

Fig. 4.5 (a)-(c) OFDM signal with 3 subcarrier (SC) groups modulated by QPSK, null and null respectively, (a) the optical spectrum of the OFDM signal, (b) the constellation diagrams of the 3 SC groups, (c) the electrical spectrum of the OFDM signal; (d)-(f) OFDM signal with 3 subcarrier (SC) groups modulated by QPSK, QPSK and null respectively, (d) the optical spectrum of the OFDM signal, (e) the constellation diagrams of the 3 SC groups, (f) the electrical spectrum of the OFDM signal.

Figs. 4.5 and 4.6 depict the optical and electrical spectra and the constellation diagrams for the OFDM signals used in the experiment in the latter part of this chapter. The electrical and hence, the optical bandwidth of the OFDM signal is varied by applying null modulation to the outer SC groups. For example, one can see that the electrical and optical bandwidth of the QPSK+null+null OFDM signal (Fig. 4.5 (a)-(c)) is lower than the corresponding bandwidth of the QPSK+QPSK+QPSK OFDM signal (Fig. 4.6 (d)-(f)).

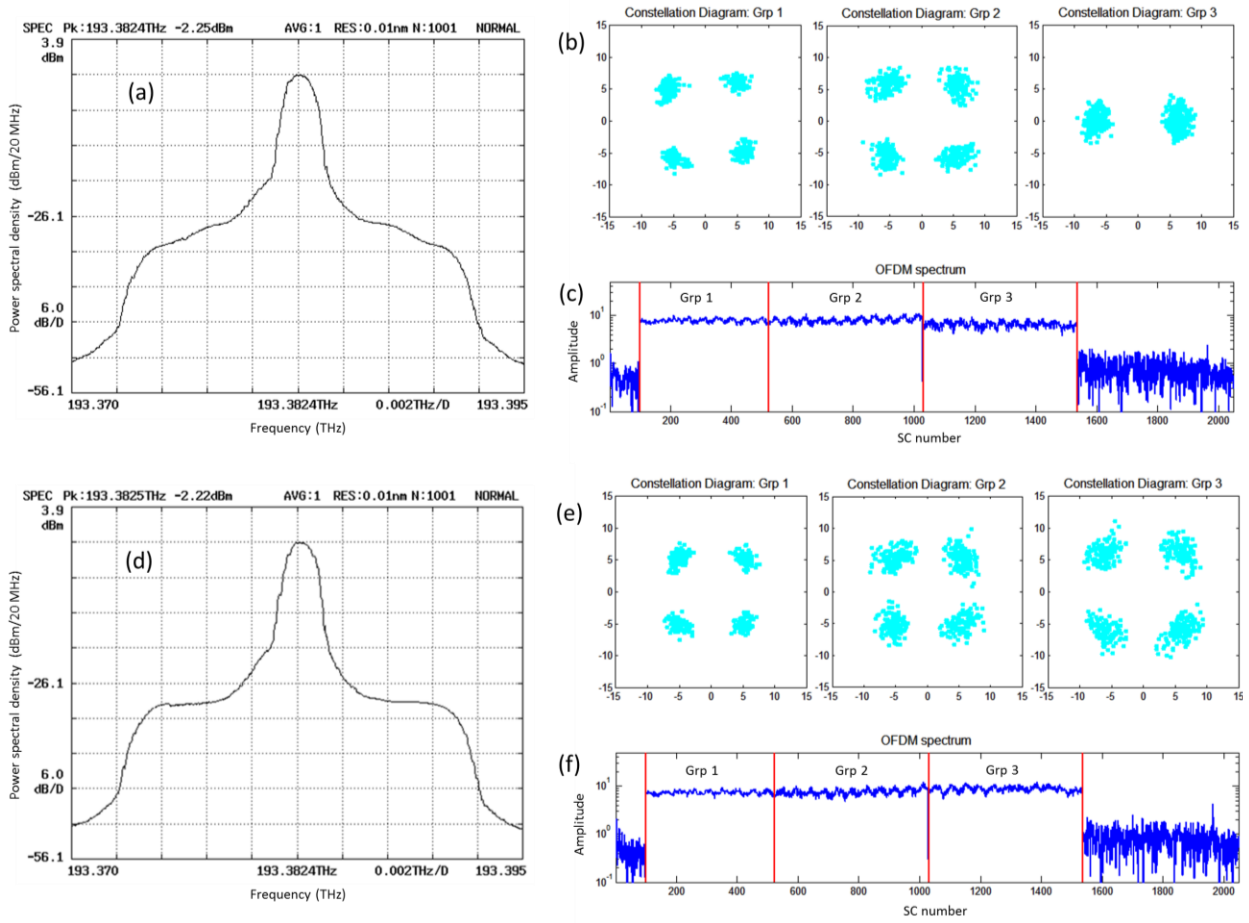

Fig. 4.6 (a)-(c) OFDM signal with 3 subcarrier (SC) groups modulated by QPSK, QPSK and BPSK respectively, (a) the optical spectrum of the OFDM signal, (b) the constellation diagrams of the 3 SC groups, (c) the electrical spectrum of the OFDM signal; (d)-(f) OFDM signal with 3 subcarrier (SC) groups all modulated by QPSK, (d) the optical spectrum of the OFDM signal, (e) the constellation diagrams of the 3 SC groups, (f) the electrical spectrum of the OFDM signal.

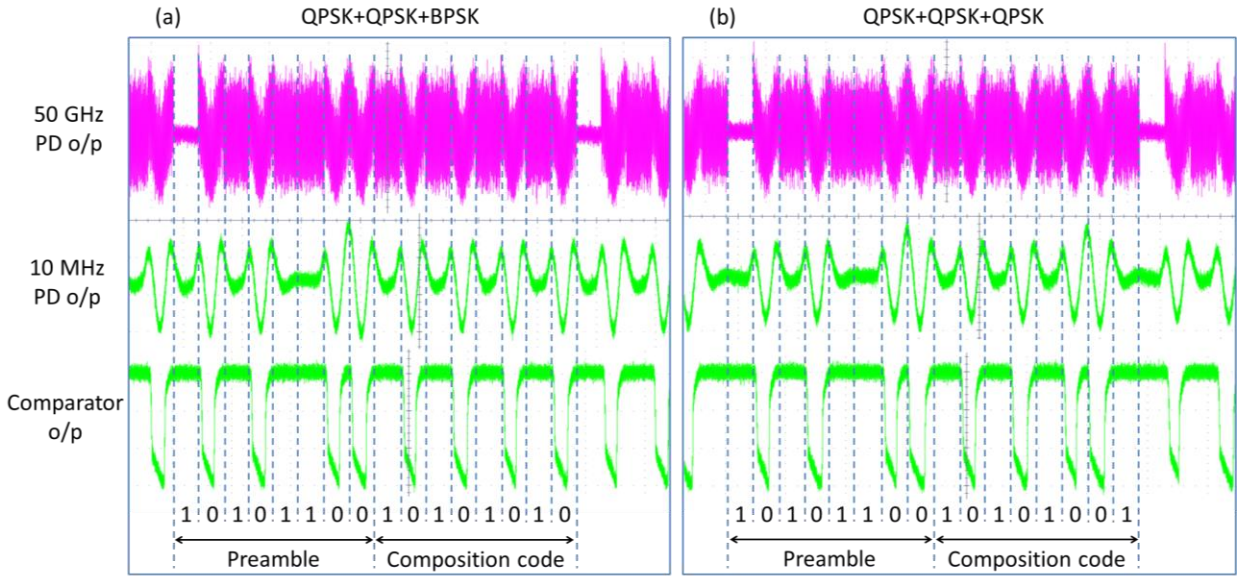

Fig. 4.7 (a) OFDM signal with 3 subcarrier groups modulated by QPSK, QPSK and BPSK respectively; (b) OFDM signal with 3 subcarrier groups modulated by QPSK, QPSK and QPSK respectively; the horizontal scale for both plots is 400 ns/div.

Fig. 4.7 shows 2 different OFDM configurations and their associated composition code waveforms. As explained earlier in this section, the composition code is preceded by the preamble to enable correct synchronization of the composition code at the distributed controller.

Compared with the distributed control scheme, to complete the re-configuration in the centralized scheme, the OFDM transmitter sends its traffic information to the SDN controller located in the cloud through several routers on specific protocols (e.g. OpenFlow), and the SDN controller parses the received traffic information and sends corresponding configuration commands to the FPGA, again through several routers. Finally, the FPGA translates the commands into specific device configurations. It is apparent that this control method takes a longer route and involves more command parsing, which is the key disadvantage as compared with the pilot-tone distributed scheme that is proposed here.

4.3 Experiment setup and results

The experiment network setup is depicted in Fig. 4.8 (a). A double side-band (DSB) intensity modulation and direct detection OFDM transmitter (Tx) is used as a bandwidth variable transmitter (BVT) with a maximum channel bandwidth of 18 GHz and 2048 subcarriers. QPSK

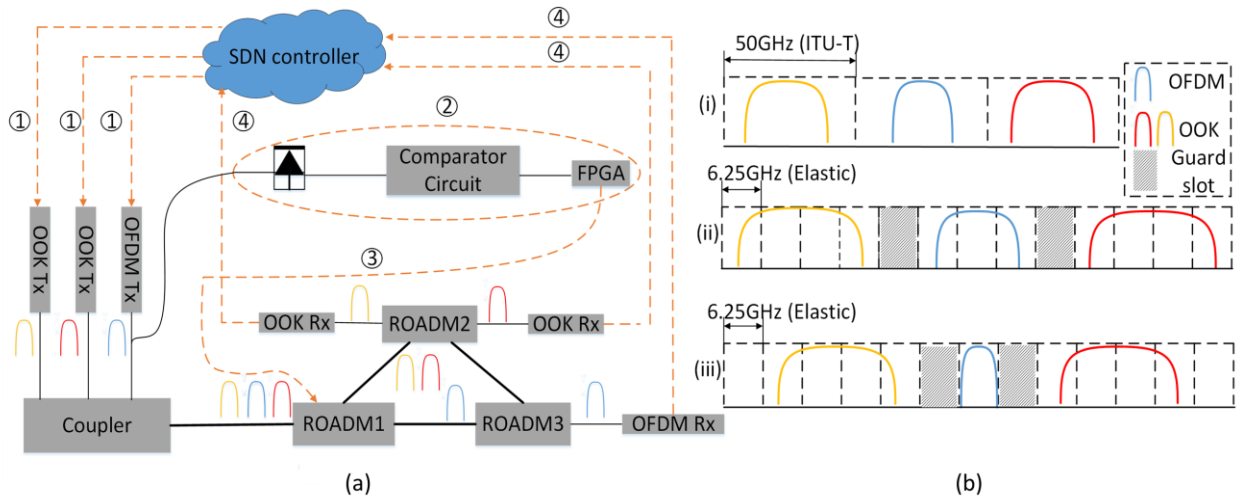

Fig. 4.8 (a) The experimental elastic optical network setup for pilot-tone assisted control; (b) Comparison between the fixed ITU-T 50 GHz grid network (i), and the flexible grid (6.25 GHz passband granularity) supported in our ROADM i.e. (ii) and (iii). The ROADM dynamically switches between configurations (ii) and (iii) based on the OFDM composition information conveyed by the pilot-tone.

and BPSK modulation formats are used while keeping the bit error rate (BER) below a pre-defined threshold of 1×10^{-4} for this experiment.

Based on the traffic load given by the SDN controller, the OFDM transmitter adjusts its optical bandwidth between 18 GHz, 12 GHz, and 6 GHz by turning on/off a specific number of subcarriers. In addition, two wavelength tunable 10 Gb/s DSB on-off keying (OOK) side channels are coupled with the OFDM channel. The composite signal then enters a reconfigurable optical add-drop multiplexer (ROADM) network and is routed to different add/drop sites. The ROADM setup is implemented with wavelength selective switches (WSSs), which can assign passbands in increments of 6.25 GHz as shown in Fig. 4.8 (b). In our experiment, ROADM1 (See Fig. 4.8 (a)) is controlled by the pilot-tone assisted scheme. At the receiver, the real-time BER is measured to monitor traffic performance of each channel (see Fig. 4.9 (a)).

OFDM composition	Spectral Efficiency in Elastic Network (b/s/Hz)	Spectral Efficiency in ITU-T 50GHz grid (b/s/Hz)
QPSK+null+null	0.36	0.17
QPSK+QPSK+null	0.41	0.21
QPSK+QPSK+BPSK	0.42	0.23
QPSK+QPSK+QPSK	0.45	0.25

Table 4.1 Spectral efficiency comparison between elastic and fixed ITU-T 50 GHz grid networks

The experimental procedure is as follows: (1) The SDN controller sends the traffic load to the OFDM transmitter and tunes central wavelengths of both side channels. On receiving the traffic load, the OFDM transmitter adjusts its bandwidth. (2) The pilot-tone is processed by the photodiode and comparator circuit and sent to the FPGA. (3) The FPGA configures the ROADM to closely match the new spectrum of all three channels, thus maintaining high spectral

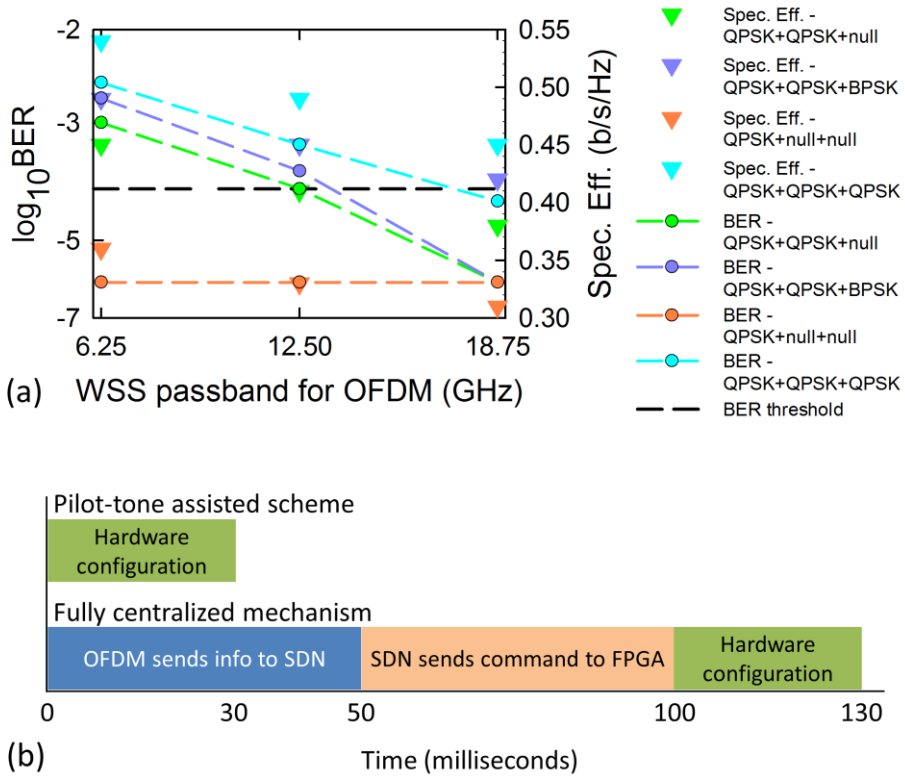

Fig. 4.9 (a) OFDM channel BER and the combined spectral efficiency vs. WSS passband assigned to the OFDM channel under different OFDM compositions. (b) Reconfiguration latency comparison between the pilot-tone assisted scheme and the fully centralized mechanism.

efficiency. Note that in every configuration, four 6.25 GHz slots are always assigned for each side channel, to keep their BERs below 1×10^{-9}. (4) If the BER is above the threshold, the SDN

controller repeats step (1)-(4).

In Fig. 4.9 (a), the OFDM channel BER performance with different OFDM compositions and different WSS passband cases is investigated. The valid OFDM subcarriers are divided into three groups of approximately 6 GHz optical bandwidth each and are modulated with QPSK, BPSK or left unmodulated. We see lower BER when the WSS passband closely matches the OFDM optical bandwidth as shown in Fig. 4.9 (a). The maximum combined spectral efficiency (OFDM and side channels) for each OFDM composition is shown in Table 4.1. Compared with the ITU-T 50 GHz grid, the combined spectral efficiency is significantly improved in our elastic optical network.

Fig. 4.9 (b) shows the latency comparison between the pilot-tone assisted control scheme vs. the fully centralized mechanism. The instant the OFDM transmitter finishes assigning new subcarriers is used as the starting time for latency calculation. In the pilot-tone assisted control scheme, the pilot-tone processing takes tens of microseconds. The main latency comes from the WSS switching time, which is experimentally measured to be around 30 ms. On the other hand, in the fully centralized mechanism, the additional communication time between the SDN controller and network devices is measured to be around 100 ms, requiring a larger cache to avoid data loss, which is quite disadvantageous for use in high data rate networks.

4.4 Conclusions

In this chapter, I have experimentally demonstrated an OFDM pilot-tone assisted distributed control scheme with a fast network reconfiguration time of 30 ms. This scheme shows the inherent capability of OFDM to work with low speed and hence low cost photodiodes which enables inexpensive distributed controllers to be built. Such an OFDM pilot-tone assisted control scheme could be a key enabling technology for next-generation high speed elastic optical networks.

Chapter 5

Optical re-timing using temporal soliton molecules

5.1 Introduction

Re-timing is one of the three important processes that have been proposed to regenerate optical signals over long haul optical fiber links, the other two processes are re-amplification and re-shaping. One method to achieve signal regeneration is by converting the optical (O) signal to the electrical (E) domain, processing the signal in the electrical domain and then converting the electrical signal back to the optical domain i.e. an O-E-O regenerator. However, this technique is limited by the speed of the electrical processing hardware and cannot be scaled up easily to higher bit-rate signals. For this reason, there is research interest in performing the regeneration of the optical signal entirely in the optical domain without the need for the intermediate electrical processing step. While the EDFA has solved the problem of re-amplification, optical re-shaping and re-timing do not have a comparable optical solution with wide adoption. In this chapter, I present and experimentally demonstrate an optical re-timing scheme and also compare its energy efficiency to commercially available optical signal regeneration hardware.

Optical re-timing schemes demonstrated to date rely on the interaction of the incoming data stream with a stable control signal via cross-phase modulation (XPM) in a highly nonlinear fiber (HNLF) [61, 62], via cross-absorption modulation (XAM) in an electroabsorption modulator (EAM) [63, 64] or via cross-gain modulation (XGM) in a semiconductor optical amplifier (SOA) [65, 66]. Periodically poled waveguide [67] and nonlinear optical loop mirror (NOLM) [68] based schemes have also been demonstrated. The schemes reported in [61, 63, 64] involve wavelength conversion in the re-timing stage and hence also use a second wavelength conversion

step to revert to the original carrier wavelength, thus increasing system complexity and cost. Re-timing schemes that involve single-step wavelength conversion [66, 67, 68] may find limited in-line application due to the possibility of wavelength blocking in optical network nodes [64].

In this chapter, a different approach to optical re-timing is used by utilizing the temporal properties of bound soliton states or so-called "soliton molecules". This re-timing scheme operates at a single wavelength and works with – but is not limited to – readily available single-mode optical fibers (SMFs) and dispersion compensating fibers (DCFs) as the principal re-timing elements.

The "Experimental observation of interaction forces between solitons in optical fibers" was first reported by F.M. Mitschke and L.F. Mollenauer in 1987 [69]. Bound states of solitons were first predicted by B. Malomed [70]. M. Stratmann *et al.* showed the existence of a bound state of solitons in anti-phase in a dispersion alternating fiber span in 2002 [71]. In 2005, M. Stratmann, T. Pagel, and F. Mitschke [72] discussed utilizing bisolitons to create a three-letter alphabet ("empty slot," "dispersion managed soliton," and "bisoliton"), replacing the conventional binary alphabet. An in-depth investigation of this solution of the nonlinear Schrödinger equation was conducted by I. Gabitov *et al.* in 2007, revealing (i) the existence of a second branch of solutions (higher bisoliton energy for the same residual dispersion) with a larger spacing between the bound pulses and (ii) that there is a maximum dispersion (the "limit point" where the first branch of solutions merges into the second one) for which bisolitons are supported [73]. The first experimental proof of existence of this second set of solutions was observed in the same year, again by F. Mitschke's group [74]. This has also been confirmed by a more rigorous mathematical treatment by M. Shkarayev and M.G. Stepanov in 2009 who also speculated about a four-letter alphabet, further increasing the capacity of soliton based transmission systems [75]. The existence of this twin family of solutions is emphasized here because the awareness about the phenomenon is important for correct interpretation of the results.

Re-timing in high-speed fiber-optic transmission systems is required (i) at the receiver site of the transmission system where the optical signal is converted back into the electrical domain and the data to be processed requires correct timing (in order to make a correct threshold decision) or (ii) along an optically transparent transmission path, e.g. at an optical time division add/drop multiplexer [76], where a local and, thus, unsynchronized tributary channel has to be

synchronously time division multiplexed into the assigned time slots of the passing-by higher speed signal (e.g. a 10 Gb/s channel is dropped/added locally from/to a 100 Gb/s – 10 × 10 Gb/s TDM – data stream). The performance of such an optical re-timing or synchronization scheme for use in future high-speed optical networks is investigated and reported here.

5.2 Operating principle

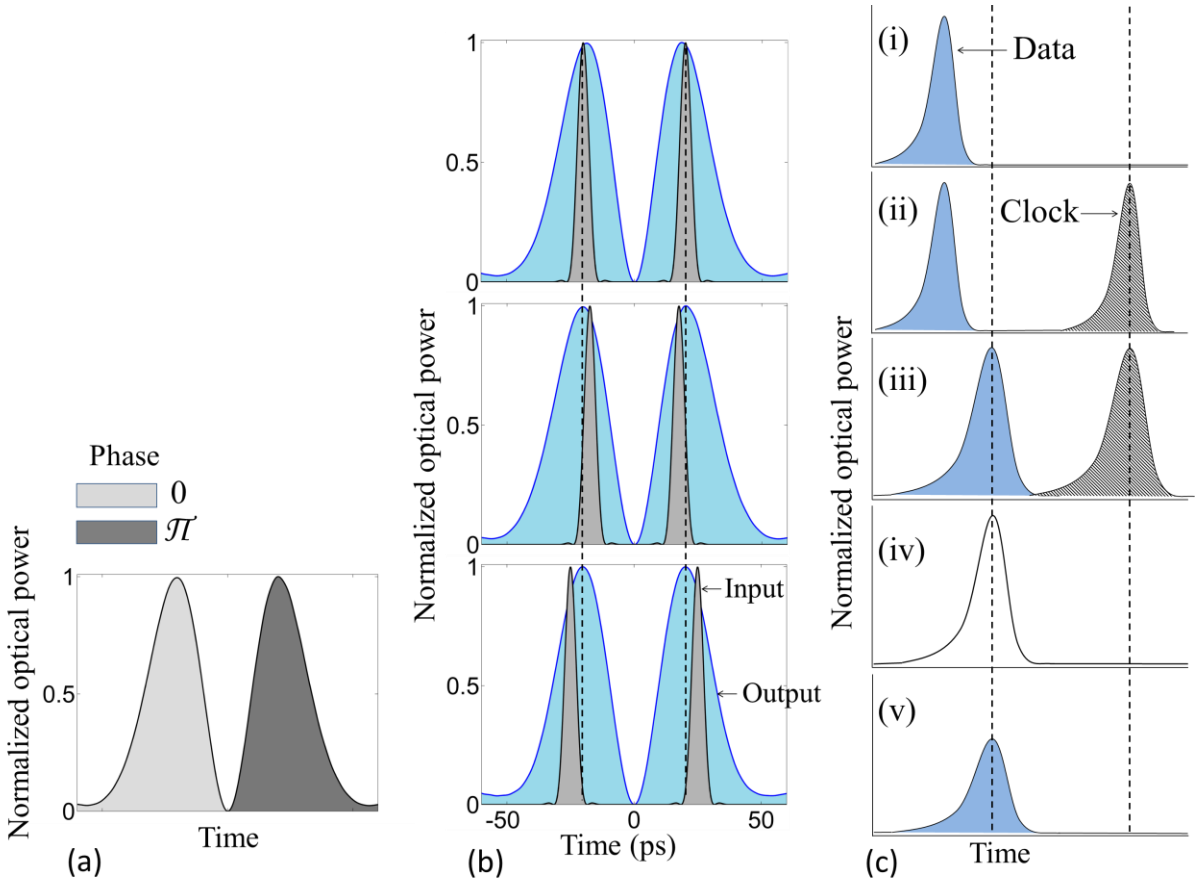

Fig. 5.1 (a) The soliton molecule – two solitons with a π phase shift between them forming a stable bound structure. (b) Results of numerical simulation at 32.4 dBm peak pulse power with the soliton molecule at various initial separations, the evolution to an equilibrium separation takes place in all three cases. (c) The principle of the re-timing scheme: (i) incoming data offset from its bit center time (ii) data interleaved with a π phase shifted clock such that the data and clock now form a soliton molecule (iii) the molecule relaxes to its equilibrium separation after the fiber span (iv) the de-interleaving window (v) the re-timed data after de-interleaving.

M. Stratmann *et al.* [72] experimentally demonstrated the existence of a bound soliton state with an equilibrium temporal separation in a dispersion alternating fiber span. A soliton pair in anti-

phase (e.g. zero phase for the first pulse and π phase for the second pulse) (Fig. 5.1 (a)) launched into a dispersion alternating fiber span with the equilibrium temporal separation maintains this separation as it propagates along the fiber span. If the pair of pulses is launched with a separation smaller or greater than equilibrium, it evolves into a pair at equilibrium separation (Fig. 5.1 (b)). As this property of returning to an equilibrium separation is analogous to a di-atomic molecule, the bound soliton pair is referred to as a "soliton molecule" [77].

The binding mechanism of the soliton molecule is the attraction (or repulsion, respectively) due to constructive (destructive) interference between the solitons forming the molecule mediated by the optical Kerr effect [74, 78]. As the soliton pulses propagate along the fiber, they acquire chirp. Hence, different time slots within the partially overlapping solitons experience constructive (destructive) interference producing attraction (repulsion) between these time slots. The integral over the entire bound structure gives the net force between the soliton pulses forming the molecule - a net repulsive (attractive) force for separations smaller (larger) than the equilibrium distance. This effect decays exponentially with an increase in separation between the soliton pulses in the anti-phase pair. The stability and dynamics of soliton molecules have been studied in [79, 80]. While we use two-soliton molecules in this experiment, multi-pulse bound solitons have also been demonstrated [81, 82].

The re-timing scheme that I present here is intended for a return-to-zero on-off keying (RZ-OOK) transmission system. The incoming data stream to be re-timed is temporally interleaved with a clock stream consisting of a series of pulses at the data stream bit rate. The clock stream is set to be in anti-phase with the data stream such that any two adjacent soliton pulses – one from the data stream and the other from the clock stream – can form a soliton molecule in a dispersion alternating fiber span. An offset of the data stream pulse from its designated temporal location at the center of the bit slot stretches or compresses the soliton molecule, with the molecule ultimately relaxing to its equilibrium separation after propagation through the dispersion alternating fiber span (Fig. 5.1 (c)). The fiber span parameters, the soliton pulse width and soliton peak pulse power launched into the fiber span determine the value of the equilibrium separation. As the addition of the clock stream doubles the bit rate, the equilibrium separation must equal one half of the bit period of the incoming data stream. Thus, the incoming data

stream can be re-timed. A clock pulse either before or after (or both) every data pulse is required for the formation of a soliton molecule.

Bound solitons have been studied for timing performance improvement in optical communication systems. Maruta *et al.* [83] investigated the use of bound soliton states for producing error preventing line coding schemes. A re-timing scheme using two soliton pulse trains at different wavelengths interacting via cross-phase modulation (XPM) has been demonstrated [84]. In contrast, our scheme utilizes two soliton streams at the same wavelength interacting via a balance of fiber dispersion and self-phase modulation (SPM).

5.3 Experiment setup

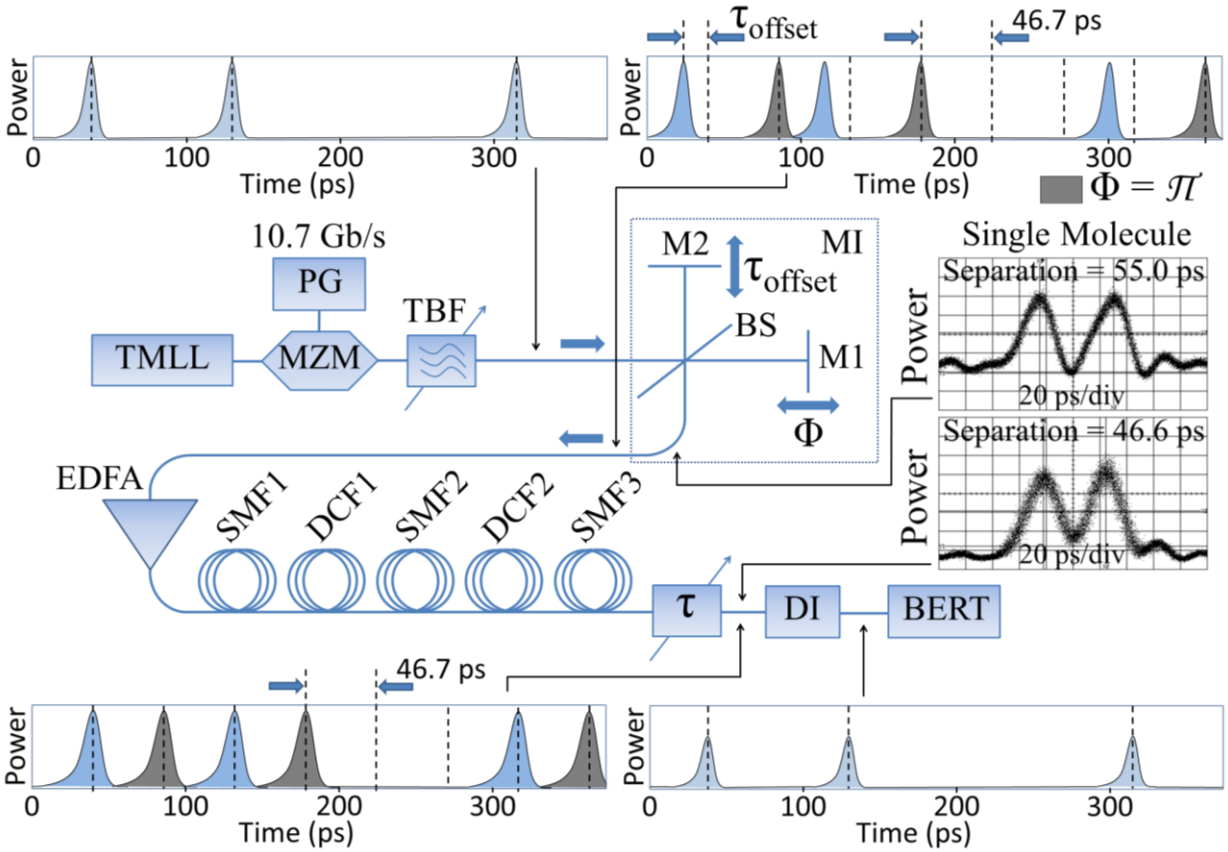

Fig. 5.2 Experiment setup - M1, M2: mirrors of the Michelson interferometer (MI), BS: beam splitter. The composite stream consists of the 10.7 Gb/s data stream and the 10.7 Gb/s pseudo-clock stream (replica of the data stream), every data pulse has a clock pulse succeeding it.

A tunable mode locked laser (TMLL) generates ~2 ps full width at half maximum (FWHM)

pulses at 1550 nm and 10.7 GHz repetition rate (Fig. 5.2). This pulse stream is modulated by a Mach-Zehnder modulator (MZM) driven by a 10.7 Gb/s 2^7 -1 pseudo-random binary sequence (PRBS) from the pattern generator (PG). A bandwidth tunable optical bandpass filter (TBF) is used to set the pulse width. A Michelson interferometer (MI) pictured in Fig. 5.3 interleaves this stream with a delayed (by half bit time of 46.7 ps) version of itself. In this composite stream, the first stream is taken to be the data stream to be re-timed. The delayed 10.7 Gb/s stream is used as a pseudo-clock stream. This pseudo-clock stream is held steady in time and the data stream is delayed or advanced (τ_{offset}) from its bit center time by varying the position of mirror M2 and

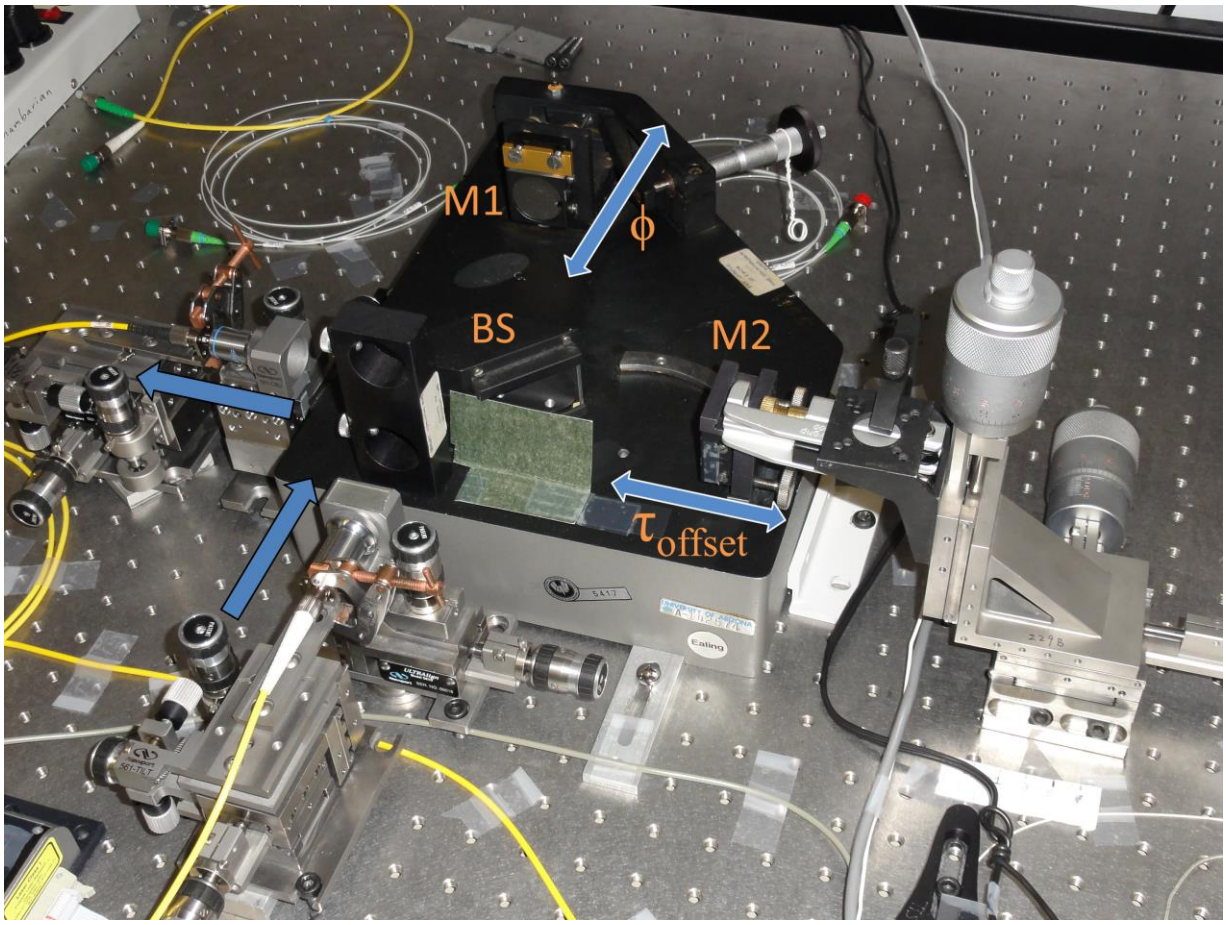

Fig. 5.3 Photograph of the interferometer setup - M1, M2: mirrors of the Michelson interferometer, BS: beam splitter.

thus the optical path length in that arm. The anti-phase relation ($\varphi = \pi$) between adjacent soliton pulses is achieved by setting the position of mirror M1 so that the optical path length difference between the two arms produces a phase difference of π radians between the data and pseudo-

clock stream, this is checked by looking for carrier suppression in the spectrum of the composite stream. The Michelson interferometer serves two purposes – it produces a data stream that can be advanced or delayed to simulate a real world out of synchronization data stream and it also combines this data stream with the clock stream, producing soliton pairs in anti-phase (composite stream) necessary for formation of soliton molecules for re-timing.

Fiber	**Length (km)**	**Attenuation (dB/km)**	**Dispersion parameter β_2 (ps^2/km) @ 1550 nm**	**Non-linearity co-efficient γ (1/W-km)**
SMF1/SMF2/ SMF3	25.26	0.19	-21.66	1.37
DCF1	2.48	1.53	207.63	5.24
DCF2	1.91	1.57	269.59	5.24

Table 5.1 Fiber parameters

The composite stream is amplified by a high power erbium-doped fiber amplifier (EDFA) and launched into the dispersion alternating fiber span (Table 5.1) consisting of three identical SMF fiber spools (SMF1, SMF2 & SMF3) and two dispersion compensation modules (DCF1 and DCF2) all fusion spliced with ~0.02 dB loss at each splice. The minimum required length of the fiber span for the perturbed soliton molecules to relax to their equilibrium separation is best described in terms of the dispersion length L_D [85] for a single soliton at the path average dispersion β_2^{avg} of the fiber span. With a β_2^{avg} of -7.63 ps^2/km for the fiber span, using soliton pulses 2 ps to 8 ps wide translates to a fiber span length that ranges from $153L_D$ to $10L_D$ respectively.

At the end of the fiber span, the slow temporal advance (delay) of the composite stream due to thermal contraction (expansion) of the fiber span is compensated for by manually adjusting an optical delay line (τ). Later on, clock recovery should be used for this purpose. Thus, the clock pulses are held steady in time and all mutual time shifts between the data and clock pulses due to the soliton molecule effect are translated to time shifts in the data pulses alone (Fig. 5.1 (c), (ii) & (iii)). The composite stream is then fed to a de-interleaver (DI) that temporally extracts the 10.7 Gb/s data stream from the composite stream (Fig. 5.1 (c), (iv) & (v)). A pair of MZMs

connected in optical series is used for this purpose. The sampling window width for the de-interleaver is 12 ps FWHM. The de-interleaved data is fed to a bit error rate tester (BERT) for analysis. As the jitter statistics for interacting solitons deviates from a Gaussian distribution [86], using a BERT is preferred to deriving the bit error rate (BER) from eye diagrams.

In this proof-of-concept experiment, I manually set the clock stream to have an anti-phase relation with the data stream by adjusting the position of mirror M1. In practice, an optical phase locked loop (OPLL) [87] can be employed to sense the phase of the incoming data stream, the anti-phase clock stream could then be derived from the OPLL.

5.4 Experiment results and discussion

I first determine the soliton pulse width and soliton peak pulse power range at which the equilibrium separation of the soliton molecule closely matches one half of the bit period i.e. 46.7

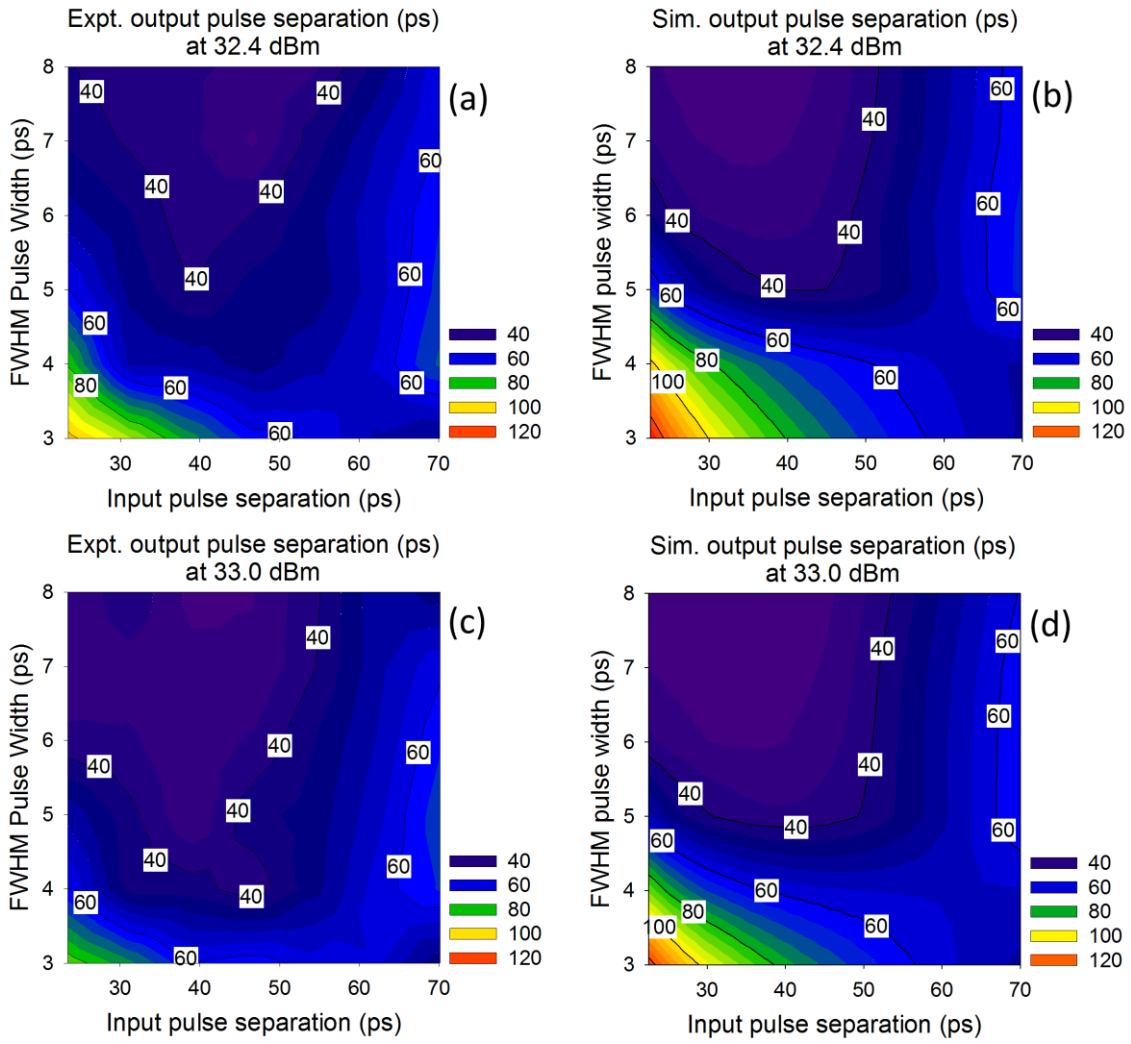

Fig. 5.4 Output pulse separations over a range of pulse widths and input pulse separations for: 32.4 dBm peak pulse power - (a) Experiment and (b) numerical simulation, 33.0 dBm peak pulse power - (c) Experiment and (d) numerical simulation.

ps for a 10.7 Gb/s system. A single soliton pair in anti-phase with variable separation, pulse width and peak pulse power is launched into the fiber and the output pulse separation is noted as a function of these variations.

For solitons launched into the fiber at 32.4 dBm peak pulse power, a pulse width of 5 ps is a good match (Fig. 5.4 (a)); this is also true for a pulse width of 4 ps for 33.0 dBm peak pulse power (Fig. 5.4 (c)). Results of corresponding numerical simulations are also shown (Fig. 5.4 (b) and Fig. 5.4 (d)). Numerical simulations were carried out using a commercial fiber transmission simulation tool that uses the split-step Fourier method [85]. All relevant experiment and fiber parameters are accounted for in the simulation model. A soliton pulse width of 5 ps is used for the remainder of the experiment as it allows for lower peak power levels to be used. Thus, with 5

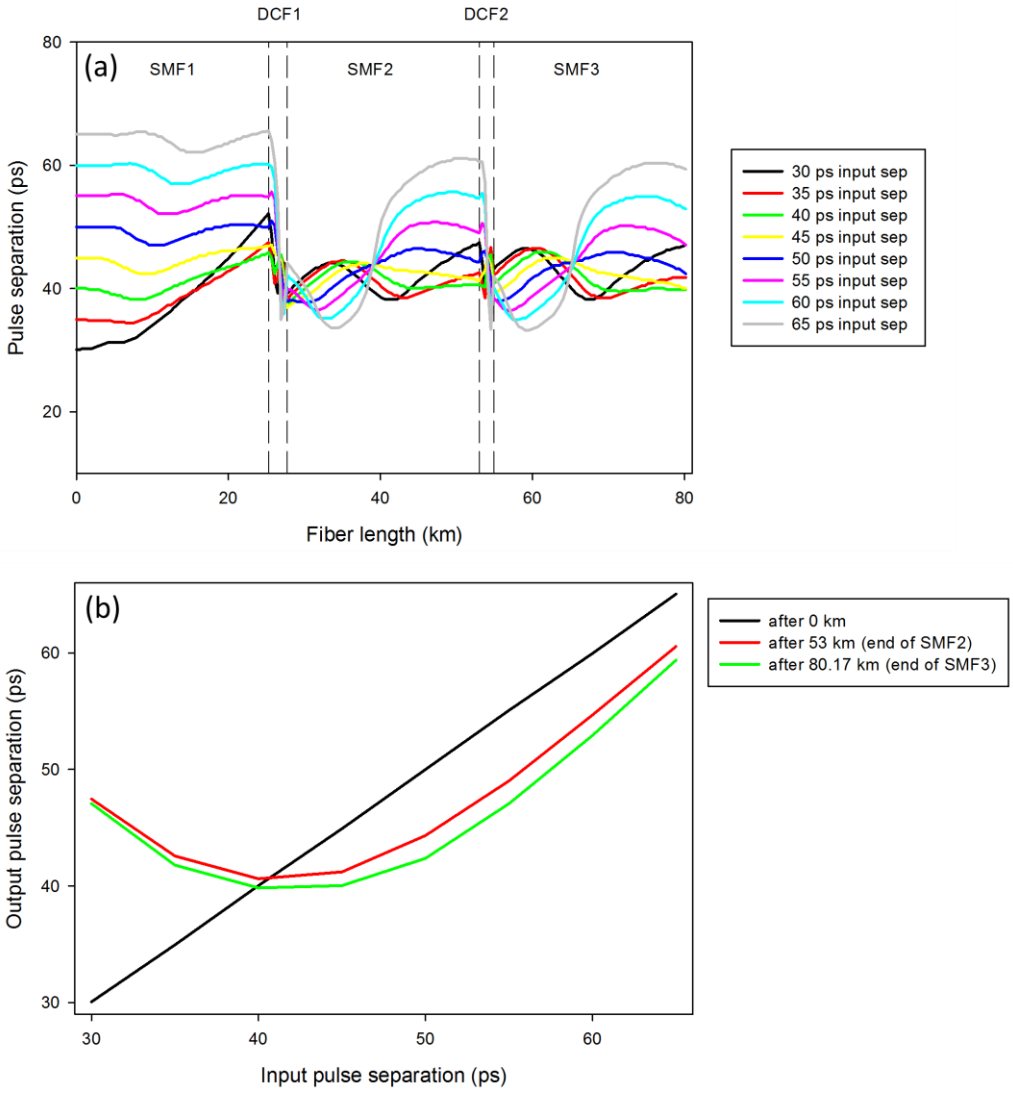

Fig. 5.5 (a) Pulse separation along the fiber span for various values of input pulse separation (b) Pulse separation vs. input pulse separation at various points along the fiber span

ps wide soliton pulses, the re-timing fiber span has a length of $24L_D$ which is an adequate length over which the soliton molecule can relax into its equilibrium separation. Numerical simulations reveal that for the experiment parameters used, the minimum propagation distance necessary for the soliton molecule to relax into its equilibrium separation is 53 km along the dispersion alternating fiber span. This can be seen in Figs. 5.5 (a) and (b). Hence, our fiber span with a length of 80.17 km is adequate for the purpose. The pulse energy (resulting from the aforementioned peak pulse power, pulse width and pulse shape) corresponds to what is referred to as the "first branch" or "first order" bisoliton in literature (see fourth paragraph of Sec. 5.1 and references therein).

With the pulse width kept constant at 5 ps, the composite stream is launched into the re-timing fiber with a variation in the offset of the data stream from its bit center time. BER performance for peak pulse power close to the estimated power (~32 dBm) is measured with 32.2 dBm peak pulse power giving the best re-timing performance (Fig. 5.7 (b)).

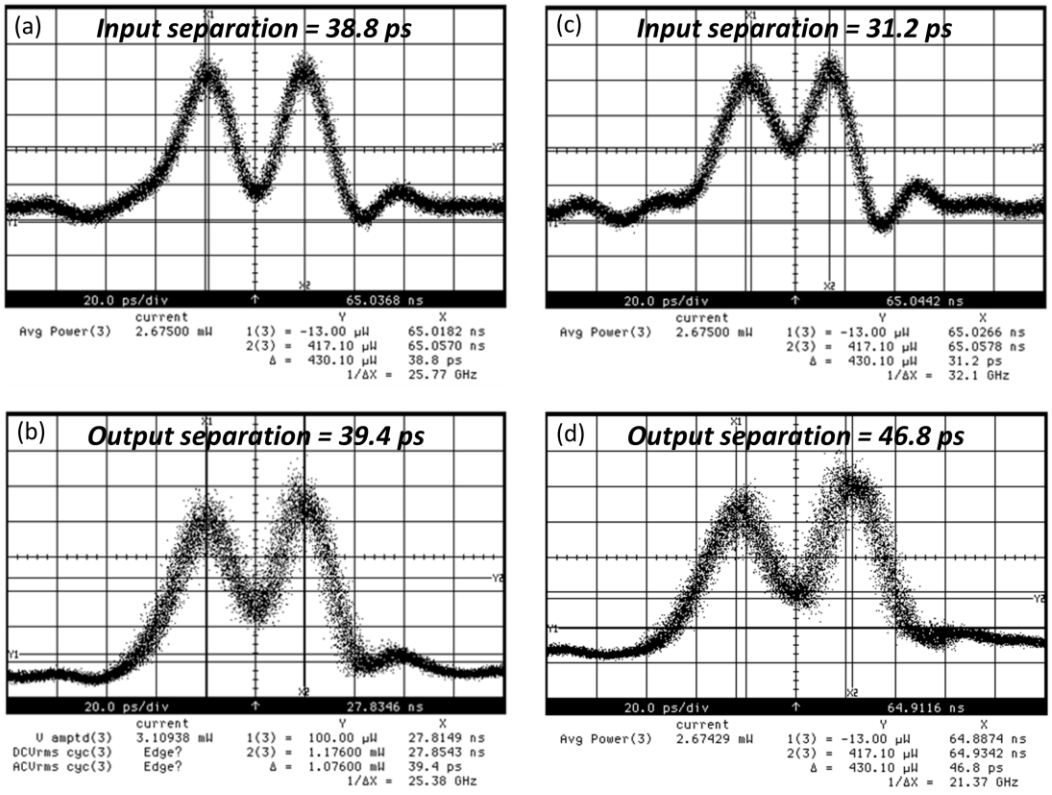

Fig. 5.6 Pulse separation after the fiber span (b), (d) for 2 values of input pulse separation (a), (c) respectively, for 32.4 dBm peak pulse power.

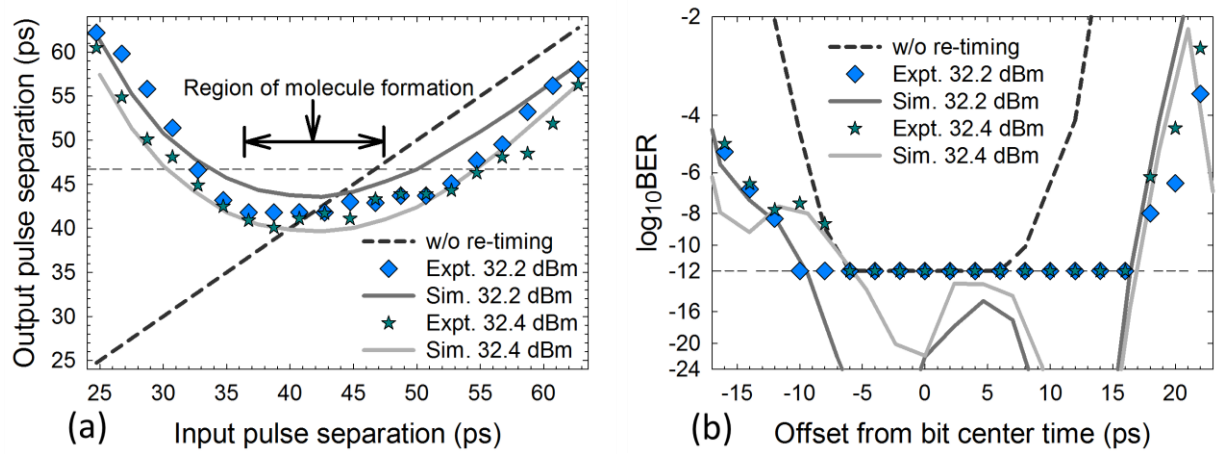

Fig. 5.7 (a) Variation of output pulse separation with peak pulse power at 5 ps FWHM pulse width. There is repulsion at small input separations. The relatively flat part of the plots with the output pulse separation nearly constant with variation in input pulse separation indicates the formation of soliton molecules. At large input separations, the output separations approach those without re-timing. (b) BER performance of the re-timing scheme, 32.2 dBm peak pulse power gives the best re-timing performance.

The re-timing scheme enables data pulses that are offset as far as 16 ps after and 10 ps before bit center time to be received with BER at 10^{-12} which is taken to be the error-free threshold for the experiment. Thus, the re-timing scheme more than doubles the range of delayed offsets from bit center time that can be detected with no error as compared to the case where no re-timing is used. The asymmetry in the re-timing performance is due to the fact that every data pulse has an accompanying clock pulse only *after* it - a data pulse offset before its bit center is further away from its corresponding clock pulse, diminishing the strength of the soliton molecule effect. The summary of the experiment and simulation is shown in Fig. 5.7. The very good agreement between simulation and the experimental measurements of pulse separation and BER provides us with high confidence on the accuracy of our model.

The current experiment setup does not easily allow insertion of clock pulses both before and after every data pulse. In the next section, I extend my numerical simulation to investigate the shifting ability of an enhanced version of the re-timing scheme with clock pulses present both before and after every data pulse.

5.5 An enhanced re-timing scheme: numerical simulation

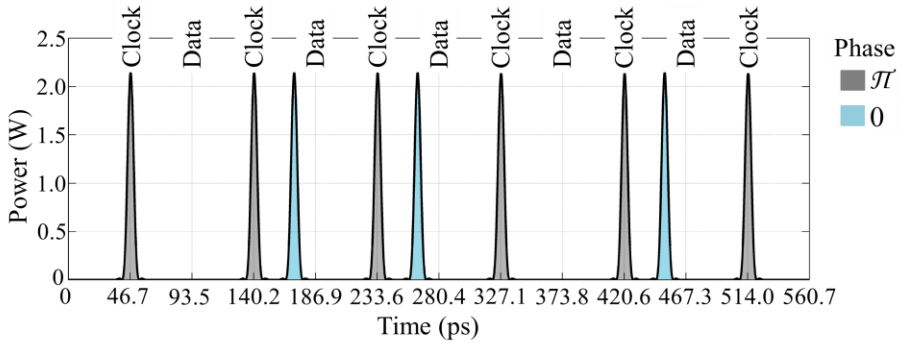

Fig. 5.8 The composite stream used for the numerical simulation consisting of the 10.7 Gb/s data stream and the 10.7 Gb/s clock stream, every data pulse has a clock pulse both before and after it (this is in contrast to the composite stream used in the experiment (Fig. 5.2), where every data pulse has a clock pulse only after it). Here, the data pulses arrive 16 ps before their bit center time.

The enhanced re-timing scheme is identical to the experimental scheme in all respects except for the fact that here the 10.7 Gb/s data stream is interleaved with a 10.7 Gb/s clock stream. This ensures that clock pulses are present both before and after every data pulse (Fig. 5.8). This scheme is analyzed using numerical simulations.

With the pulse width kept constant at 5 ps, the data and clock streams are launched into the fiber in anti-phase as required for soliton molecule formation with a variation in the peak pulse power and offset of the data stream from its bit center time for each simulation instance.

It was found that 33.3 dBm peak pulse power gives the best re-timing performance (Fig. 5.9, Fig. 5.10). The enhanced re-timing scheme enables data pulses that are offset as much as 23 ps before and after bit center time to be received with BER < 10^{-12}. Thus, the enhanced re-timing scheme more than triples the range of offsets from bit center time that can be detected with no error as compared to the case where no re-timing is used. As compared to the experiment, the re-timing in the enhanced scheme is symmetric as both advanced and delayed offsets from bit center are well re-timed (BER < 10^{-12}). This is the consequence of the presence of clock pulses both before and after every data pulse as the data pulse experiences identical force when arriving before or after bit center time.

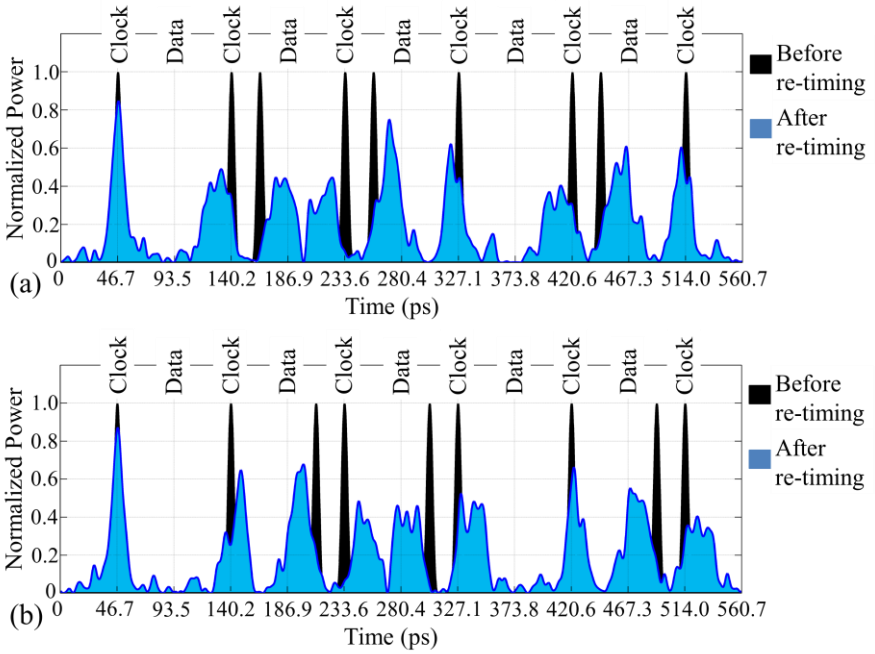

Fig. 5.9 Optical domain waveforms before and after the re-timing fiber span for peak pulse power = 33.3 dBm and data stream launched (a) 23 ps before bit center time (b) 23 ps after bit center time. The shifting of the peaks of the data pulses toward bit center time is visible.

The important departure in the enhanced scheme is the drop in BER as the offset is increased as compared to a corresponding monotonic increase in BER in the experiment. This, too, can be attributed to the presence of the periodic clock pulses. Soliton pairs in anti-phase launched with small input separations (large offset from bit center time) experience strong repulsion (Fig. 5.7 (a)). Periodic clock pulses in the enhanced setup limit this strong repulsion as every data pulse experiences the repulsion of both clock pulses, shifting the data pulse towards its bit center time and resulting in low BER. The absence of periodic clock pulses in the experiment causes data pulses with large delayed offsets from bit center time to repel strongly away from their accompanying clock pulse, moving further away from the bit center time, thus resulting in high BER.

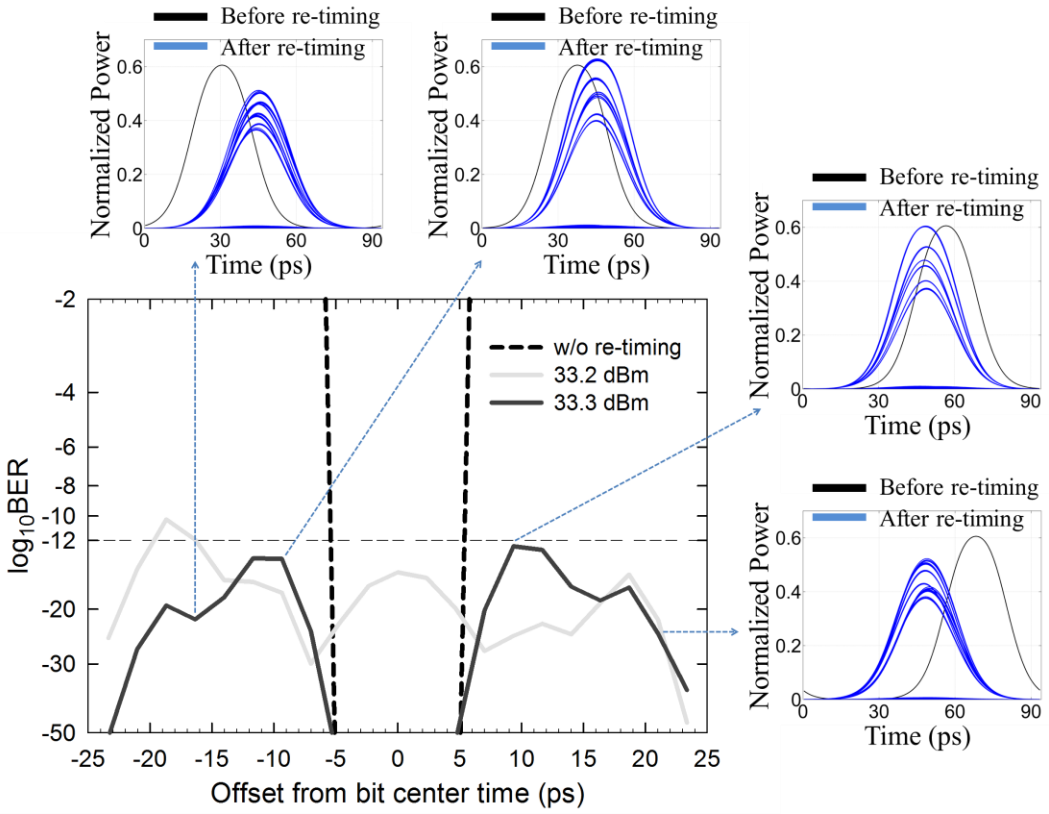

Fig. 5.10 BER performance of the enhanced re-timing scheme, 33.3 dBm peak pulse power gives the best re-timing performance. Insets show electrical domain eye diagrams after the de-interleaver using a 20 GHz bandwidth photo-detector model.

5.6 Energy efficiency of the soliton molecule based re-timing system

Using equipment datasheets when available, I determined the power consumption of the soliton molecule based re-timing system as shown in Table 5.2.

Component	Power consumption (W)
Optical pulse source (mode-locked laser + RF driver)	10
EDFA before Michelson interferometer	10
EDFA before fiber span	15
De-interleaver	4.9
EDFA after de-interleaver	5
System Total	**44.9**

Table 5.2 Soliton molecule based re-timing system power consumption

Energy/bit = System total power / bit-rate for the soliton molecule re-timing system

= 44.9 W / 10.7 Gbps

= 4.196 nJ/bit

Bits/Joule = 238.307 Mb/J

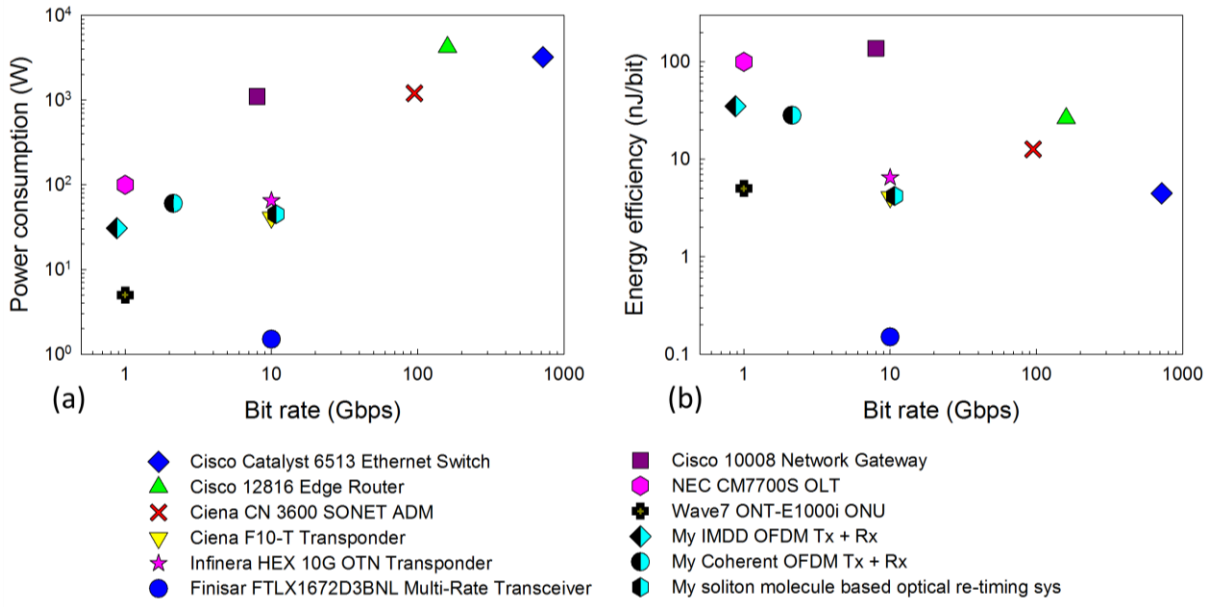

Fig. 5.11 The power consumption (a) and energy efficiency (b) of commercially available networking equipment and my soliton molecule based optical re-timing system, my OFDM systems (IMDD and coherent) are also shown for comparison; a lower energy efficiency number (in nJ/bit) is better.

With the power consumption and energy efficiency (energy/bit) as calculated above, we can compare the performance of the soliton molecule re-timing system with commercially available networking equipment as shown in Fig. 5.11. Optical transponders, such as the Ciena F10-T and the Infinera HEX 10G OTN, are good examples of signal regenerators as they essentially perform all the three regeneration functions of re-amplification, re-shaping and re-timing during optical transport protocol conversion in the transponder. In Fig. 5.11, we can see that the soliton molecule based re-timing system studied in this chapter has a power consumption and energy efficiency that is comparable to that of the 2 transponders mentioned above. It should however be noted that the power consumption of the transponders mentioned will rise with bit-rate due to the O-E-O process used in the transponder, as faster electronic hardware is more power hungry. On the other hand, the power consumption in an optical re-timing system, such as the one studied in this chapter, is essentially bit-rate independent. This enables optical re-timing to be more energy efficient compared to O-E-O based re-timing for higher bit rates.

5.7 Conclusions

I have experimentally demonstrated the ability of the soliton molecule effect to re-time an out of synchronization data stream at 10.7 Gb/s. Data pulses offset up to 16 ps from bit center are re-timed successfully. The results of numerical simulations closely match those of the experiment. An enhanced version of the scheme that uses an additional clock pulse for every data pulse was simulated and shown to re-time data pulses offset up to 23 ps from bit center, resulting in superior performance as compared to the experimental scheme. It is important to note that the use of newer techniques such as transmitter side pre-compensation and receiver side post-compensation using coherent detection and digital signal processing (DSP) have in many ways solved the problem of re-shaping and re-timing. The development of high speed DSP application specific integrated circuits (ASICs) has helped drive down the cost of processing in the electrical domain. However, optical signal regeneration may still play an important role by providing a toolbox of optical methods that can be used in specific applications where the cost of DSP is prohibitive and in applications such as the development of the all-optical router for core and edge networks.

Conclusions and future work

In this dissertation, I have presented OFDM implementations for both direct and coherent detection. In the direct detection OFDM implementation in Chapter 2, I, in association with my colleagues, demonstrated elastic networking with OFDM that can be useful in next generation access networks [88]. I have presented a real-time FPGA based implementation of a complete OFDM (Tx and Rx) system that carries examples of real-world traffic – HD video and text. This real-time implementation would be a useful tool to study OFDM transmission in larger networking experiments and could serve as a starting point for commercialization of fiber-optic links for access and metro applications.

In Chapter 3, I presented and experimentally verified the concept of a unified transmitter that can service both direct and coherent receivers [89, 90]. This concept could help with more efficient provisioning of capex as bit rate and cost can be traded against one another. The unified transmitter approach also enables the network to be scaled up to meet future traffic demand by replacing direct receivers with coherent receivers. I have also experimentally demonstrated the resilience of the pol-mux transmission scheme to nonlinear effects in fiber as compared to the conventional IMDD-OFDM scheme. Conventional IMDD-OFDM also suffers from dispersion fading while the pol-mux transmission for the direct receiver is single sideband, and hence does not suffer from dispersion fading. Hence, the pol-mux transmission is a more suitable candidate for long haul OFDM transmission.

I have also presented two polarization analyzer based receivers to receive pol-mux single sideband OFDM signals in Chapter 3. I have compared the performance of these two receivers with one another and shown that the dual analyzer balanced detector has superior performance as compared to the single analyzer detector. The dual analyzer balanced detector was studied using numerical simulation. A future extension of this work could be to build this receiver as a photonic integrated circuit (PIC). A PIC implementation is called for as the optical path lengths

for the light from the optical splitter to the two polarization analyzers must be equal and these paths must not suffer from excessive time-varying birefringence.

In Chapter 4, I have presented an OFDM pilot-tone based distributed control scheme. My colleagues and I verified this control scheme for a simple optical network carrying 3 optical wavelengths and showed that the distributed control scheme has a lower latency compared to centralized control [91]. This pilot-tone based control scheme uses the lowest frequency OFDM subcarrier defined for our system and hence does not need additional hardware to add the pilot-tone in the electrical or optical domain as is the convention. This work demonstrates that OFDM has the inherent capability to work with low frequency (a fraction of the full OFDM bandwidth) and hence low cost photodiodes for pilot-tone extraction and distributed control.

In Chapter 5, I presented and experimentally verified an optical retiming scheme utilizing the property of soliton pairs to maintain a fixed temporal separation when launched at a specific optical power into a dispersion alternating fiber span [92, 93]. The appeal of all-optical processing in general is that it is free from the severe bandwidth bottleneck in the electrical domain – which has been the traditional domain for signal processing. As I have covered both electronic processing (Chapter 2 and 3) and optical processing (Chapter 5) in this dissertation, I have also presented the comparison of the energy efficiency estimates for these processing schemes. While the availability of highly optimized and faster application specific integrated circuits (ASICs) and faster DACs and ADCs may have swung the pendulum back in favor of electronic processing, optical processing may yet have a role to play in applications such as wavelength conversion.

OFDM for optical networking demands substantial processing hardware at the transmitter and receiver. Attempts to commercialize OFDM will have to first address this hardware problem. A logical step would be the development of OFDM ASICs with at-least a 100 Gb/s throughput. The FPGA based OFDM implementation developed for research presented in this dissertation can be scaled up and optimized further to serve as a blueprint for a commercial OFDM ASIC.

Appendix

OFDM frame synchronization for coherent and direct detection optical fiber telecommunication

A.1 Introduction

Orthogonal frequency division multiplexing (OFDM) is a promising candidate for next generation elastic optical networks due to its inherent ability to support multiple users, its capability to adapt to channel frequency response and its dispersion tolerance. One of the important operations of OFDM reception is frame synchronization.

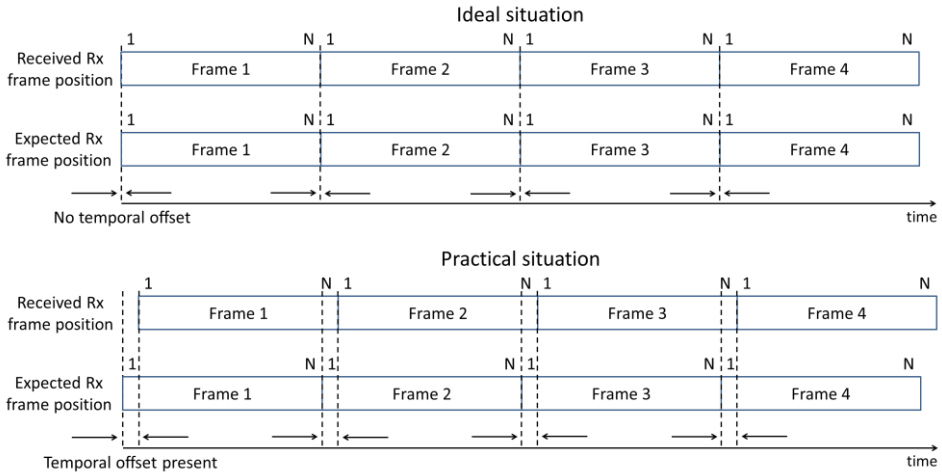

Fig. A.1 The upper figure shows the ideal situation with the received IFFT frames arriving at the expected time. The lower figure shows a more practical situation with the frames arriving after their expected time.

Fig. A.1 depicts the problem OFDM reception faces. OFDM relies on modulating a large number of low bandwidth subcarriers (SCs) with data using an Inverse Fast Fourier Transform

(IFFT) operation at the transmitter. The receiver uses the Fast Fourier Transform (FFT) operation to demodulate the data. OFDM data is transmitted as a series of IFFT frames – each IFFT frame consisting of data from one IFFT operation. At the receiver, it is necessary that only the data from one IFFT frame be used as input to the corresponding FFT operation. This ideal situation is shown in the upper portion of Fig. A.1. Practically however, there is a random temporal offset between the received IFFT frames and their expected position as depicted in the lower half of Fig. A.1. In fiber telecom, this random temporal offset is a result of the thermal expansion and contraction of the fiber over its entire length. This results in data from one IFFT frame being part of the computation of the FFT of the subsequent IFFT frame which causes errors in the demodulated data after FFT [94]. Hence, frame synchronization in OFDM is an important problem.

Several methods have been proposed and demonstrated to solve the frame synchronization problem. The first group of methods is based on transmitting a predefined pattern (also called training symbols or a training sequence) and determining the temporal offset by calculating the correlation between the training symbols using iterative temporal sliding. Particular implementations of this method [95, 96] require a large number of samples per training symbol (~512) and are not suitable for fiber optic OFDM communication where the requirement for Gb/s bit rates and the availability of GSa/s sampling rates do not allow for a large number of samples per symbol. Other implementations of this method rely on cross-correlating the received predefined pattern with a stored version of the predefined pattern at the receiver [97, 98]. Frequency domain auto-correlation has also been proposed [99]. The disadvantages of this group of methods are: (a) the need for hardware multipliers to calculate correlation, this calls for more complex digital hardware; (b) iteratively calculating the temporal offset is time consuming. A maximum-likelihood (ML) based method that uses the cyclic prefix has been proposed [100], this method requires hardware multipliers to calculate the ML estimate. The method proposed in [101] relies on transmitting the training symbols using differential-binary phase shift keying (D-BPSK) and demodulating the training symbols at the receiver using a D-BPSK demodulator and then comparing the training symbols to each other to determine the temporal offset. Here, the use of D-BPSK allows the synchronization process to be robust against the inherent random phase variations between the received signal and the carrier/local oscillator which corrupts the training symbols in the time domain. However, this also complicates the synchronization hardware due to

the need for a D-BPSK demodulator. A virtual subcarrier based method [102] has been proposed, this method requires hardware multipliers and therefore more complex synchronization circuitry.

Our method of frame synchronization has the advantage of speed and simplicity in hardware implementation. It is ideally suited for self-coherent OFDM reception over optical fiber and requires only 1 sample per symbol for correct operation. The method is robust against the inherent random phase variations between the received signal and the carrier/local oscillator. It takes just 4 clock cycles of computation time to achieve frame synchronization in our implementation. The method employs digital comparators and does not require hardware multiplication and iterative temporal sliding operations, simplifying the digital circuitry. This allows for the frame synchronization method to be implemented in a simple and cost-effective manner.

A.2 Principle of operation

I begin by describing the temporal structure of the OFDM frame in our example implementation. I use a 512 point IFFT and with the digital to analog converters (DACs) at the transmitter and the

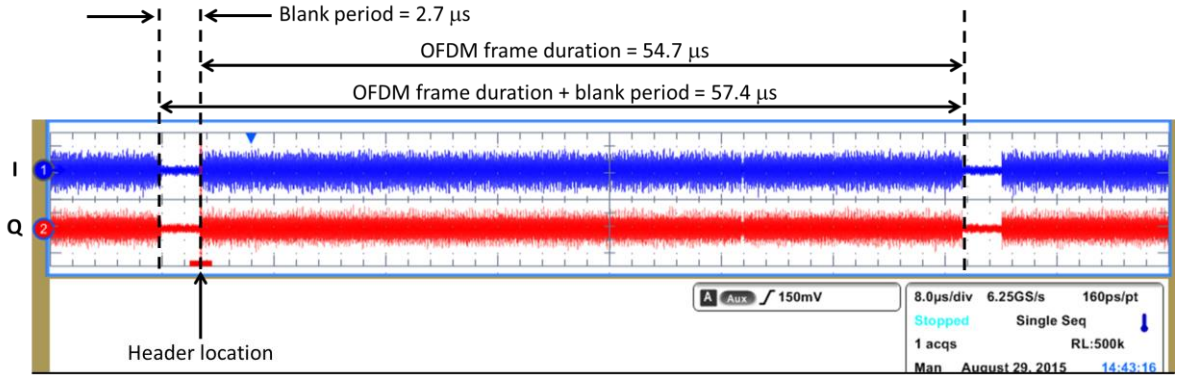

Fig. A.2 The temporal structure of the OFDM frame. The horizontal scale is 8 µs/div.

analog to digital converters (ADCs) at the receiver running at 2 GSa/s, one IFFT frame is 256 ns in duration. We transmit 214 such IFFT frames to form one OFDM frame 54.7 µs in duration, as shown in Fig. A.2. This is followed by a blank period of 2.7 µs. The OFDM frame and blank period combination is repeated every 57.4 µs.

Every OFDM frame begins with a single pulse – the header, as shown in Fig. A.3. The header is placed on both the in-phase (I) and the quadrature (Q) outputs of the complex OFDM signal.

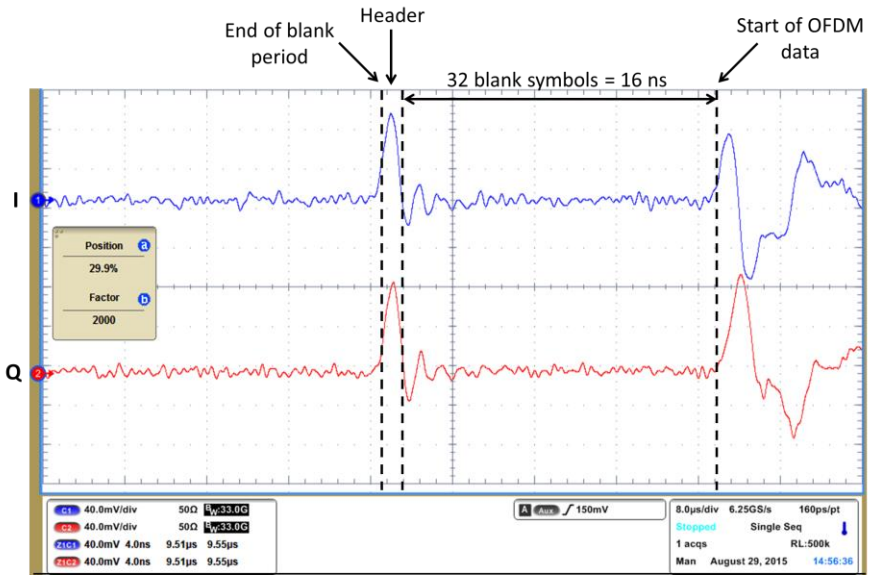

Fig. A.3 The timing in the vicinity of the header. The horizontal scale is 4 ns/div.

This is followed by a blank period of 16 ns. The OFDM data commences at the end of the blank period.

Our method of frame synchronization relies on the detection of the header on either the I or the Q inputs of the receiver. Since coherent detection is employed, the inherent random phase drift between the carrier/local oscillator and the signal causes the amplitude of the headers on the I and Q inputs to wax and wane in a complementary manner. This can be seen in Fig. A.4 where 8 representative phase positions of the header in the complex plane and the corresponding time domain I and Q waveforms are shown. The receiver hardware employs digital comparator circuits with 4 configurable threshold levels – the upper_threshold2 and the lower_threshold2 are symmetric about the zero amplitude of the I and Q inputs and are set lower i.e. closer to the zero amplitude to enable detection of the start of the OFDM frame. The upper_threshold and the lower_threshold are also symmetric about the zero amplitude of the I and Q inputs and are set higher i.e. further away from the zero amplitude to enable setting of the data shifting logic in a predictable manner. The important point to note in Fig. A.4 is that irrespective of the received phase position of the header, the header component in either the I or the Q input will always breach upper_threshold2 or lower_threshold2. Hence, we have a method to determine the start of the OFDM frame irrespective of the instantaneous phase of the carrier/local oscillator.

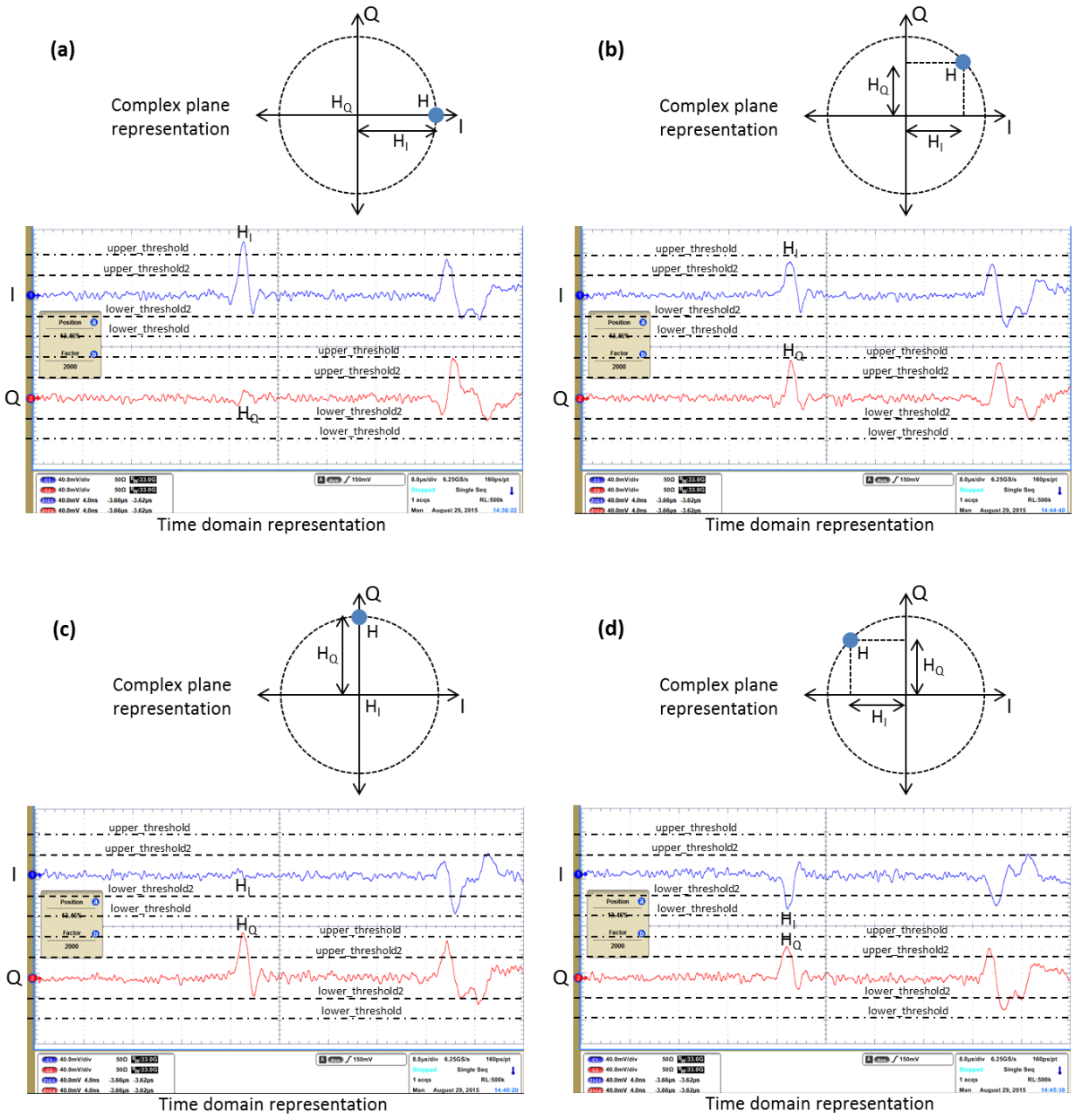

Fig. A.4-Part I The header sampled at 4 representative phase positions. The horizontal scale is 4 ns/div.

It is important to note that our method of frame synchronization provides OFDM symbol level synchronization accuracy. In order to achieve sub-symbol level synchronization accuracy, frequency domain training symbols/pilots can be transmitted every OFDM frame and can be used at the receiver to compensate for sub-symbol temporal offset. These pilot frequencies can also be used to compensate for the dispersion in optical fiber and can therefore be implemented

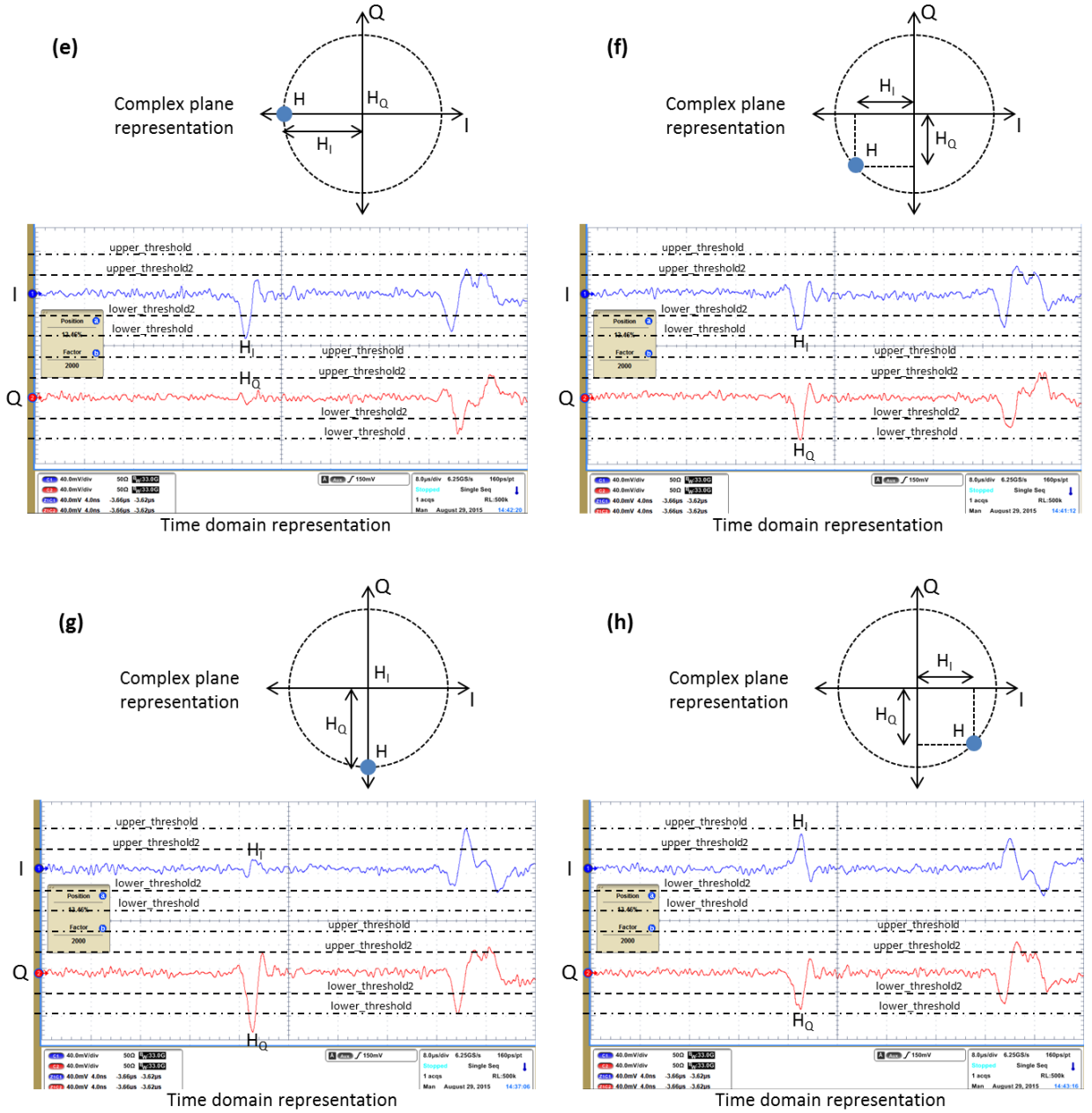

Fig. A.4-Part II The header sampled at 4 additional representative phase positions. The horizontal scale is 4 ns/div.

most efficiently after the FFT operation. For this reason, I do not include sub-symbol level synchronization in our proposed method of synchronization.

A.3 Hardware implementation

The proposed method has been implemented on a BEE3 Virtex 5 Field Programmable gate Array (FPGA) board. This board has 2 ADCs running at 2 GSa/s each, and each connected to 2 FPGAs clocked at 250 MHz. Data from the ADC 1 connected to the I input enters the main data processing FPGA. Data from the ADC 2 connected to the Q input is routed via its FPGA to the

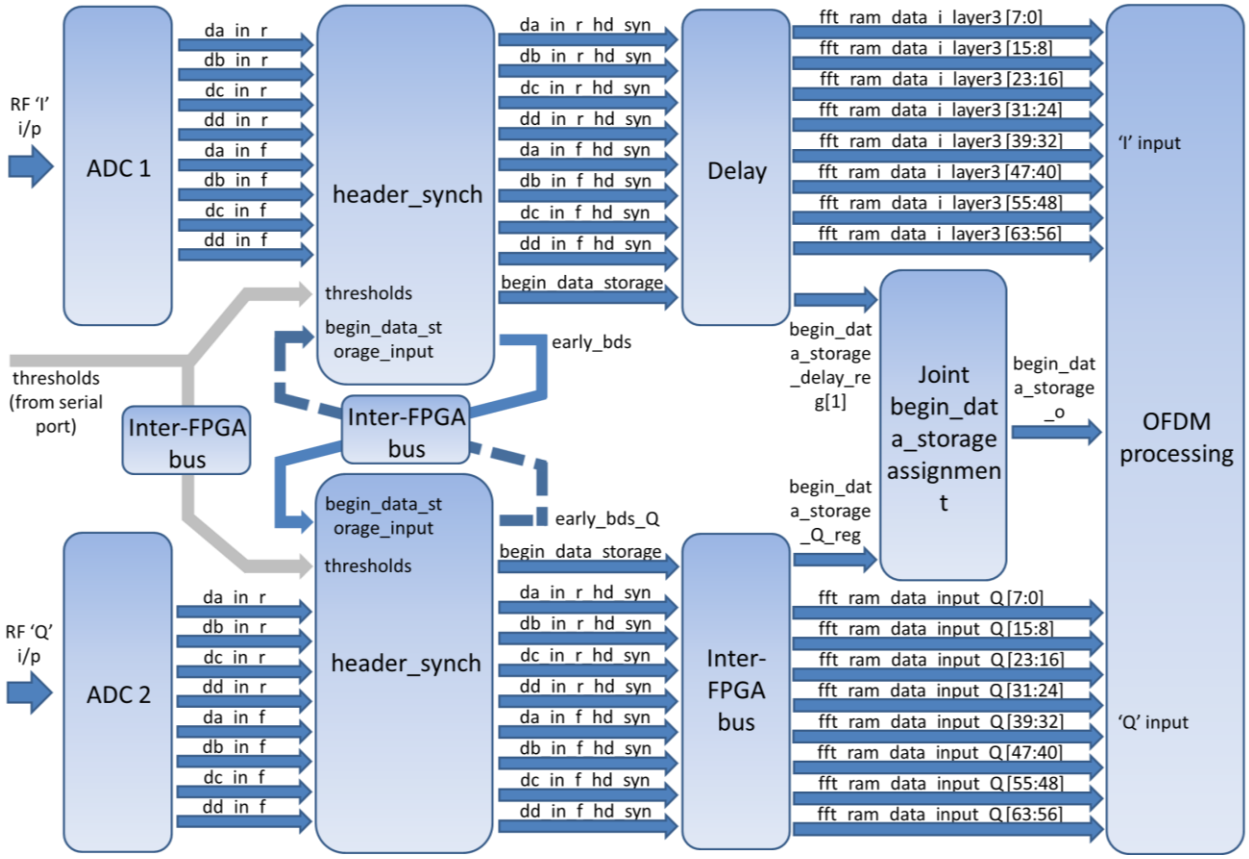

Fig. A.5 The top level block diagram of the frame synchronization circuit.

main data processing FPGA using an inter-FPGA communication bus, as shown in Fig. A.5. The 4 threshold levels are set using serial port based commands from the user and both FPGAs use the same threshold values.

Data output from each ADC consists of 8 lines in chronological order of sampling at the ADC, each consisting of 8 bits and updated every 4 ns (explained further in Fig. A.8). da_in_r represents the earliest sample in each 4 ns period while dd_in_f represents the latest sample in each 4 ns period.

The header_synch block is implemented immediately after the ADC in each FPGA i.e. for each of the I and Q inputs. The two tiered threshold levels enable us to divide the frame synchronization method into a coarse acquisition step and a fine acquisition step. As mentioned in the previous section, upper_threshold2 and lower_threshold2 are set lower i.e. closer to the zero level of the I and Q inputs to guarantee that begin_data_storage from either the I or the Q header_synch blocks will be set to 1 when a new OFDM frame arrives. This is the coarse acquisition step and will occur at the start of every OFDM frame. The fine acquisition step occurs whenever the header breaches upper_threshold or lower_threshold for either I or Q inputs which enables the header_synch block to shift data individually for the I and the Q inputs based on the temporal position of the received header. As can be seen from Fig. A.4, the header may not breach upper_threshold or lower_threshold for either I or Q inputs at the start of every OFDM frame and in this case the previous shifting position is held.

The inter-FPGA bus has a propagation delay of 3 clock cycles of the 250 MHz clock i.e. 12 ns. This causes the data (fft_ram_data_input_Q) and begin_data_storage_Q_reg signal for the Q input to arrive delayed by 3 clock cycles into the main data processing FPGA. Hence, in order to ensure the co-incidence of data and signals for I and Q in the main data processing FPGA, the data (da_in_r_hd_syn to dd_in_f_hd_syn) and the begin_data_storage signal for the I input are delayed by 3 clock cycles in the Delay block as shown in Fig. A.5.

The early_bds and early_bds_Q signals from the I and Q input header_synch blocks respectively are used to indicate to the Q and I header_synch blocks that a header was received and that all further activity in the header_synch block that did not receive the header must be suspended for the duration of the OFDM frame. This ensures that OFDM data in the OFDM frame is not misinterpreted as a header. Since early_bds and the early_bds_Q use the same inter-FPGA bus with a 3 clock cycle i.e. 12 ns propagation delay, I added a blank period of 16 ns after the header position as shown in Fig. A.3. This ensures that the early_bds and the early_bds_Q signals arrive at the destination header_synch blocks before the OFDM data can be misinterpreted as a header and can corrupt the synchronization process.

The Joint begin_data_storage assignment block consists of the following ‘OR’ operation:

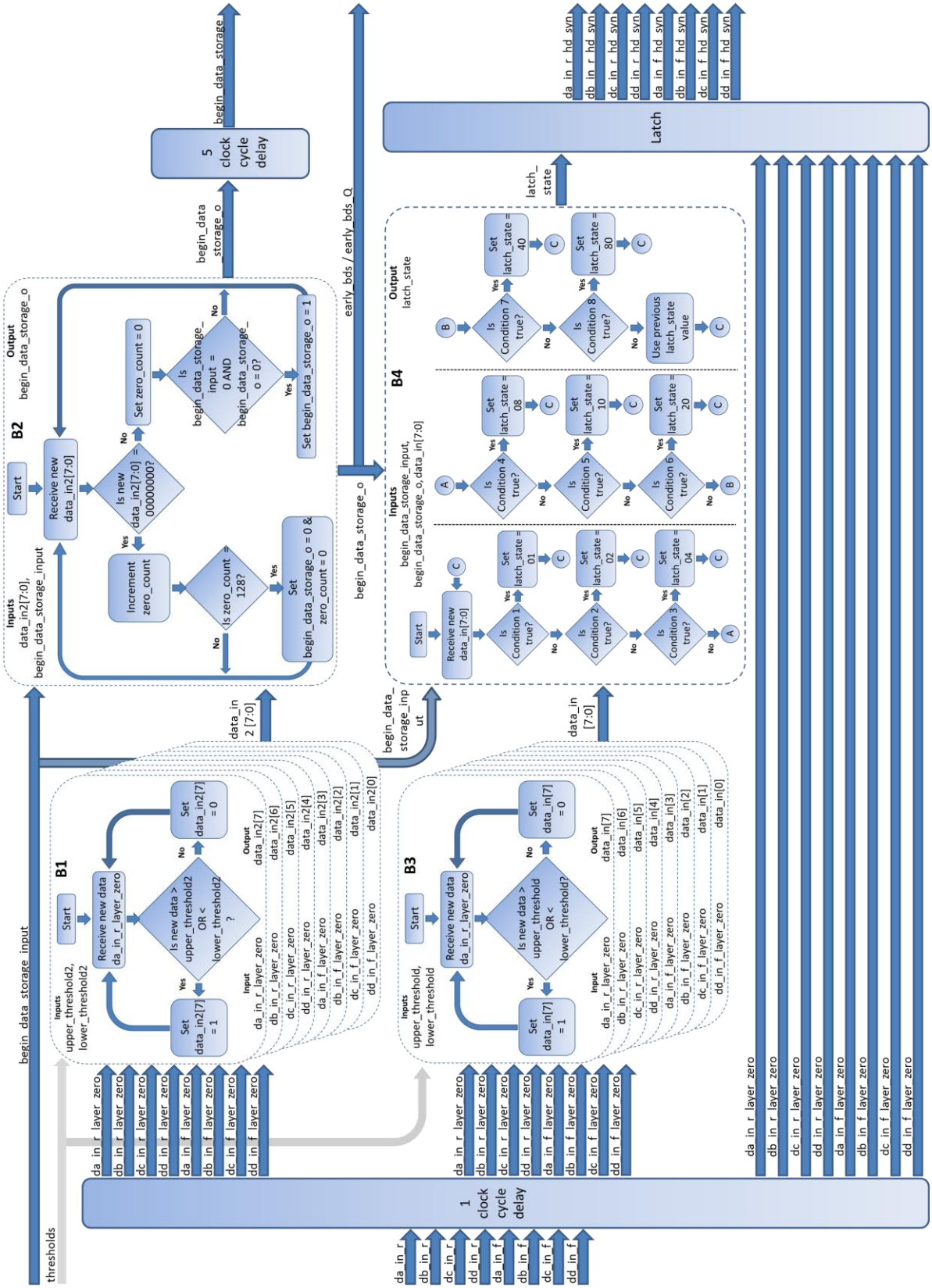

Fig. A.6 The internal block diagram of the header_synch block.

begin_data_storage_o = begin_data_storage_delay_reg[1] OR begin_data_storage_Q_reg

Thus, the begin_data_storage_o signal, which indicates the start of valid data to the OFDM processing block, will be set to 1 whenever I or the Q header or both are detected.

Fig. A.6 shows the internal block diagram of the header_synch block. There are 4 main processing blocks in the header_synch block:

1. B1: Using digital comparators, this block determines if the incoming data has breached upper_threshold2 or lower_threshold2. If so, the data_in2 bit of the corresponding data line is set to 1. This process is repeated every 4 ns.
2. B2: This block sets the begin_data_storage_o signal to 0 if all bits of data_in2 are 0 at least 128 times. This indicates that there are 128x8 = 1024 blank symbols transmitted and is used to determine the blank period that follows each OFDM frame. The first instance any bit of data_in2 is found to be 1 (which indicates a header was found) following the blank period is used to set begin_data_storage_o to 1. The begin_data_storage_input (early_bds/early_bds_Q) signal coming from the other FPGA is also checked for 0 level so as to ensure that the begin_data_storage_o is not set to 1 incorrectly by OFDM data if the other input (I or Q) has already detected a header. The begin_data_storage_o signal is delayed for five 250 MHz clock cycles so that the setting of begin_data_storage to 1 coincides with valid data on the Latch block data output lines (da_in_r_hd_syn to dd_in_f_hd_syn).
3. B3: Using digital comparators, this block determines if the incoming data has breached upper_threshold or lower_threshold. If so, the data_in bit of the corresponding data line is set to 1. This process is repeated every 4 ns. The position of 1 in data_in determines the position of the header. For example, 00100000 for data_in indicates that the header was found in the 3rd data symbol in that particular 4 ns period. This case is depicted in Fig. A.8.
4. B4: This block sets the shifting position for the incoming data i.e. the latch_state based on the received position of the header as indicated by data_in. The conditions checked in the flowchart are as follows:
   a. Condition 1: begin_data_storage_input = 0 AND begin_data_storage_o = 0 AND data_in[7] = 1

b. Condition 2: begin_data_storage_input = 0 AND begin_data_storage_o = 0 AND data_in[7] = 0 AND data_in[6] = 1

c. Condition 3: begin_data_storage_input = 0 AND begin_data_storage_o = 0 AND data_in[7] = 0 AND data_in[6] = 0 AND data_in[5] = 1

d. Condition 4: begin_data_storage_input = 0 AND begin_data_storage_o = 0 AND data_in[7] = 0 AND data_in[6] = 0 AND data_in[5] = 0 AND data_in[4] = 1

e. Condition 5: begin_data_storage_input = 0 AND begin_data_storage_o = 0 AND data_in[7] = 0 AND data_in[6] = 0 AND data_in[5] = 0 AND data_in[4] = 0 AND

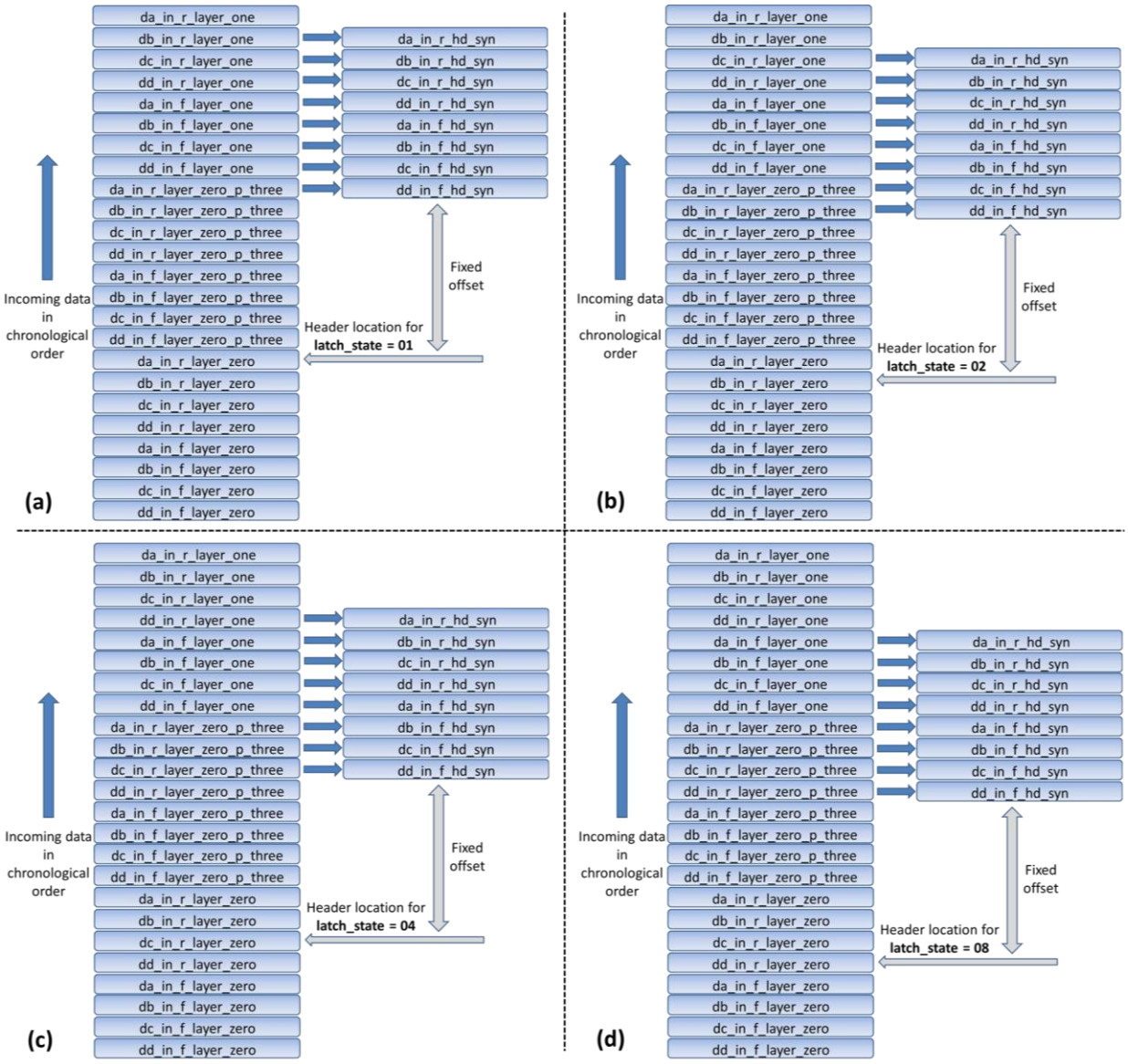

Fig. A.7-Part I The Latch block in the first 4 of the 8 possible latch_state conditions.

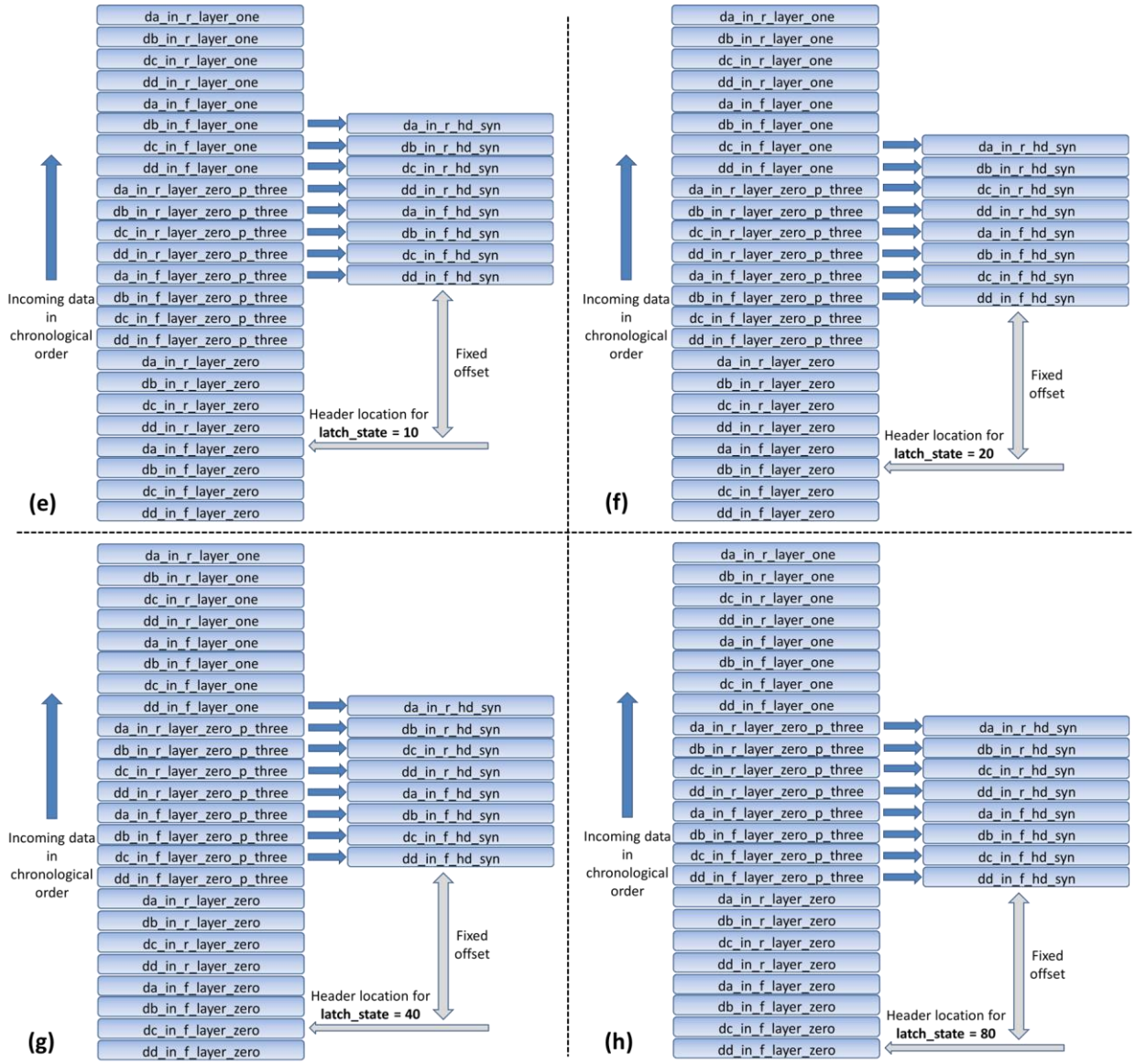

Fig. A.7-Part II The Latch block in the next 4 of the 8 possible latch_state conditions.

data_in[3] = 1

f. Condition 6: begin_data_storage_input = 0 AND begin_data_storage_o = 0 AND data_in[7] = 0 AND data_in[6] = 0 AND data_in[5] = 0 AND data_in[4] = 0 AND data_in[3] = 0 AND data_in[2] = 1

g. Condition 7: begin_data_storage_input = 0 AND begin_data_storage_o = 0 AND data_in[7] = 0 AND data_in[6] = 0 AND data_in[5] = 0 AND data_in[4] = 0 AND data_in[3] = 0 AND data_in[2] = 0 AND data_in[1] = 1

h. Condition 8: begin_data_storage_input = 0 AND begin_data_storage_o = 0 AND data_in[7] = 0 AND data_in[6] = 0 AND data_in[5] = 0 AND data_in[4] = 0 AND data_in[3] = 0 AND data_in[2] = 0 AND data_in[1] = 0 AND data_in[0] = 1

The Latch block is implemented as shown in Fig. A.7. The value of latch_state from block B4 determines the set of data that will be selected so as to eliminate the effect of temporal offset of the received data. This can be understood further in Fig. A.8, which depicts the variation of all important signals in the header_synch block over time.

In Fig. A.8, the 3rd ADC sample contains the header followed by 32 zero samples as shown in Fig. A.3. The next sample is the 1st OFDM data sample which has a temporal offset i.e. analog offset of 3 sample positions. This translates to a digital offset on the da_in_r to dd_in_f data lines. The scenario depicted in Fig. A.8 is that of the header breaching both thresholds i.e. upper_threshold/lower_threshold and upper_threshold2/lower_threshold2. Thus, 2 clock cycles after the appearance of the header on the da_in_r to dd_in_f data lines, data_in and data_in2 each have a non-zero bit. In the next clock cycle, begin_data_storage_o is set to 1 and latch_state is set to its new value of 04. From the next clock cycle onwards, the Latch outputs da_in_r_hd_syn to dd_in_f_hd_syn carry the correct shifted data with the digital offset eliminated. This is most visible with the data corresponding to the 1st OFDM sample – D1_binary appearing on the da_in_r_hd_syn data line. Thus, from the time the header appears on the da_in_r to dd_in_f data lines, it takes the header_synch circuit just 4 clock cycles i.e. 16 ns to determine the header's new temporal offset, configure the Latch and to output the correct shifted data with no digital offset on the Latch output lines. The signal begin_data_storage, which is a 5 clock cycle delayed version of begin_data_storage_o, is set to 1 at the same time valid data appears on the latch output lines (da_in_r_hd_syn to dd_in_f_hd_syn).

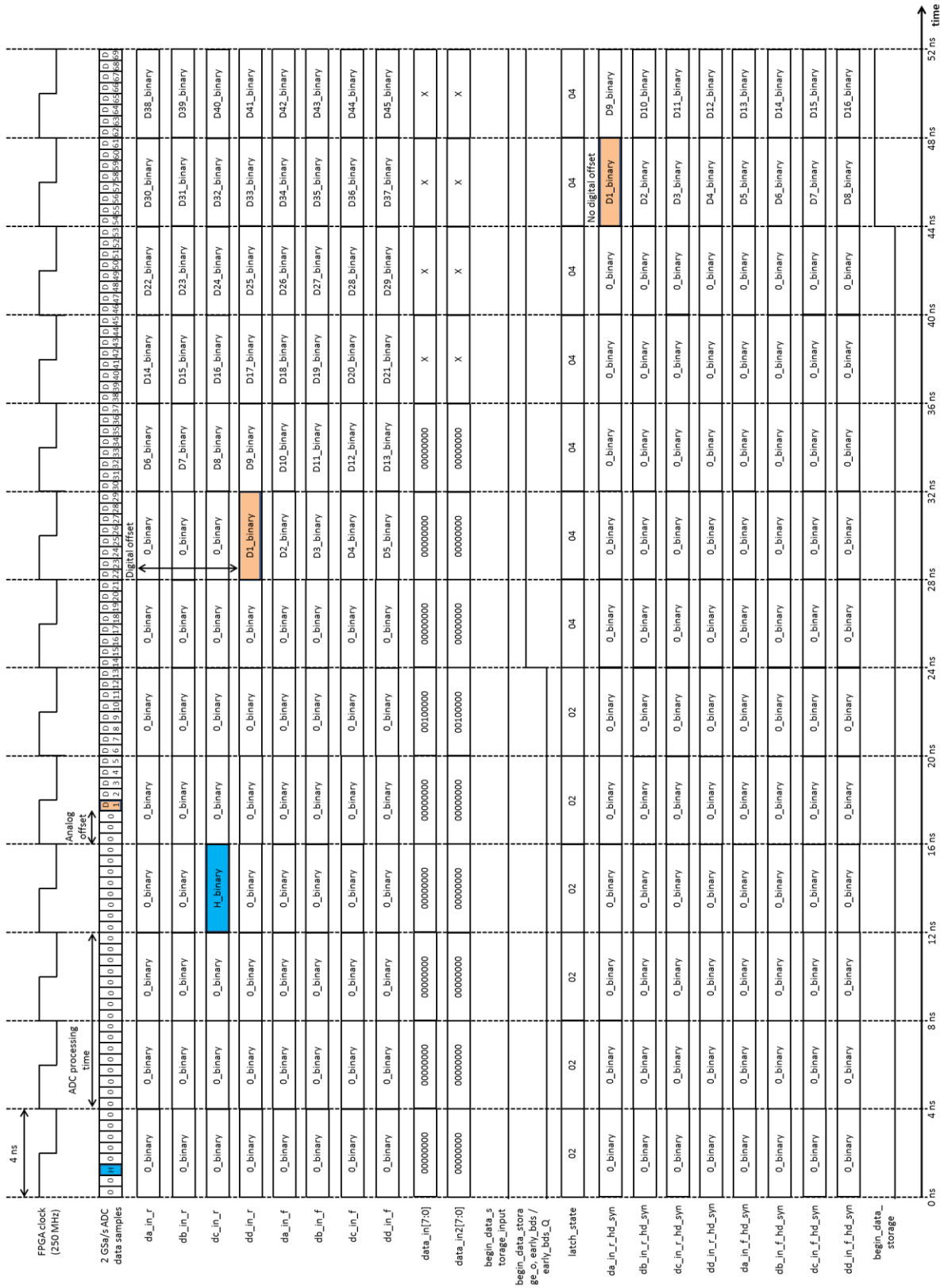

Fig. A.8 The timing diagram of the header_synch block. 'X' indicates a don't care value.

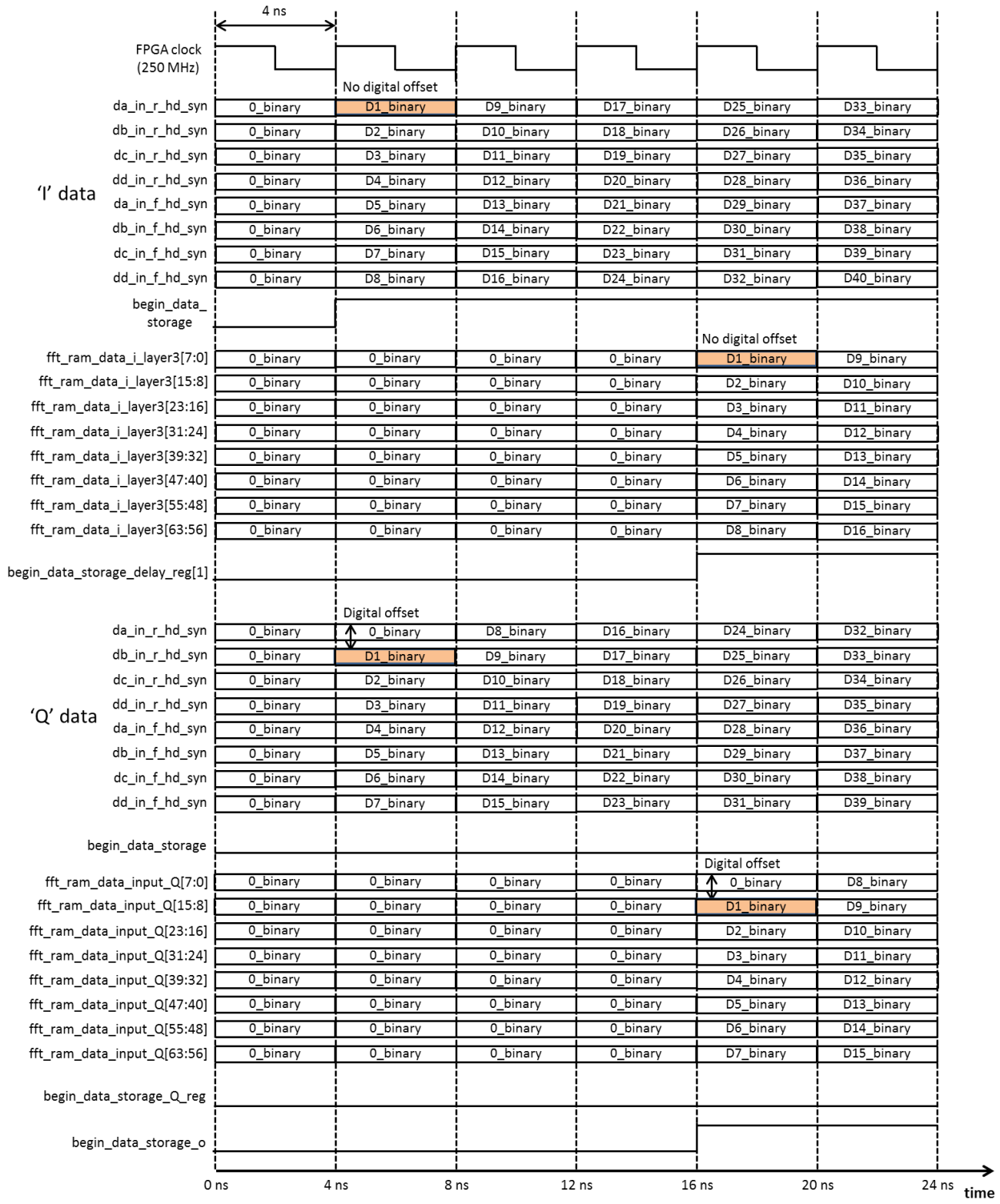

Fig. A.9 The timing diagram for the top level frame synchronization circuit.

Fig. A.9 shows the timing diagram of the top level frame synchronization circuit. The scenario depicted is that of the header on the I input being present while the header on the Q

input being absent as represented in Fig. A.4 (a). Thus, we have the begin_data_storage signal of the I input being set to 1 when valid data appears on the da_in_r_hd_syn to dd_in_f_hd_syn I data lines. Also, the begin_data_storage signal of the Q input is not set to 1 when valid data appears on the da_in_r_hd_syn to dd_in_f_hd_syn Q data lines, as no header was found for the Q input. This also means that the Q input has a digital offset as the header position could not be determined for this particular OFDM frame. Experimental observations for self-coherent OFDM detection show that the complementary waxing and waning of the I and Q headers (as shown in (a)-(h) of Fig. A.4) usually occurs tens of times per second. Thus, the Q input will detect a header and hence the new header position to eliminate the digital offset in the order of tens of milliseconds. This time period can be compared to the time it takes for the fiber delay and hence the header position/offset to change, which is usually in the order of tens of seconds. Thus, even though the circuitry (for I or Q input) may fail to detect a header to correct for digital offset for every OFDM frame, the digital offset (if and when present) is corrected about 3 orders of magnitude faster than the time it takes for the temporal offset to change to a new value. The inability of the circuitry to detect a header to correct for digital offset is a direct outcome of using higher thresholds (upper_threshold/lower_threshold) which the header is unable to breach in every OFDM frame. As the OFDM I and Q waveforms suffer from random small amplitude fluctuations, the higher thresholds are required to eliminate the possibility of detecting a false header position.

Lower thresholds (upper_threshold2/lower_threshold2) are used to detect the start of the OFDM frame and set the begin_data_storage signal to 1. These lower thresholds guarantee that the header for the I or Q input will breach them every OFDM frame. In the scenario in Fig. A.9, the I input header is detected and hence the signal begin_data_storage_delay_reg[1] which is a 3 cycle delayed version of the begin_data_storage signal for the I input, is set to 1 when valid data appears on the fft_ram_data_i_layer3 lines. Because the Q input header is not detected, the signal begin_data_storage_Q_reg which is a 3 cycle delayed version of the begin_data_storage signal for the Q input, stays at 0 level even when valid data appears on the fft_ram_data_input_Q lines. The OR operation on begin_data_storage_delay_reg[1] and begin_data_storage_Q_reg ensures that begin_data_storage_o is set to 1 when valid data appears on the fft_ram_data_i_layer3 and fft_ram_data_input_Q lines. The OFDM processing block will thus begin data processing even when the I input header alone has been detected in this case.

A.4 Hardware implementation for direct detection OFDM

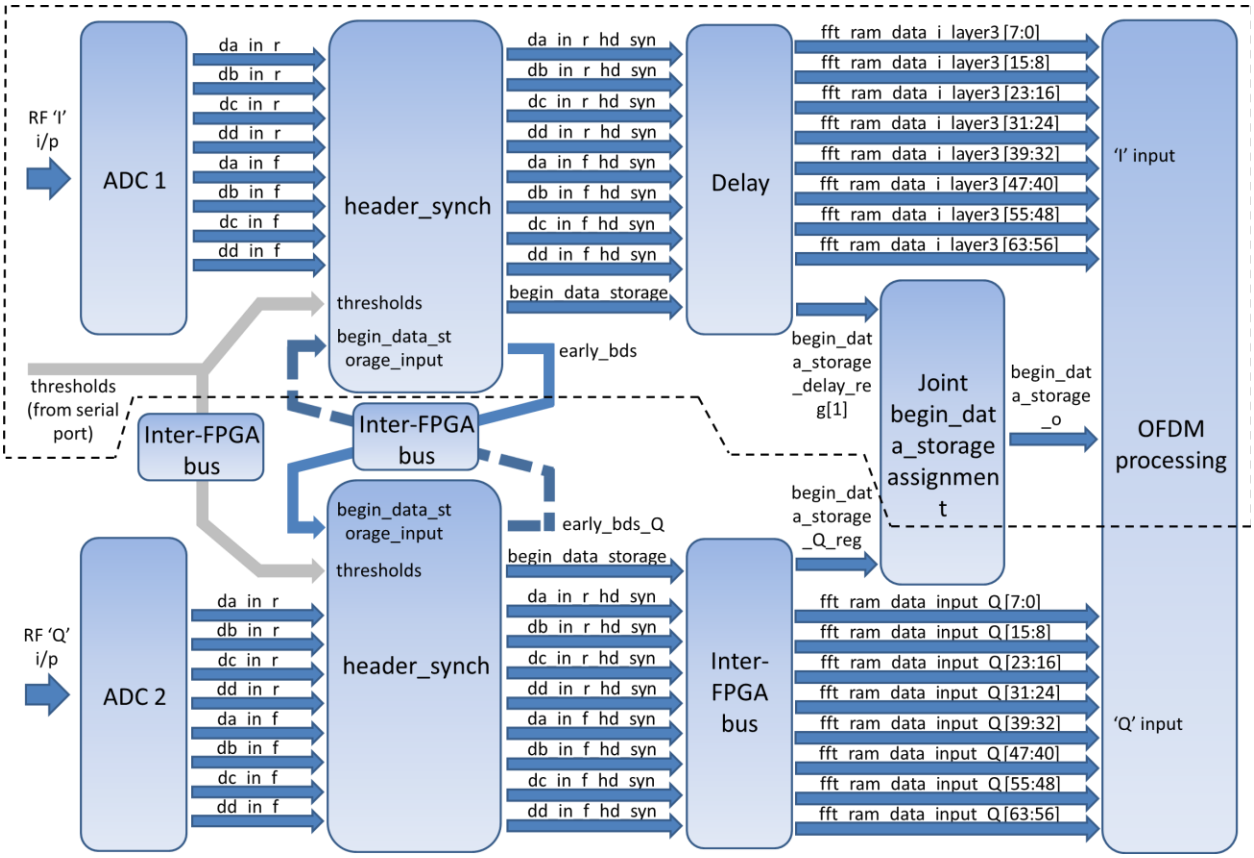

Fig. A.10 The top level block diagram of the frame synchronization circuit for direct detection OFDM.

The implementation of the frame synchronization circuitry for direct detection OFDM can be considered to be a subset of the coherent OFDM implementation discussed above. This is due to the fact that direct detection OFDM consists of just one input and hence can be connected to the I input of the coherent OFDM implementation. It is also important to note that the header for direct detection OFDM does not wax and wane like its coherent counterpart. This is because direct detection does not rely on interference with a local oscillator/carrier at the receiver and hence does not suffer from the effects of random phase variation between the local oscillator/carrier and the received signal. This means that the header on the single input is guaranteed to breach the lower thresholds (upper_threshold2/lower_threshold2) in every OFDM frame. In Fig. A.10, only the circuitry within the dashed boundary is necessary for frame synchronization in direct detection OFDM. Unused outputs such as thresholds and early_bds can be left unconnected while unused inputs such as begin_data_storage_input,

begin_data_storage_Q_reg and the fft_ram_data_input_Q lines must be connected to zero level to ensure predictable circuit operation.

References

[1] A.G. Bell, "Apparatus for signaling and communicating, called Photophone," US patent no. 235199, Dec. 1880.

[2] J. Hecht, *City of Light: The Story of Fiber Optics*, Oxford University Press, 2004.

[3] Cisco Visual Networking Index: Forecast and Methodology, 2014-2019 White Paper, http://www.cisco.com/c/en/us/solutions/collateral/service-provider/ip-ngn-ip-next-generation-network/white_paper_c11-481360.pdf

[4] Cisco Global Cloud Index: Forecast and Methodology, 2014–2019 White Paper, http://www.cisco.com/c/en/us/solutions/collateral/service-provider/global-cloud-index-gci/Cloud_Index_White_Paper.pdf

[5] H. Sun, K. Wu, and K. Roberts, "Real-time measurements of a 40 Gb/s coherent system," Optics Express, vol. 16, no. 2, pp. 873-879, 2008.

[6] V. Herath, R. Peveling, T. Pfau, O. Adamczyk, S. Hoffmann, C. Wördehoff, M. Porrmann, and R. Noé, "Chipset for a Coherent Polarization-Multiplexed QPSK Receiver," Proc. OFC/NFOEC, paper OThE2, 2009.

[7] C. Rasmussen, Y. Pan, M. Aydinlik, M. Crowley, J. C. Geyer, P. Humblet, F. Liu, B. Mikkelsen, P. Monsen, N. Nadarajah, G. Pendock, and B. Shah, "Real-time DSP for 100+ Gb/s," Proc. OFC/NFOEC, paper OW1E.1, 2013.

[8] S. Yamanaka, H. Uzawa, T. Ohara, T. Saida, T. Akashi, K. Mori, O. Takeuchi, H. Onaka, K. Takei, K. Terada, S. Aisawa, and O. Ishida, "100 Gb/s CFP coherent transceiver enabled by power-optimized DSP," OECC/ACOFT, 2014. http://www.oecc-acoft2014.org/wp-content/uploads/THPDP1-4oecc2014Abstract00724.pdf

[9] R. Giddings, "Real-time Digital Signal Processing for Optical OFDM-Based Future Optical Access Networks," J. of Lightwave Tech., vol. 32, no. 4, pp. 553-570, 2014.

[10] NTT Electronics and Acacia Communications Announce Interoperability Mode of Operation in Next-Generation Coherent ASICs, 2013, http://www.ntt-electronics.com/en/news/2013/09/100gdsplsi.html

[11] D. C. Kilper, G. Atkinson, S. K. Korotky, S. Goyal, P. Vetter, D. Suvakovic, and O. Blume, "Power Trends in Communication Networks," IEEE J. of Selected Topics in Quantum Electronics, vol. 17, no. 2, pp. 275-284, 2011.

[12] T. J. Xia, G. Wellbrock, B. Basch, S. Kotrla, W. Lee, T. Tajima, K. Fukuchi, M. Cvijetic, J. Sugg, Y. Ma, B. Turner, C. Cole, and C. Urricariet, "End-to-end Native IP Data 100G Single Carrier Real Time DSP Coherent Detection Transport over 1520-km Field Deployed Fiber," Proc. OFC/NFOEC, paper PDPD4, 2010.

[13] J. Faure, B. Lavigne, C. Bresson, O. Bertran-Pardo, A. C. Colomer, and R. Cantó, "40G and 100G deployment on 10G Infrastructure: market overview and trends, Coherent versus Conventional technology," Proc. OFC/NFOEC, paper OThE3, 2010.

[14] T. Toifl, C. Menolfi, M. Ruegg, R. Reutemann, P. Buchmann, M. Kossel, T. Morf, J. Weiss, and M. L. Schmatz, "A 22-Gb/s PAM-4 Receiver in 90-nm CMOS SOI Technology," IEEE J. of Solid-State Circuits, vol. 41, no. 4, pp. 954-965, 2006.

[15] K. Szczerba, P. Westbergh, J. Karout, J. S. Gustavsson, Å. Haglund, M. Karlsson, P. A. Andrekson, E. Agrell, and A. Larsson, "4-PAM for High-Speed Short-Range Optical Communications," J. Opt. Commun. Netw., vol. 4, no. 11, pp. 885-894, 2012.

[16] J. Wei, Q. Cheng, R. V. Penty, I. White, and D. Cunningham, "Analysis of Complexity and Power Consumption in DSP-based Optical Modulation Formats," in Advanced Photonics for Communications, OSA Technical Digest (online) (Optical Society of America, 2014), paper SM2D.5.

[17] J. L. Wei, J. D. Ingham, D. G. Cunningham, R. V. Penty, and I. H. White, "Performance and Power Dissipation Comparisons Between 28 Gb/s NRZ, PAM, CAP and Optical OFDM Systems for Data Communication Applications," J. of Lightwave Tech., vol. 30, no. 20, pp. 3273-3280, 2012.

[18] K. Zhong, X. Zhou, T. Gui, L. Tao, Y. Gao, W. Chen, J. Man, L. Zeng, A. P. T. Lau, and C. Lu, "Experimental study of PAM-4, CAP-16, and DMT for 100 Gb/s Short Reach Optical Transmission Systems," Optics Express, vol. 23, no. 2, pp. 1176-1189, 2015.

[19] R. van Nee, G. Awater, M. Morikura, H. Takanashi, M. Webster, and K. W. Halford, "New high-rate wireless LAN standards," IEEE Communications Magazine, vol. 37, issue 12, pp. 82-88, 1999.

[20] P. Reusens, D. Van Bruyssel, J. Sevenhans, S. Van Den Bergh, B. Van Nimmen, and P. Spruyt, "A practical ADSL technology following a decade of effort," IEEE Communications Magazine, vol. 39, issue 10, pp. 145-151, 2001.

[21] I. B. Djordjevic, and B. Vasic, "Orthogonal frequency division multiplexing for high-speed optical transmission," Optics Express, vol. 14, no. 9, pp. 3767-3775, 2006.

[22] J. Armstrong, "OFDM for Optical Communications," J. of Lightwave Tech., vol. 27, no. 3, pp. 189-204, 2009.

[23] F. Buchali, X. Xiao, S. Chen, and M. Bernhard, "Towards real-time CO-OFDM transceivers," Proc. OFC/NFOEC, paper OWE1, 2011.

[24] R. P. Giddings, E. Hugues-Salas, and J. M. Tang, "Experimental demonstration of record high 19.125Gb/s real-time end-to-end dual-band optical OFDM transmission over 25km SMF in a simple EML-based IMDD system," Optics Express, vol. 20, no. 18, pp. 20666-20679, 2012.

[25] M. Chen, J. He, J. Tang, X. Wu, and L. Chen, "Experimental demonstration of real-time adaptively modulated DDO-OFDM systems with a high spectral efficiency up to 5.76bit/s/Hz transmission over SMF links," Optics Express, vol. 22, no. 15, pp. 17691-17699, 2014.

[26] M. Cvijetic and I. Djordjevic, *Advanced Optical Communication, Systems and Networks*, Artech House, 2013.

[27] S.B. Weinstein, and P.M. Ebert, "Data Transmission by Frequency-Division Multiplexing Using the Discrete Fourier Transform," IEEE Trans. Commun. Technol., vol. COM-19, no. 5, pp. 628-634, 1971.

[28] S. Gringeri, B. Basch, V. Shukla, R. Egorov, and T. J. Xia, "Flexible Architectures for Optical Transport Nodes and Networks," IEEE Commun. Mag., vol. 48, no. 7, pp. 40-50, 2010.

[29] N. Cvijetic, A. Tanaka, M. Cvijetic, Y. Huang, E. Ip, Y. Shao, and T. Wang, "Novel Optical Access and Digital Processing Architectures for Future Mobile Backhaul," Journal of Lightwave Technology, vol. 31, issue 4, pp. 621-627, 2013.

[30] N. Cvijetic, A. Tanaka, P. N. Ji, S. Murakami, K. Sethuraman, and T. Wang, "First OpenFlow-based Software-Defined λ-Flow Architecture for Flex-Grid OFDMA Mobile Backhaul over Passive Optical Networks with Filterless Direct Detection ONUs," OFC/NFOEC Technical Digest, paper PDP5B.2, 2013.

[31] W. Mo, J. He, M. M. Karbassian, J. Wissinger, and N. Peyghambarian, "Situation-Aware Multipath Routing and wavelength Re-assignment in a Unified Packet-circuit OpenFlow Network," OFC/NFOEC Technical Digest, paper NTu3F.6, 2013.

[32] Xilinx Virtex-5 FPGA Data Sheet: DC and Switching Characteristics: http://www.xilinx.com/support/documentation/data_sheets/ds202.pdf

[33] Xilinx LogiCORE IP Fast Fourier Transform v7.1: http://japan.xilinx.com/support/documentation/ip_documentation/xfft_ds260.pdf

[34] VLC media player: http://www.videolan.org/vlc/
[35] Xilinx Virtex-5 FPGA Embedded Tri-Mode Ethernet MAC User Guide: http://www.xilinx.com/support/documentation/user_guides/ug194.pdf
[36] B. Lin, J. Li, H. Yang, Y. Wan, Y. He, and Z. Chen, "Comparison of DSB and SSB Transmission for OFDM-PON [Invited]," J. Opt. Commun. Netw., vol. 4, no. 11, pp. B94-B100, 2012.
[37] Z. Pan, C. Yu, and A. E. Willner, "Optical performance monitoring for the next generation optical communication networks," Optical Fiber Technology, vol. 16, pp. 20–45, 2010.
[38] Synopsys Insight Newsletter - Multi-Gigahertz FPGA Signal Processing: https://www.synopsys.com/COMPANY/PUBLICATIONS/SYNOPSYSINSIGHT/Pages/Art1-fpga-signal-processing-IssQ1-13.aspx
[39] Y. Zhang, P. Chowdhury, M. Tornatore, and B. Mukherjee, "Energy Efficiency in Telecom Optical Networks," IEEE Communications Surveys & Tutorials, vol. 12, no. 4, pp. 441-458, 2010.
[40] Ciena F10-T Transponder module datasheet: http://media.ciena.com/documents/F10-T_Transponder_Module_DS.pdf
[41] Infinera HEX 10G OTN Transponder datasheet: https://www.infinera.com/wp-content/uploads/2015/09/DS_TM_TPHEX10GOTN_B1.pdf
[42] Finisar FTLX1672D3BNL Multi-rate transceiver - Product specification: https://www.finisar.com/sites/default/files/downloads/finisar_ftlx1672d3bnl_10g_er_40km_sfp_optical_transceiver_product_specrevc1.pdf
[43] S. Adhikari, S. L. Jansen, M. Alfiad, B. Inan, V. A. J. M. Sleiffer, A. Lobato, P. Leoni, and W. Rosenkranz, "Self-coherent optical OFDM, an interesting alternative to direct or coherent detection," in Proc. ICTON, paper We.C1.3, 2011.
[44] D. Che, X. Chen, J. He, A. Li, and W. Shieh, "102.4-Gb/s Single-Polarization Direct-Detection Reception using signal carrier interleaved optical OFDM," in Proc. OFC, paper Tu3G.7, 2014.
[45] M. Sjödin, E. Agrell, P. Johannisson, G. Lu, P. A. Andrekson, and M. Karlsson, "Filter optimization for self-homodyne coherent WDM systems using interleaved polarization division multiplexing," J. Lightwave Tech., vol. 29, pp. 1219-1226, 2011.
[46] B. J. C. Schmidt, Z. Zan, L. B. Du, and A. J. Lowery, "100 Gbit/s transmission using single-band direct-detection optical OFDM," in Proc. OFC/NFOEC, paper PDPC3, 2009.
[47] D. Qian, N. Cvijetic, J. Hu, and T. Wang, "108 Gb/s OFDMA-PON with Polarization Multiplexing and Direct Detection," J. Lightwave Tech., vol. 28, pp. 484–493, 2010.
[48] H. Huang, C. Sun, C. Lin, C. Wei, W. Zeng, H. Chang, B. Shih, and A. Ng'oma, "Direct-Detection PDM-OFDM RoF System for 60-GHz Wireless MIMO transmission without Polarization Tracking," in Proc. OFC, paper W3F.2, 2015.
[49] A. Amin, H. Takahashi, I. Morita, and H. Tanaka, "100-Gb/s Direct-Detection OFDM Transmission on Independent Polarization Tributaries," IEEE Phot. Tech. Lett., vol. 22, pp. 468–470, 2010.
[50] D. Qian, T. Kwok, N. Cvijetic, J. Hu, and T. Wang, "41.25 Gb/s realtime OFDM receiver for variable rate WDM-OFDMA-PON transmission," in Proc. OFC, paper PDPD9, 2010.
[51] N. Yoshimoto, J. Kani, S. Kim, N. Iiyama, and J. Terada, "DSP-Based Optical Access Approaches for Enhancing NG-PON2 Systems," IEEE Commun. Mag., vol. 51, issue 3, pp. 58-64, 2013.
[52] B. Koch, R. Noé, D. Sandel, and V. Mirvoda, "Versatile endless optical polarization controller/tracker/demultiplexer," Optics Express, vol. 22, no. 7, pp. 8259-8276, 2014.
[53] W. Freude, R. Schmogrow, B. Nebendahl, M. Winter, A. Josten, D. Hillerkuss, S. Koenig, J. Meyer, M. Dreschmann, M. Huebner, C. Koos, J. Becker, and J. Leuthold, "Quality Metrics for Optical Signals: Eye Diagram, Q-factor, OSNR, EVM and BER," Proc. ICTON, paper Mo.B1.5, 2012.
[54] W. Kester, "Taking the Mystery out of the Infamous Formula, 'SNR = 6.02N + 1.76dB,' and Why You Should Care," Analog Devices, MT-001 tutorial, http://www.analog.com/media/en/training-seminars/tutorials/MT-001.pdf
[55] J. D. Proakis, and M. Salehi, *Digital Communications*, McGraw-Hill, 2008.

[56] F. Paolucci, F. Fresi, A. Castro, L. Velasco, F. Cugini, N. Sambo, A. Giorgetti, L. Potì, and P. Castoldi, "Filter Optimization in SDN-based Flexgrid Networks," Optical Fiber Communication Conference, paper Th3I.4, 2014.

[57] O. Gerstel, M. Jinno, A. Lord, and S. J. B. Yoo, "Elastic optical networking: a new dawn for the optical layer?," IEEE Communications Magazine, vol. 50, issue 2, pp. s12-s20, 2012.

[58] B. Heller, R. Sherwood, and N. McKeown, "The Controller Placement Problem," ACM SIGCOMM Computer Communication Review, 2012.

[59] F. Agraz, S. Azodolmolky, M. Angelou, J. Perelló, L. Velasco, S. Spadaro, A. Francescon, C.V. Saradhi, Y. Pointurier, P. Kokkinos, E. Varvarigos, M. Gunkel, and I. Tomkos, "Experimental Demonstration of Centralized and Distributed Impairment-Aware Control Plane Schemes for Dynamic Transparent Optical Networks," Optical Fiber Communication Conference, paper PDPD5, 2010.

[60] H. Ji, K. Park, J. Lee, H. Chung, E. Son, K. Han, S. Jun, and Y. Chung, "Optical performance monitoring techniques based on pilot tones for WDM network applications," J. of Optical Networking, vol. 3, no. 7, pp. 510-533, 2004.

[61] C. Ito, and J. C. Cartledge, "Polarization independent all-optical 3R regeneration based on the Kerr effect in highly nonlinear fiber and offset spectral slicing," IEEE J. Sel. Top. in Quant. Elec., vol. 14, no. 3, pp. 616-624, 2008.

[62] F. Parmigiani, L. Oxenløwe, M. Galili, M. Ibsen, D. Zibar, P. Petropoulos, D. J. Richardson, A. T. Clausen, and P. Jeppesen, "All-optical 160-Gbit/s retiming system using fiber grating based pulse shaping technology," J. Lightw. Technol., vol. 27, no. 9, pp. 1135-1141, 2009.

[63] H. Murai, M. Kagawa, H. Tsuji, and K. Fujii, "80-Gb/s error-free transmission over 5600 km using a cross absorption modulation based optical 3R regenerator," IEEE Photon. Technol. Lett., vol. 17, no. 9, pp. 1965-1967, 2005.

[64] T. Otani, T. Miyazaki, and S. Yamamoto, "40-Gb/s optical 3R regenerator using electroabsorption modulators for optical networks," J. Lightw. Technol., vol. 20, no. 2, pp. 195-200, 2002.

[65] C. Bornholdt, J. Slovak, and B. Sartorius, "Semiconductor-based all-optical 3R regenerator demonstrated at 40 Gbit/s," Electron. Lett., vol. 40, no. 3, 2004.

[66] J. Leuthold, B. Mikkelsen, R. E. Behringer, G. Raybon, C. H. Joyner, and P. A. Besse, "Novel 3R regenerator based on semiconductor optical amplifier delayed-interference configuration," IEEE Photon. Technol. Lett., vol. 13, no. 8, pp. 860-862, 2001.

[67] S. Liu, K. J. Lee, F. Parmigiani, K. Gallo, P. Petropoulos, and D. J. Richardson, "Retiming of short pulses using quadratic cascading in a periodically poled lithium niobate waveguide," IEEE Photon. Technol. Lett., vol. 23, no. 2, pp. 94-96, 2011.

[68] J. A. Harrison, K. J. Blow, and A. J. Poustie, "All-optical bit-level retiming and jitter suppression," Opt. Comm., vol. 240, pp. 221–226, 2004.

[69] F. M. Mitschke, and L. F. Mollenauer, "Experimental observation of interaction forces between solitons in optical fibers," Opt. Lett., vol. 12, no. 5, pp. 355-357, 1987.

[70] B. A. Malomed, "Bound solitons in the nonlinear Schrodinger —Ginzburg-Landau equation," Phys. Rev. A, vol. 44, no. 10, pp. 6954-6957, 1991.

[71] M. Stratmann, and F. Mitschke, "Bound states between dark and bright solitons in dispersion maps," in Quantum Electronics and Laser Science Conference, QELS '02, Technical Digest, pp. 226-227, 2002.

[72] M. Stratmann, T. Pagel, and F. Mitschke, "Experimental observation of temporal soliton molecules," Phys. Rev. Lett., vol. 95, 143902, 2005.

[73] I. Gabitov, R. Indik, L. Mollenauer, M. Shkarayev, M. Stepanov, and P. M. Lushnikov, "Twin families of bisolitons in dispersion-managed systems," Opt. Lett., vol. 32, no. 6, pp. 605-607, 2007.

[74] A. Hause, H. Hartwig, B. Seifert, H. Stolz, M. Böhm, and F. Mitschke, "Phase structure of soliton molecules," Phys. Rev. A, vol. 75, 063836, 2007.

[75] M. Shkarayev, M.G. Stepanov, "New bisoliton solutions in dispersion managed systems," Physica D, vol. 238, pp. 840-845, 2009.

[76] S. Pau, J. Yu, N. Chand, K. Kojima, "160Gb/s all optical time-slot switching for OTDM applications," Phot. Tech. Lett., vol. 14, 1460, 2002.
[77] F. Mitschke, Compounds of Fiber-Optic Solitons. Lect. Notes Phys. vol. 751, pp. 175–194, Springer-Verlag, Berlin Heidelberg, 2008.
[78] A. Hause, H. Hartwig, M. Böhm, and F. Mitschke, "Binding mechanism of temporal soliton molecules," Phys. Rev. A, vol. 78, 063817, 2008.
[79] V. V. Afanasjev, B. A. Malomed, and P. L. Chu, "Stability of bound states of pulses in the Ginzburg-Landau equations," Phys. Rev. E, vol. 56, no. 5, pp. 6020-6025, 1997.
[80] U. Al Khawaja, "Stability and dynamics of two-soliton molecules," Phys. Rev. E, vol. 81, 056603, 2010.
[81] M. Romagnoli, S. Wabnitz, P. Franco, M. Midrio, F. Fontana, and G. Bordogna, "Multisoliton interaction in actively mode-locked erbium fiber lasers: theory and experiment," Opt. Comm., vol. 108, pp. 65-70, 1994.
[82] D. Y. Tang, L. M. Zhao, and B. Zhao, "Multipulse bound solitons with fixed pulse separations formed by direct soliton interaction," Appl. Phys. B, vol. 80, pp. 239–242, 2005.
[83] A. Maruta, T. Inoue, Y. Nonaka, and Y. Yoshika, "Bisoliton propagating in dispersion-managed system and its application to high-speed and long-haul optical transmission," IEEE J. Sel. Top. in Quant. Elec., vol. 8, no. 3, pp. 640- 650, 2002.
[84] T. Widdowson, D.J. Malyon, A.D. Ellis, K. Smith and K.J. Blow, "Soliton shepherding: All-optical active soliton control over global distances," Electron. Lett., vol. 30, no. 12, pp. 990-991, 1994.
[85] G. P. Agrawal, *Nonlinear Fiber Optics*, 3rd ed., Academic Press, New York, 2001.
[86] A. Pinto, G. P. Agrawal, and J. F. da Rocha, "Effect of soliton interaction on timing jitter in communication systems," J. Lightwave Technol., vol. 16, no. 4, pp. 515-519, 1998.
[87] T. von Lerber, S. Honkanen, A. Tervonen, H. Ludvigsen, and F. Küppers, "Optical clock recovery methods: Review (Invited)," Opt. Fiber Technol., vol. 15, pp. 363–372, 2009.
[88] S. Johnson, W. Mo, M. Cvijetic, J. He, J. Wissinger and A. E. Willner, "Real-Time Software-Defined Dynamic Resource Allocation using OpenFlow for Next-Generation OFDM-based Optical Access Networks," Optical Fiber Communication Conference, paper Tu2F.5, 2014.
[89] S. Johnson and M. Cvijetic, "Unified Direct and Coherent Detection Real-Time OFDM Scheme for Optical Access Networks," Optical Fiber Communication Conference, paper W2A.62, 2016.
[90] S. Johnson and M. Cvijetic, "Unified direct and coherent orthogonal frequency division multiplexing optical transmission scheme," Applied Optics, vol. 54, no. 36, pp. 10606-10612, 2015.
[91] W. Mo, S. Johnson, M. Yang, M. Cvijetic, A. Ahsan, W. Gao, D. Kilper, K. Bergman, J. Wissinger, and J. Zhu, "OFDM Pilot-tone Assisted Distributed Control for SDN-based Elastic Optical Networks," IEEE Optical Interconnects Conference, TuP18, 2015.
[92] S. Johnson, S. Pau, and F. Küppers, "All-Optical Re-Timing Using the 'Soliton Molecule Effect'," Numerical Analysis and Applied Mathematics ICNAAM 2011, AIP Conf. Proc. 1389, pp. 701-704, 2011.
[93] S. Johnson, S. Pau, and F. Küppers, "Experimental Demonstration of Optical Retiming Using Temporal Soliton Molecules," IEEE J. of Lightwave Tech., vol. 29, no. 23, pp. 3493-3499, 2011.
[94] Y. Mostofi, D. C. Cox, and A. Bahai, "Effect of Frame Synchronization Errors on Pilot-aided Channel Estimation in OFDM: Analysis and Solution," 5th International Symposium on Wireless Personal Multimedia Communications, vol. 3, pp. 1309–1313, 2002.
[95] T. M. Schmidl, and D. C. Cox, "Robust Frequency and Timing Synchronization for OFDM," IEEE Trans. on Communications, vol. 45, no. 12, pp. 1613-1621, 1997.
[96] S. Tsakiris, A. Salis, and N. Uzunoglu, "FPGA Implementation of a Frame Synchronization Algorithm for Powerline Communications," Radioengineering, vol. 18, no. 3, pp. 325-329, 2009.
[97] N. Kaneda, T. Pfau, and Q. Yang, "Frame/symbol synchronization in coherent optical OFDM," United States Patent Application Publication, Pub. no.: US 2012/0027419 A1, 2012.

[98] B. Jahan, M. Lanoiselée, G. Degoulet, and R. Rabineau, "Frame synchronization method for OFDM/QAM and ODFM/OQAM modulations," 4th IEEE International Conference on Circuits and Systems for Communications, pp. 445-449, 2008.

[99] R. Bouziane, Y. Benlachtar, and R. I. Killey, "Frequency-Based Frame Synchronization for High-Speed Optical OFDM," IEEE International Conference on Photonics in Switching, pp. 1–3, 2012.

[100] J. van de Beek, M. Sandell, M. Isaksson, and P. O. Borjesson, "Low-Complex Frame Synchronization in OFDM Systems," 4th IEEE International Conference on Universal Personal Communications, pp. 982–986, 1995.

[101] Y. Kim, and F. Langinieux, "Frame synchronization method and apparatus for use in digital communication system utilizing OFDM method," United States Patent, Patent no.: US 6,172,993 B1, 2001.

[102] R. Bouziane, and R. I. Killey, "Blind symbol synchronization for direct detection optical OFDM using a reduced number of virtual subcarriers," Optics Express, vol. 23, no. 5, pp. 6444-6454, 2015.